SLAC-177
UC-34d
(T/E)

A STUDY OF THE REACTIONS $\bar{K}^0 p \to \Lambda\pi^+$ AND $\bar{K}^0 p \to \Sigma^0\pi^+$ FROM 1 GeV/c to 12 GeV/c *

ROBERT J. YAMARTINO, JR.

STANFORD LINEAR ACCELERATOR CENTER

STANFORD UNIVERSITY

Stanford, California 94305

September 1974

PREPARED FOR THE U.S. ATOMIC ENERGY

COMMISSION UNDER CONTRACT NO. AT(04-3)-515

Printed in the United States of America. Available from National Technical Information Service, U.S. Department of Commerce, 5285 Port Royal Road, Springfield, Virginia 22151. Price: Printed Copy $5.45; Microfiche $1.45.

---

*Ph. D. dissertation, May 1974.

ABSTRACT

Experimental results are reported on the $\Lambda\pi^+$ and $\Sigma^0\pi^+$ final states in $\overline{K}^0p$ interactions for lab momenta between 1 GeV/c and 12 GeV/c. The data were obtained from an exposure of the SLAC 40-inch hydrogen bubble chamber to a K_L^0 beam. Cross sections, differential cross sections, and hyperon polarization are presented for both final states. Momentum dependences of the total cross sections are obtained and indicate possible convergence to cross sections obtained in the accompanying, pion induced, line reversed reactions as predicted by the hypothesis of exchange degenerate K*(890) and K*(1420) trajectories. Similarly, the Σ^0/Λ cross section ratio for $0.05 \leq -t \leq 0.4$ GeV^2 is seen to be nearly momentum independent as expected from exchange degeneracy. Fitted slopes for the forward differential cross sections are observed at higher momenta to increase toward slope values extracted from the line reversed companion reactions, suggesting that the equal slope prediction of exchange degeneracy is realized near incident momenta of 10 GeV/c. Extrapolated forward cross sections are used to calculate the helicity non-flip coupling constant F_+. The observed momentum dependence of F_+ suggests that final state interactions are important near $t \sim 0$. Polarization of the Λ is observed to be large, positive, and relatively momentum independent above 2 GeV/c and this is viewed as possible evidence for "weak" exchange degeneracy of the K*, K** trajectories.

Discussion centers around the importance of understanding the final state interactions which mask exchange degenerate behavior and the significance of phase space and angular momentum barrier correction factors at these energies.

PREFACE

I would like to express my thanks at this time to the many people who helped make this work possible.

I am grateful for the assistance given us by Bob Watt and the crew of the SLAC 40-inch bubble chamber and by John Brown and the scanning and measuring staff at SLAC. I also thank Dwight Johnson for much of the preliminary data reduction work.

I have enjoyed very much working with the other physicists in Group B. In particular, I want to thank Bill Johnson, Jim Loos, George Luste, Kai Moriyasu, and Ben Shen for their patience in answering the frequent and all too often stupid questions of a beginning graduate student. I have learned much from each of them.

George Brandenburg and John Matthews deserve many thanks for their numerous suggestions on improving the analysis of these data and for thoughtful readings of the manuscript. I also wish to thank Roger Cashmore, Fred Gilman, and Ernie Moniz for interesting and helpful discussions.

My special thanks to David Leith, my research advisor, for his guidance, enthusiasm, and encouragement throughout my graduate career.

Considerable effort has gone into the preparation of this manuscript. I thank Betty Pennington for typing the many rough drafts.

Finally, I would like to thank my close friends for making my graduate years very enjoyable and my parents for their unfailing support, wisdom, and understanding.

TABLE OF CONTENTS

LIST OF TABLES

LIST OF FIGURES

Page

Page

CHAPTER 1

Introduction

In the early days of this experiment the concept of duality was not yet proposed. The notion of exchange degeneracy as suggested by Arnold[1] was just two years old and, though well supported for $t > 0$ by the distribution of meson resonances on the Chew-Frautschi plot (Fig. 1), was relatively untested in the $t < 0$ region. However, with the advent of duality and duality diagrams, the issue of whether trajectories remained degenerate in the scattering region assumed new significance.

The idea of duality[2] followed soon after the derivation of finite energy sum rules[2,3] which in turn are based on the assumption that above some reasonable laboratory energy $\nu > N$, the scattering amplitude $f(\nu, t)$ can be expressed as a sum of t channel Regge exchange amplitudes, i.e.

$$f(\nu, t) = -\sum_i \beta_i(t) \frac{1 \pm e^{-i\pi\alpha_i(t)}}{\sin \pi\alpha_i(t)} \nu^{\alpha_i(t)} \tag{1.1}$$

where t is the invariant four momentum transfer, $\alpha_i(t)$ the Regge trajectory, and $\beta_i(t)$ the Regge residue function. Assumption of analyticity and crossing properties of the amplitude then leads to an infinite set of sum rules,[2,3] the most important of which is

$$\int_0^N \operatorname{Im} f(\nu, t)\, d\nu = \sum_i \pm \beta_i(t) \frac{N^{\alpha_i(t)+1}}{\alpha_i(t)+1} \tag{1.2}$$

With the added assumption of resonance dominance of $\operatorname{Im} f(\nu, t)$ the notion of global duality is realized in that $\operatorname{Im} f(\nu, t)$ can be completely described as either a sum over s-channel resonances or a sum over t-channel Regge

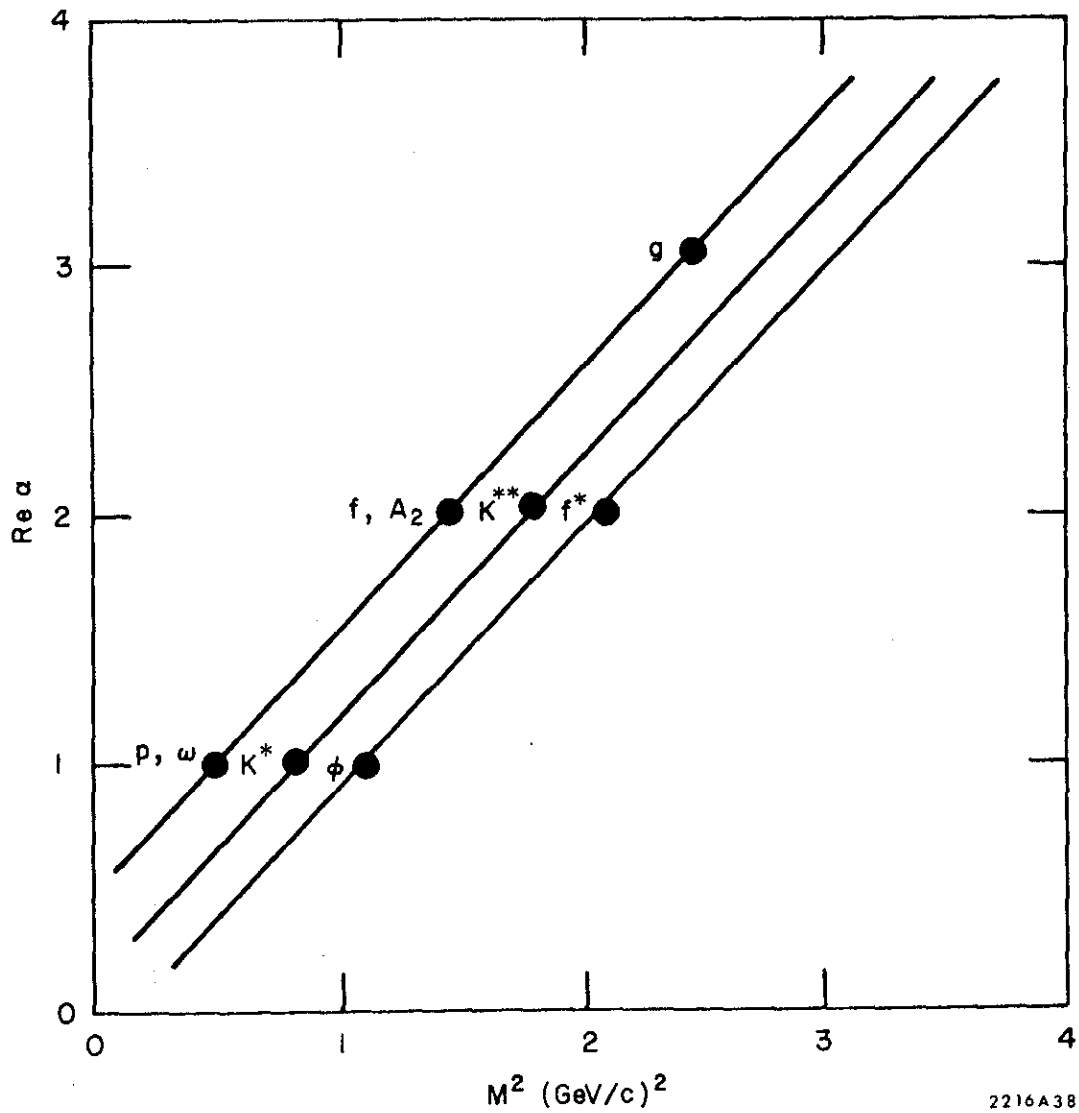

FIG. 1--Chew-Frautschi plot of some well known meson resonances. That these resonances lie along straight lines of slope ~ 1 GeV^2 is suggestive of exchange degeneracy.

exchanges. Choice of the desired basis set then becomes, in principle, a matter of convenience.

Consider now the situation where the quantum numbers in the s-channel are exotic. The presence of s-channel resonances is therefore suppressed and the left hand side of the sum rule equals zero. This then constrains the right hand side of the sum rule to vanish and hence demands that the Regge exchange amplitudes must cancel. Such a cancellation can occur at all ν and t only if the $\alpha_i(t)$ are identical and $\sum_i \pm \beta_i(t) = 0$, where the sign chosen is the one relevant to the signature factor for the ith exchange. Hence, duality provides a way of predicting exchange degeneracy.

The duality diagrams of Harari[4] and Rosner[5] extend the definition of "exotic" to include reactions with non-planar quark diagrams so that processes like $\overline{K}^0 p \rightarrow \Lambda \pi^+$ (Fig. 2) are considered exotic even though the quantum numbers allow resonances in all three channels. Hence, according to Harari's conjecture,both the helicity flip and non-flip amplitudes for this process should be real at high energies, resulting in zero polarization of the Λ. The data of this and other experiments show strong Λ polarization in apparent contradiction with the theory.

The validity of exchange degeneracy can be tested outside the framework of duality if one considers line reversed processes. As a test of K*(890) - K*(1420) degeneracy we consider the line reversed reaction pairs

$$\overline{K}^0 p \rightarrow \Lambda \pi^+ \quad (1a)$$

$$\pi^- p \rightarrow \Lambda K^0 \quad (1b)$$

and

$$\overline{K}^0 p \rightarrow \Sigma^0 \pi^+ \quad (2a)$$

$$\pi^- p \rightarrow \Sigma^0 K^0 \quad (2b)$$

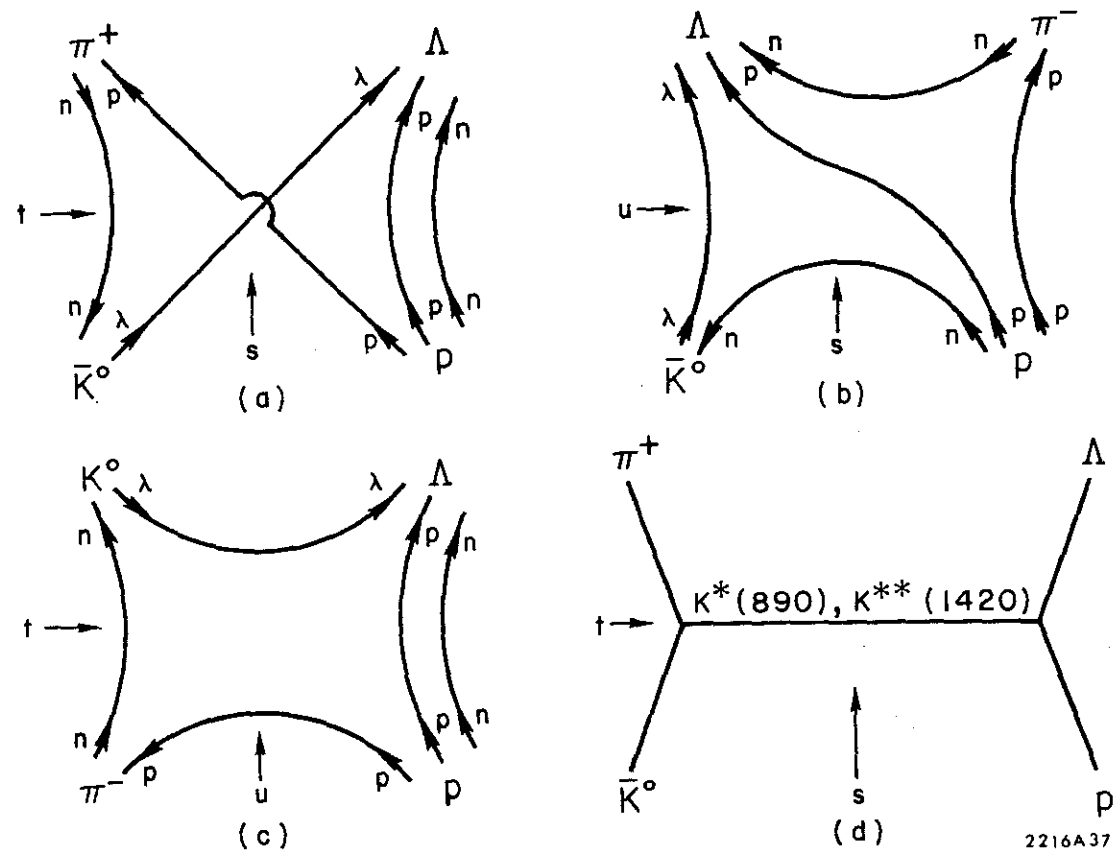

FIG. 2--Duality diagram for the process $\overline{K}^{o}p \rightarrow \pi^{+}\Lambda$. Intersecting quark lines indicate an exotic, non-planar diagram.

where the first reaction of each pair $a + b \to c + d$ has amplitudes A and the second reaction, the line reversed counterpart, is denoted $\bar{c} + b \to \bar{a} + d$ and has amplitudes $\bar{A}$. These two reactions are related by s-u crossing, where $s = (a+b)^2 = (c+d)^2$, $t = (a-c)^2 = (b-d)^2$ and $u = (b-c)^2 = (a-d)^2$ are the Mandelstam invariant variables and where $\nu = (s - u)/4m_b$ and t are chosen as the two independent variables. The amplitudes A and $\bar{A}$ can be written in terms of amplitudes $A^{(+)}$ and $A^{(-)}$ which are even or odd under the crossing of $\nu \to -\nu$ as follows:

$$A = A^{(+)} + A^{(-)}$$

$$\bar{A} = A^{(+)} - A^{(-)}$$

Generally, $|A|^2 \neq |\bar{A}|^2$ so that cross sections for $ab \to cd$ are not equal to those for $\bar{c}b \to \bar{a}d$. However, Gilman[6] has pointed out that the amplitudes $A^{(+)}$ and $A^{(-)}$ correspond to the tensor and vector amplitudes respectively, and that the phases of these amplitudes are just given by their Regge signature factors so that the phases of $A^{(+)}$ and $A^{(-)}$ are

$$1 + e^{-i\pi\alpha_T(t)} = 2e^{\frac{1}{2}i\pi\alpha_V(t)} \cos \tfrac{1}{2}\pi\alpha_T(t)$$

$$1 - e^{-i\pi\alpha_V(t)} = 2ie^{\frac{1}{2}i\pi\alpha_V(t)} \sin \tfrac{1}{2}\pi\alpha_V(t)$$

respectively. If the trajectories are "weakly" exchange degenerate, i.e. $\alpha_T(t) = \alpha_V(t)$, then the two amplitudes $A^{(+)}$ and $A^{(-)}$ are seen to be always 90° out of phase and hence add incoherently so that

$$\frac{d\sigma}{dt}(a + b \to c + d) = \frac{d\sigma}{dt}(\bar{c} + b \to \bar{a} + d)$$

$$P(a + b \to c + d) = -P(\bar{c} + b \to \bar{a} + d).$$

In the case of "strong" exchange degeneracy, i.e., $\beta_T(t) = \beta_V(t)$ and $\alpha_T(t) = \alpha_V(t)$, the polarization vanishes and, in addition, the amplitude A becomes purely real, in agreement with the duality prediction while the amplitude $\overline{A}$ has the rotating phase $e^{-i\pi\alpha(t)}$.

While the idea of exchange degeneracy is quite successful in understanding some reactions, it seems to fail rather badly for reactions (1) and (2).[7-9]

All available data indicate that:

(i) cross sections for the $\overline{K}$ induced reactions are as much as a factor of 2 larger than π induced cross sections,

(ii) differential cross section slopes, b_π, for π induced reactions are systematically larger than the slopes, $b_{\overline{K}}$, for the $\overline{K}$ induced reactions, and

(iii) the polarizations observed in these processes are neither zero nor mirror images of one another.

Conventional absorption models[10] with purely imaginary absorption have proven incapable of providing a qualitative description of the data for two basic reasons. First, evaluation of the absorption for real versus rotating phases leads to the erroneous prediction that the π induced cross sections should be larger than the $\overline{K}$ induced cross sections. Secondly, though correct polarizations can be predicted for the π induced reactions, zero polarization results for the $\overline{K}$ induced reactions.

Modified absorption models such as the Dual Absorptive Model of Harari[11] and the Ringland-Roberts-Roy-Tran Thanh Van Reggeized Absorption Model[12] are capable of producing respectable fits[13, 14] to the data but primarily because of built in freedom to parameterize the real part of the helicity non-flip amplitude in the case of the DAM model and insertion of a phase factor into the absorption correction for the latter model. Recently the Hartley-Kane model,[15]

which strives to model in detail the "absorption" terms, has achieved at least qualitative agreement with essentially all two body reactions.

Another model, rather successful in accommodating the data and put forth by R.D. Field,[16] suggests the importance of lower lying EXD daughter trajectories as well as Pomeron-Regge pole cuts. This model has the desirable feature of explicitly preserving duality and exchange degeneracy exactly for the bare poles by isolating the EXD and duality breaking to the Pomeron-Regge pole cut terms. Higher energy data should provide a severe test for this model.

Before moving on to a description of the experiment, I would like to mention briefly some of the other motivations and successes of this experiment which unfortunately lie outside the scope of this paper.

The $K_L^o p$ bubble chamber experiment was intended to provide moderate statistics on a wide variety of final states over a wide range of incident momenta and momentum transfers. One of the prime motivations for this experiment was its unique ability to permit direct comparison of $K^o(S = +1)$ and $\overline{K}^o(S = -1)$ processes with no relative normalization error. This property of the K_L^o beam proved to be a significant advantage in a recent analysis of $K^o p \rightarrow Q^o p$ and $\overline{K}^o p \rightarrow \overline{Q}^o p$ reactions observed in the final state $K_S^o \pi^+ \pi^- p$,[17] as it facilitated comparison of the total cross sections and permitted bias free observation of a crossover[18] at $-t' = 0.13 \pm 0.03$ GeV^2 in the differential cross sections. It is expected to be of equal advantage in the forthcoming analysis of the final states $K^{\pm} \pi^{\mp} p$.

Observation of the reaction $K_L^o p \rightarrow K_S^o p$ led not only to the determination of the $K_L^o \rightarrow K_S^o$ regeneration phase angle $\varphi_f = -43.9^o \pm 4.0^o$ and the intercept of the effective trajectory, $\alpha(0) = 0.49 \pm 0.05$,[19] presumably dominated by ω exchange, but also to a prediction of the f/d ratio for the non-flip coupling of

vector mesons to baryons.[20] Analysis of the backscattered events from this same reaction has provided direct experimental evidence that $g^2_{N\Sigma K} << g^2_{N\Lambda K}$.[21]

In addition, measurement of the large number of two prongs, necessary for flux and yield determination, has given rise to a new measurement of the $K^o_{\mu 3}/K^o_{e3}$ branching ratio, in agreement with the older measurements that suggested that the $\Delta I = 1/2$ rule is not exactly satisfied. Also measured was the linear slope of the f_+ form factor, with the result found to be in good agreement with previous measurements.[22]

Further analysis in the final states $K^o_S \pi^+ \pi^- p$, $\Lambda \pi^+ \pi^- \pi^+$, and $\Lambda \pi^+ K^- K^+$ is planned and indications are that the time-of-flight system will permit 1-C analysis of the final state $np\pi^- \pi^+$ to provide new insight into the quasi-two-body process $np \rightarrow \Delta^- \Delta^{++}$.

CHAPTER 2

Experimental Apparatus and Data Reduction

A. General Description

The main design criteria of this experiment was the creation of a K_L^o beam relatively free of contamination from charged particles as well as other neutral particles. The use of such a neutral beam offers a few advantages over charged K beams apart from the previously mentioned equal mixture of $S = \pm 1$ components. One advantage is the ability to use a more intense beam. Since a neutral K beam leaves no tracks in the bubble chamber, fluxes as large as 40 K_L^o's per picture could be tolerated without creating scanning difficulties or reducing the effectiveness of automatic measuring machines such as the spiral reader at SLAC. Another advantage from the point of view of the reactions $\overline{K}N \rightarrow Y^o\pi$ is that $\overline{K}^o p \rightarrow Y^o\pi^+$ has two more constraints than the case $K^- p \rightarrow Y\pi^o$ and though of the same constraint class as $K^- n \rightarrow Y^o\pi^-$, avoids deuterium associated problems. The presence of the two additional constraints is of course dependent on a well determined incident $\overline{K}^o$ direction which in our case is known to better than ±1 mr in azimuth and ±2 mr in the dip angle.

B. Beam Line

A schematic illustration of the neutral beam line is shown in Fig. 3. The primary electron beam (with energies of 10-19 GeV and currents of 5-20 ma) first passed through a toroidal charge monitor[23] which integrated the total charge per pulse for purposes of beam normalization. The accuracy of this device was critical only in determination of yields from the target[24] and was not used in obtaining K_L^o fluxes at the bubble chamber.

The production angle of the neutral beam with respect to the electron beam could be varied from 1.5^o to 5° by a dipole magnet (18D72) placed immediately

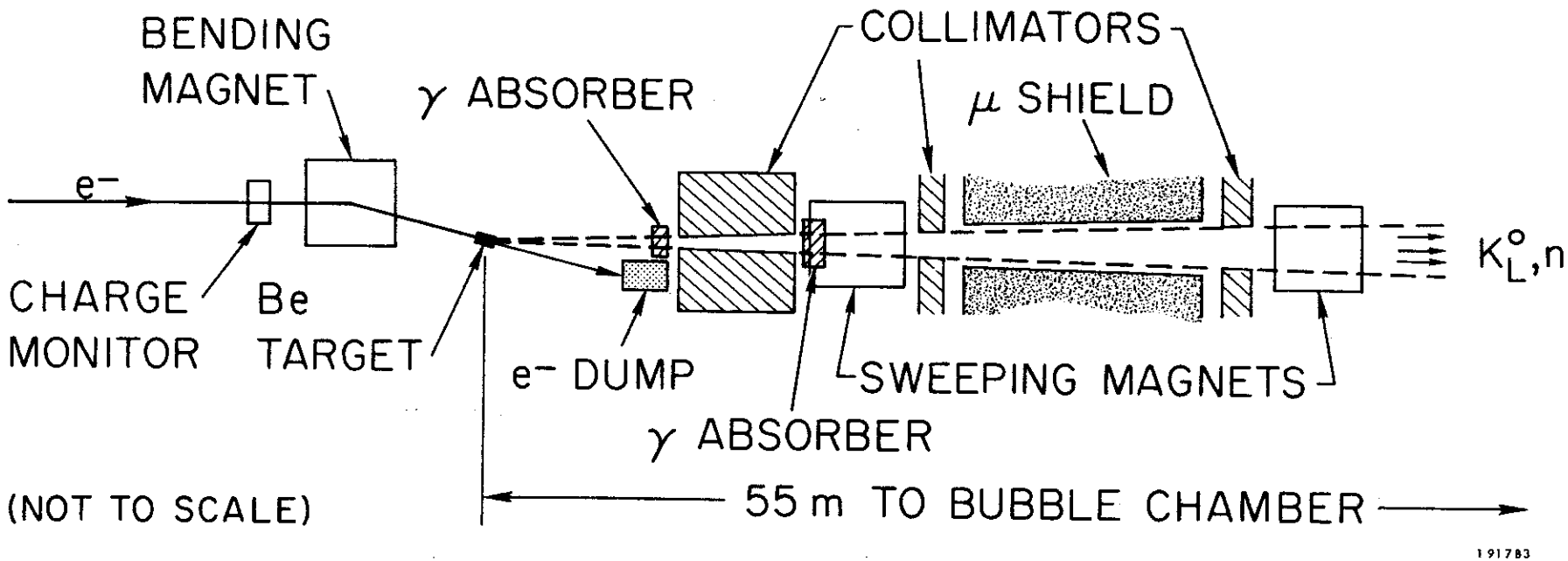

FIG. 3--Schematic illustration of the neutral secondary beam.

upstream of the beryllium target. The position, spot size, and angle of entry of the electron beam on the target was monitored visually by means of closed-circuit television displays of two ruled zinc sulfide screens. The first screen was attached to the upstream face of the target and the second was attached to the upstream face of a water cooled dump used to stop the electron beam.

The target itself consisted of 1.75 radiation lengths (0.70 r.l. in some cases) of Be. Beryllium was chosen as a best compromise since its low Z value minimized photon contamination in the beam while its high density (relative to other low A materials) allowed it to be of easily manageable size.

The neutral beam channel was defined by three carefully aligned lead collimators: a 2.2 meter tapered collimator centered 7 meters from the target, and two 0.5 meter untapered collimators located 10 meters and 22 meters from the target. Two sweeping magnets were used to remove charged particles. The halo of muons emerging from the target was absorbed by $\sim$ 15 meters of iron shielding surrounding the neutral beam channel. Photons in the beam were primarily removed by a 2-3 inch slab of tungsten and a remotely adjustable lead plug 6 to 9 inches thick. Slow neutrons were removed by compressed blocks of lithium hydride powder kept in an inert atmosphere. The presence of the absorbers had the additional effect of reducing the n/K_L^0 ratio as the amount of absorber was increased, since the nuclear absorption cross sections are larger for neutrons than for K_L^0 mesons.

At the bubble chamber, located 55 meters from the target, the beam had a cross sectional area of 15 cm by 40 cm and subtended a solid angle of $\sim 2 \times 10^{-5}$ steradian. Several factors contributed to the desirability of having the bubble chamber a sizeable distance from the target: such as; the need for small apparent target size to guarantee accurate knowledge of the K_L^0 direction,

the desire to further reduce stray muon background in the chamber, and the desire to enhance the high momentum K_L^o flux through attrition of the lower momentum components to compensate somewhat for reaction cross sections dropping with increasing beam momentum.

C. The Bubble Chamber

All the data were taken in the SLAC 40" hydrogen bubble chamber shown in Fig. 4. The chamber is cylindrical with a visible diameter of 1 meter and a depth of 50 cm and is illuminated by circular xenon flash tubes surrounding each of the three camera lenses. The light is then reflected back to the cameras by the retrodirective material Scotchlite which is glued to a dish attached to the chamber piston. Operating in this bright field illumination mode, only the light scattered away by the bubbles fails to reach the film. The only difficulty this causes is that the flashlamp voltages must be tuned to provide uniform exposure if the film is intended for measuring on the spiral reader.

The chamber is viewed by three lenses mounted on a 10 cm thick steel plate for stability and located at the vertices of an equilateral triangle about 70 cm on a side. The distance of the lens to the mid-plane of the chamber is 245.5 cm in space, resulting in a 17 degree stereo angle. After the light passes through the chamber window (Schottglass BK7), the quartz viewing ports, and lenses, it is bent by a 45 degree mirror and comes to a focus at the film plane, with an overall demagnification of 17 to 1. The film format was single strip, three view, on 70 mm film.

The chamber was operated at rates up to 5 pulses per second with a magnetic field of about 27 kilogauss, uniform to 4% over the illuminated volume. Operating temperatures and pressures resulted in a hydrogen density of 0.0594 gm/cc. The time from beam spill to expansion valley, light delay, and

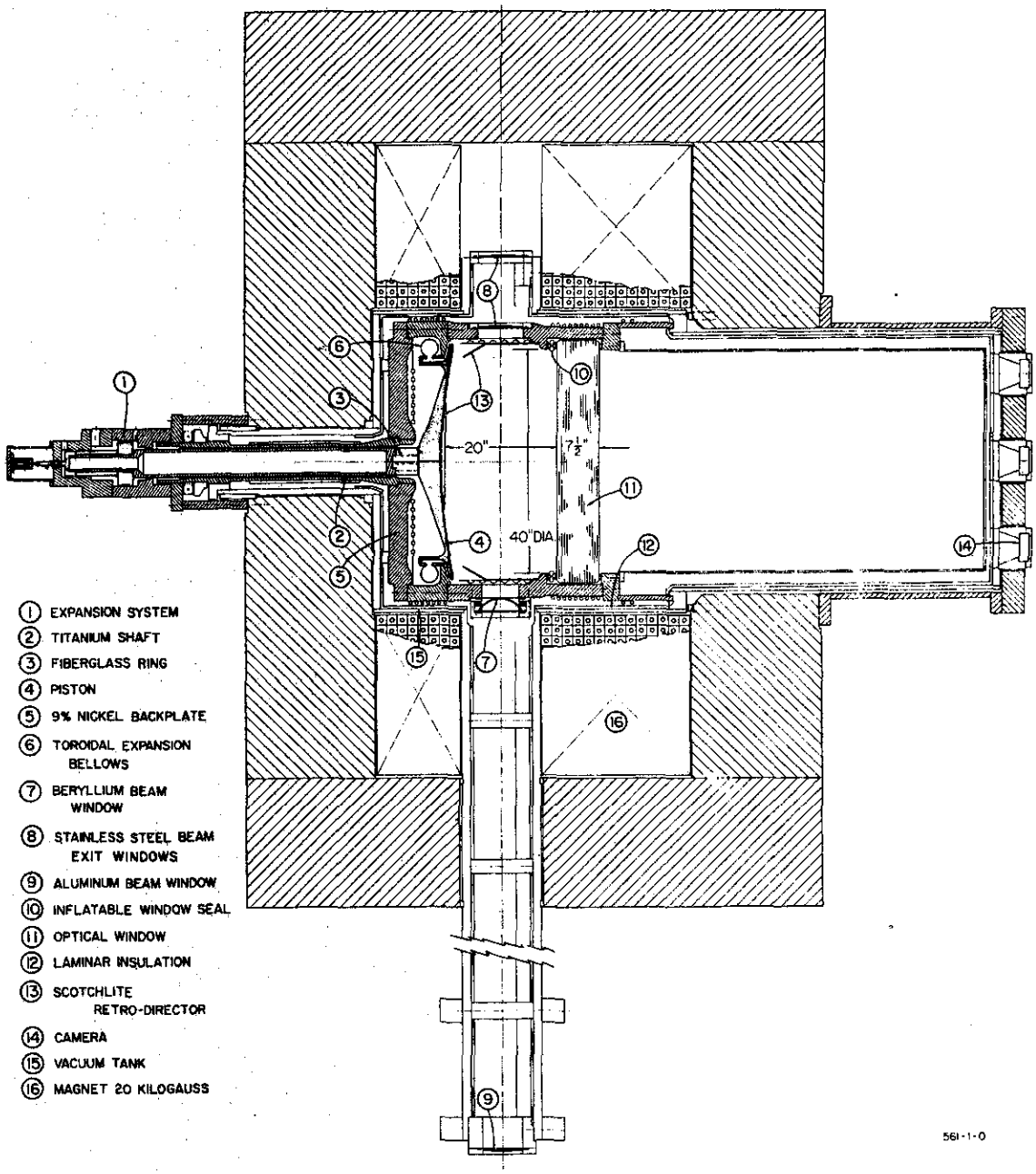

FIG. 4--The SLAC 40" Bubble Chamber.

vapor pressure (about 1 msec., 3 msec., and 67 psi. respectively) were monitored carefully to insure that the bubbles were of adequate size and density (10-15 bubbles per centimeter) for optimal measuring on the spiral reader. Stringent control was also maintained over film processing through frequent densitometer checks to provide a background density most appealing to the reader's AGC circuits.

D. Time-of-Flight-System

Not shown in Fig. 4 is an array of 12 counters surrounding the exit window side of the chamber's 2.9 inch stainless steel vacuum jacket. The scintillators were connected via light pipe to phototubes outside of the magnet, and these signals, together with a time mark from a small Cerenkov counter just upstream of the Be target, were fed into a PDP-9 for time-of-flight evaluation. Using this information a decision could then be made to trigger or not trigger the flashtubes for a picture. Time-of-flight information was gathered for much of the film while triggering on the basis of this information was done for only about 150 rolls. Since the reaction channels to be discussed here do not make use of the timing information, further detail of the system's operation is not warranted. A discussion on the use of the triggered film will be covered elsewhere in this paper.

E. Scanning

Scanners were instructed to record all topologies found on the film. Topologies were categorized by a three digit event code, $N_1 N_2 N_3$, where N_1 is the number of charged tracks emerging from the main vertex, N_2 indicates the number of vees which pointed to the main vertex or to a kink on one of the charged primary tracks, and N_3 indicates the number of kinks present on the charged tracks and whether the kink occurred on a positive or negative track.

Vees which pointed to a main vertex in all three views were considered associated with that event while all others were recorded as unassociated vee events, i.e., event type (ET) 200. Hence the final states $\Lambda\pi^+$ and $\Sigma^0\pi^+$ are both categorized at ET 110 while beam decays are classified as ET 200. Vees with an apparent zero degree opening angle in all three views and with at least one track having a radius of curvature of less than 10 inches were discarded as $\gamma \rightarrow e^+e^-$ events. One weakness of these scanning rules is that Ξ^0 events are not properly scanned for, as the vee points to the invisible Ξ^0 decay point rather than to the main vertex. Care was taken to insure the correct association to interactions. In cases of doubtful association of a vee, the scanners were instructed to assign the vee to the "n-prong-vee" category rather than the ET 200 category. In cases of ambiguous main vertex associations of a vee, both main verticies were recorded and a multiple association flag set. After measurement of all "n-prong-vee" events, those vees which were really K_L^0 beam decays were identified and reassigned (this amounted to a 8% increase in the number of K_L^0 beam decays).

The data were taken in four distinct periods (November 1968, August 1969, December 1970 and January 1971). Excluding some unmeasurable film taken during one run, about one million frames (670 rolls at 1500 pictures per roll) were scanned. All of the ET 110 events in this sample of film were measured except for those declared unmeasurable because of problems such as obscured vertices or serious track scatters.

About 13% (88 rolls) of the film was scanned a second time and a comparison made with data summary tapes (DST) resulting from events detected on the first scan. The resulting efficiencies are given below.

Data	Scan Efficiency	No. Rolls in 2nd Scan
ET 110; $(\Lambda, \Sigma^0)\pi^+$ Fits		
Run I	92 ± 2%	36
Run II	90 ± 2%	52
ET 200; Beam Decays		
Run I	92 ± 1%	36

As will be shown later, the only important quantity for cross section determinations will be the relative event/flux scanning efficiency for Run I, and this is seen to be consistent with unity. It is worth noting that the rolls selected for second scanning sample the two runs quite uniformly, rather than being consecutive rolls from one part of each run. Also worth mentioning is that although no second scanning was done for Runs III and IV the efficiency is probably quite close to that for Run I as the relative event densities per frame for the four runs were 1, 5/3, 2/3, and 1/2 respectively.

F. Event Processing

The scan information was recorded vocally by the scanner onto small dictation machines. Keypunch operators then played back the tapes and recorded the information onto punched cards. The cards were then fed to a library program which produced a Master List. The Master List and associated handling programs were the key to efficient processing and accurate bookkeeping, and it was from the Master List that measurement request cards and tapes came.

The events were measured at SLAC on conventional NRI film plane measuring machines on-line to an ASI 6020 computer and on the SLAC spiral reader. Each event was measured in all three views and in each view four fiducial marks

were measured to aid in spatial reconstruction. Geometrical reconstruction and hypothesis fittings were done by the programs TVGP and SQUAW[25] on SLAC's IBM 360 Model 91. As this was the first experiment to be measured on the spiral reader, extensive tests were conducted to determine its accuracy. In one such test a sample of ~ 900 events fitting the three-constraint reaction $np \rightarrow pp\pi^-$ showed that the average RMS scatter of points about TVGP reconstructed tracks for spiral reader measured tracks was within 1 least count of the NRI value of ~ 5 least counts (1 least count = 2.54 microns). In another such test a comparison was made of mass resolution using similar samples of vees giving 3-C fits to $K_S^0 \rightarrow \pi^+\pi^-$. The NRI measurements gave a mass and width of 497.8 ± 3.8 MeV, while the spiral reader gave 498.1 ± 4.2 MeV. This small difference in resolution is unlikely to be noticeable in most physics applications.

With regard to the overall accuracy of reconstructed points, A. Levy and G. Wolf[26] have performed a study of the SLAC bubble chamber analysis system, consisting of the 40" chamber, the NRI measuring machines, and the TVGP geometrical reconstruction program with the TVGP optical constants determined by fiducial measurements.[27] They photographed fast muons in the chamber with the magnetic field off. Distortions due to multiple scattering were eliminated by adding together the effect of many tracks in the same region of the chamber. In this way no systematic distortions were found in either of the directions normal to the beam directions. The upper limits for such distortions were 50 microns in the visual plane (y direction) and 250 microns normal to the visual plane (z direction). From a fit to the curvature a maximum detectable momentum of P(MDM) = 1600 (+2400, -600) GeV/c was found by assuming a magnetic field of 26 kG and 100 cm of track length.

Surveys of the chamber and top glass fiducials were taken before each experimental run and together with corresponding fiducial measurements from the film were used to determine the optical constants as well as various distortion parameters. Measurement uncertainties and the overall setting error were adjusted to give unit width pull distributions centered at zero. Target position errors were somewhat over-estimated in order to prevent the loss of good events, and it is now felt that the overall setting error used was slightly too large. This is not a serious problem but does result in the somewhat skewed confidence level distributions (Fig. 5) of the 6-C $\Lambda\pi^+$ fits and the 4-C $\Sigma^0\pi^+$ fits. Fine tuning of the magnetic field was accomplished by requiring the K_s^0 mass to agree with the published value of 497.79 MeV.[28]

G. Special Scans

Following TVGP-SQUAW processing an update of the master list was done so that remeasure requests could easily be made. Especially difficult events were remeasured on the NRI machines. In addition, TVGP-SQUAW information was used to generate directed or resolve scans. The first of these resolve scans was done to confirm the hypothesis that decisions to reassign events improperly scanned as "n-prong-vee" events to the beam decay category (ET 200) could be made by the computer.

The second resolve scan was an attempt at estimating the number of "n-prong-vee" events improperly scanned as unassociated vee events. Two-prong events which SQUAW indicated as possible Λ or K_s^0 decays (Λ candidate if 0-C P π^- mass in range 1110 to 1120 MeV; K_s^0 candidate if 0-C $\pi^+\pi^-$ mass in range 485 to 510 MeV) were listed and scanners then carefully checked the vicinity of each event for a possible main vertex. This was done for a sample of 29 rolls from Run I, and events for which a possible association was found

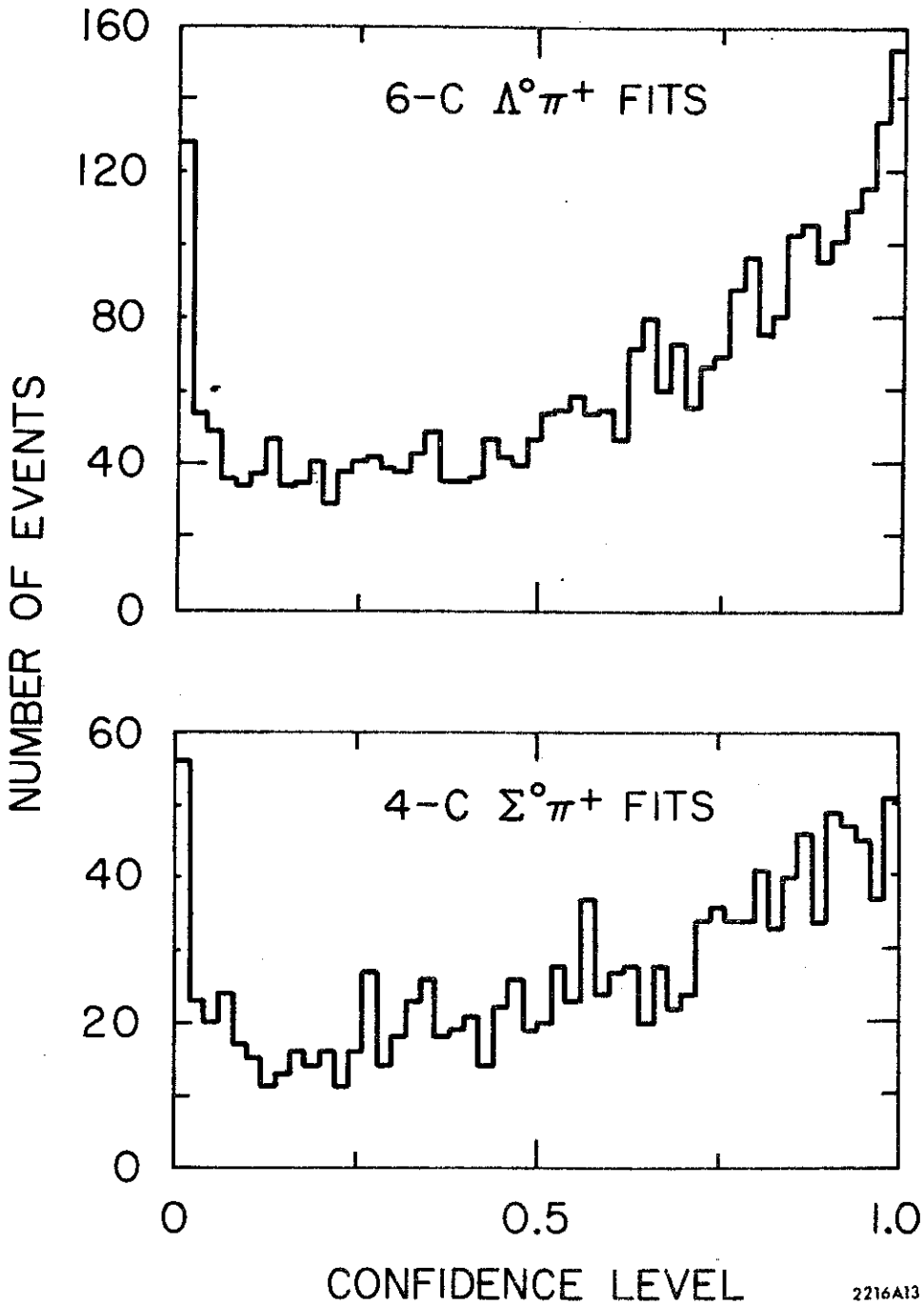

FIG. 5--Confidence level distributions for events fitting the hypotheses $\overline{K}^{o}p \rightarrow \Lambda\pi^{+}$ and $\overline{K}^{o}p \rightarrow \Sigma^{o}\pi^{+}$.

were remeasured and reprocessed. Results indicated that an additional $6.8 \pm 0.7\%$ more ET 110 events with an associated Λ^0 could be recovered from the ET 200 category. About the same increase was obtained for ET 110's with an associated K_s^0, while ET 310's gained only about 2%, indicating, not surprisingly, that association of vees to three-prong verticies is more reliably done than to one-prong vertices.

There is a small problem of double-counting of losses if one includes the above correction as well as the scanning efficiency correction, since some ET 110 events failed to appear in the second scan simply because they were improperly scanned as ET 200 events. The amount of over-correction for ET 110 events with associated Λ vees has been found to be 2%.

CHAPTER 3

Spectral Shapes and Flux

Accurate determination of the spectral shapes and absolute flux in this experiment was essential for extracting good cross section measurements. In the early stages of the experiment only the spectral shape was determined so that we were forced to normalize our data to reaction cross sections obtained in other experiments. This was not only esthetically unsatisfying but also quite inaccurate since the scale factor for the entire experiment rested on the small sample of events to be found in a narrow slice of beam momentum.

A. A First Approximation

As the first rolls of film were being taken a quick estimate of the beam spectrum shape was desired for optimizing the beam conditions (i.e., electron energy and production angle). The film was scanned by physicists and scanners for two prong events which pointed within five degrees of the beam direction. (5° rule dropped for obvious low momentum events below 2 GeV/c.) Only clearly associated events and obvious $e^{+}e^{-}$ pairs were rejected. Curvature templates were then used to measure the visible momenta, and a rough spectrum was generated by assuming that about two-thirds of the beam momentum is visible in these three body decays. Although the template measurements of momenta were good to only 10% and the procedure subject to 10-20% contamination from K_S^o decays, the results were adequate for engineering purposes, and the technique was suggestive of the more refined procedure finally used and to be described below.

B. Selection of Events

The film was scanned for the visible K_L^o decays: $K_L^o \rightarrow \pi^{\pm}e^{\mp}\nu$, $K_L^o \rightarrow \pi^{\pm}\mu^{\mp}\nu$, and $K_L^o \rightarrow \pi^{+}\pi^{-}\pi^{o}$. These decays appear mainly as two-prong events which are

not associated with any interaction in the chamber. However, as mentioned before, a small fraction of the final sample of events (8%) were first classified by the scanners as associated with an interaction in the chamber but were properly classified as beam decays following measurement. The events were measured and processed through TVGP and SQUAW. Each of the five, zero constraint, decay hypotheses were attempted and events were included if any one of the hypotheses gave a fit. As to be expected with 0-C fits, many events give multiple solutions.†

Events were excluded if any of the following were satisfied:

$$M(e^+e^-) < 35 \text{ MeV},$$

$$485 < M(\pi^+\pi^-) < 510 \text{ MeV},$$

or

$$1110 < M(p\pi^-) < 1120 \text{ MeV},$$

where the charged tracks were interpreted as the indicated particles. These cuts, which effectively remove all non-K_L^o decays, also remove a small fraction (~ 5%) of the K_L^o decays. However, these cuts introduce no bias since the same cuts are made on the Monte Carlo events used in the theoretical analysis. A final selection required the K_L^o decay to occur within a 55 cm long decay volume within the chamber.

C. Determination of the K_L^o Momentum Spectrum at the Bubble Chamber

The method used determines both the shape and the absolute magnitude of the K_L^o momentum spectrum at the bubble chamber from the observed distribution of the visible momentum, p_{VIS}, defined as

$$p_{VIS} = \hat{n} \cdot (\vec{p}_1 + \vec{p}_2)$$

† A small fraction of true K_{e3} decays failed to have a kinematic solution due to measurement resolution or small angle scatters on the electron track. Events in this category are readily identifiable and have been included in the analysis of the K_L^o spectrum. Only 7% of the total sample are in this category.

where $\vec{p}_1$ and $\vec{p}_2$ are the three-momenta of the two charged tracks and $\hat{n}$ is a unit vector along the beam direction. The procedure, as illustrated in Fig. 6, consists of first generating the p_{VIS} distribution that would be observed in the decay of K_L^o particles with a prescribed momentum. These distributions (histograms (a) - (s)) are produced in a Monte Carlo program by allowing the K_L^o to decay into the various modes as specified by the known branching ratios and decay matrix elements and finally by averaging over a band in K_L^o momentum (e.g., 0.0-0.4 GeV/c for distribution (a)). The contribution of each distribution is then varied until the sum of the distributions best duplicates the observed p_{VIS} distribution, as measured by minimizing chi squared. Errors on the resulting momentum spectrum, $Z(p_K)$, are obtained by allowing random fluctuations in the p_{VIS} data distribution and repeating the iteration procedure to obtain the change in $Z(p_K)$. The fluctuations in a single p_{VIS} bin containing N events are Gaussian distributed with standard deviation $N^{1/2}$.[24]

The absolute flux of K_L^o at the chamber, denoted by $F(p_K)$, is related to $Z(p_K)$ as follows:

$$F(p_K) = \frac{1}{\epsilon r}\left[1 - e^{-L/\lambda(p_K)}\right]^{-1} Z(p_K)$$

where

ϵ = efficiency factor for scanning and measuring two prongs

r = branching ratio, $(K_L^o \rightarrow \text{charged})/K_L^o \rightarrow \text{all})$,

$\lambda(p_K) = \frac{p_K c\tau}{m_K}$, the mean K_L^o decay length,

L = length of decay volume in the chamber,

m_K = K_L^o mass,

and τ = K_L^o lifetime.

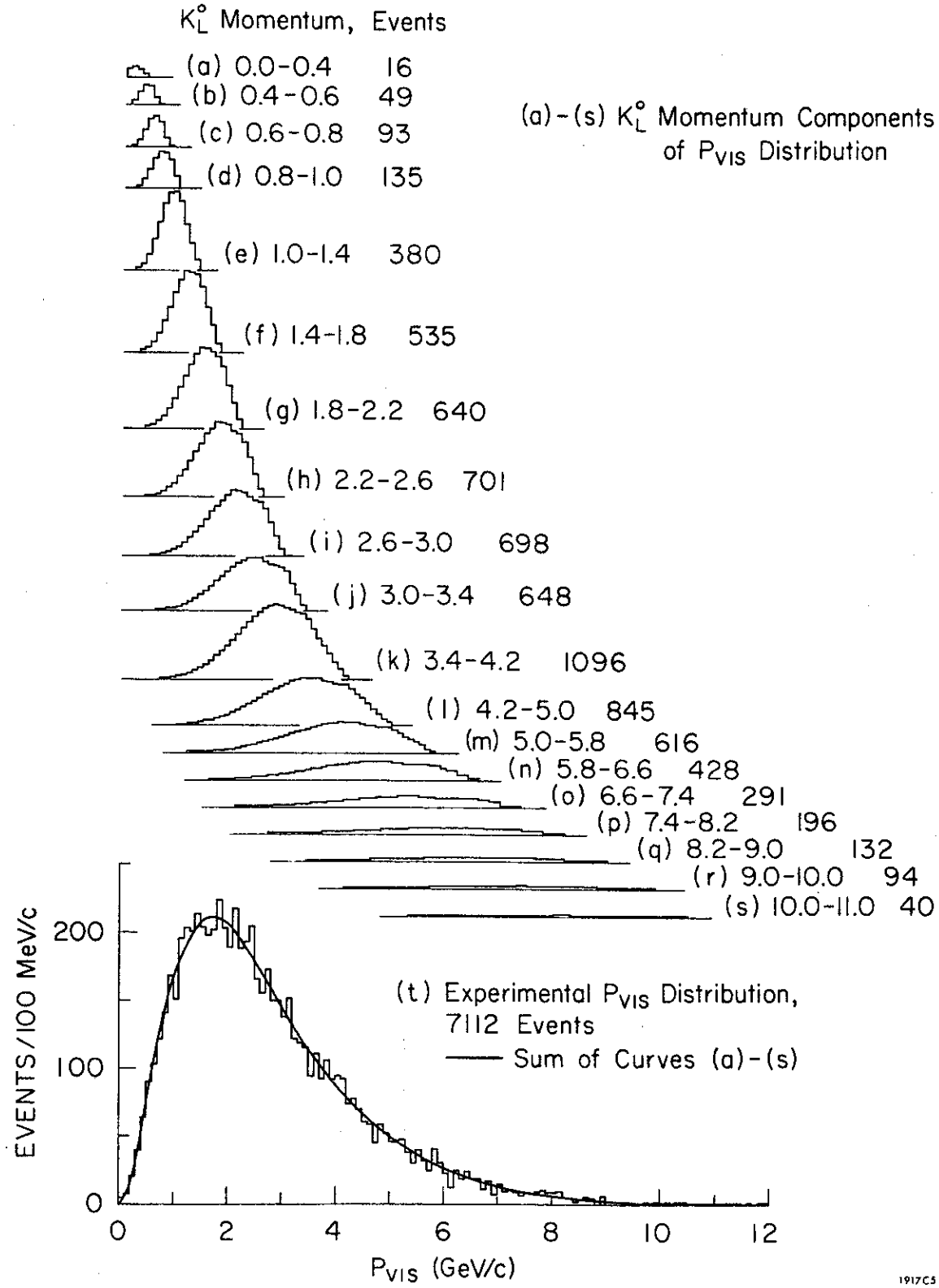

FIG. 6--Distribution in P_{VIS} used to determine the K_L^o momentum spectrum from 16 GeV electrons incident at 2° production angle on a 1.75 r.l. Be target.

An example of the K_L^o flux at the chamber is shown in Fig. 7 (solid dots). The uncertainties shown are the statistical uncertainties determined as described above.

As a check of the preceeding method an alternate approach[29] was taken using only the K_{e3} decays which were uniquely identifiable by a transverse momentum selection. The results are shown (open dots) in Fig. 7 and compare well with the results of the previous method. Also shown (solid squares) is the neutron flux obtained for the same beam conditions (2° production by 16 GeV electrons on 1.75 r.l. Be target) and determined by comparing the number of $np \rightarrow pp\pi^-$ events in our experiment with published values of $\sigma(np \rightarrow pp\pi^-)$.

D. K_L^o Spectra — Results and Errors

The experiment was analyzed in terms of four distinct beam spectra; Run I composite and 1.6^o K_L^o production at 16, 18, and 19 GeV electron energies. Run I actually consisted of a wide range of operating conditions, but as every beam decay, as well as every ET 110 event, was processed, creation of a composite spectrum for this run was not only possible but highly desirable. The intensity profiles and their percentage statistical errors are given in Table 1 for each of the spectra. Since the beam decays for the 16, 18, and 19 GeV, 1.6^o exposures were measured for only a fraction of the film, the numbers indicate only the spectral shape, while the Run I composite numbers have the added significance of being the flux of K_L^o particles ($\times 10^{-3}$ per 200 MeV/c).† The spectra are also displayed in Figs. 8 and 9.

E. Absolute Normalization

Knowledge of the absolute flux for Run I permits calculation of cross sections without dependence on other experiments. At the base of Fig. 8 are the

† Run I composite flux as tabulated was computed assuming $\epsilon = 1$.

TABLE 1

Spectral Shapes and Errors

P_{BEAM} (GeV/c)	Run I Flux	Run I % Error	16 GeV Shape	16 GeV % Error	P_{BEAM} (GeV/c)	18 GeV Shape	18 GeV % Error	19 GeV Shape	19 GeV % Error
0.0 - 0.2	.048	80.	.159	83.	0.0 - 0.2	.265	59.	-.020	2055.
0.2 - 0.4	.248	49.	1.17	61.	0.2 - 0.4	.752	42.	.328	68.
0.4 - 0.6	2.59	8.3	4.45	24.	0.4 - 0.6	1.90	33.	4.61	20.6
0.6 - 0.8	7.68	5.4	12.8	10.9	0.6 - 0.8	5.68	19.2	12.7	12.4
0.8 - 1.0	15.0	3.6	28.2	6.9	0.8 - 1.0	12.9	11.4	23.6	8.0
1.0 - 1.4	29.4	2.4	63.3	5.4	1.0 - 1.4	29.5	6.5	44.4	4.9
1.4 - 1.8	53.7	2.2	131.	4.5	1.4 - 1.8	61.2	4.6	80.1	3.9
1.8 - 2.2	79.1	2.2	213.	3.6	1.8 - 2.2	99.3	4.5	123.	4.2
2.2 - 2.6	102.	2.2	297.	3.6	2.2 - 2.6	138.	4.9	166.	4.6
2.6 - 3.0	117.	2.2	361.	3.5	2.6 - 3.0	171.	5.0	201.	4.7
3.0 - 3.4	125.	2.2	402.	3.1	3.0 - 3.4	196.	4.6	225.	4.5
3.4 - 4.2	127.	2.8	442.	3.3	3.4 - 4.2	222.	4.2	244.	4.2
4.2 - 5.0	117.	3.2	483.	3.4	4.2 - 5.0	234.	3.8	243.	4.0
5.0 - 5.8	99.9	3.8	470.	3.2	5.0 - 5.8	224.	3.9	228.	4.0
5.8 - 6.6	78.1	3.9	407.	3.7	5.8 - 6.6	199.	4.3	209.	4.4
6.6 - 7.4	58.5	4.7	324.	4.6	6.6 - 7.4	169.	5.1	188.	5.1
7.4 - 8.2	42.8	11.4	241.	5.5	7.4 - 8.4	136.	6.0	162.	5.9
8.2 - 9.0	32.2	8.1	170.	6.4	8.4 - 9.4	105.	6.4	130.	5.8
9.0 - 10.0	20.5	10.6	98.9	10.0	9.4 - 10.4	74.8	8.1	94.8	6.9
10.0 - 11.0	10.2	22.	44.4	19.2	10.4 - 11.4	47.9	12.9	63.9	11.4
11.0 - 12.0	5.59	33.	17.8	30.	11.4 - 12.4	26.4	20.2	39.3	16.9
12.0 - 13.0	3.92	42.	9.97	76.	12.4 - 13.6	10.2	51.	20.5	25.7
13.0 - 14.0	-.043	113.	7.05	103.	13.6 - 14.8	1.63	185.	8.75	64.
14.0 - 15.0					14.8 - 16.0			3.02	121.
No. Events in Data Distrib.	11880		4195			2115		2466	
No. Events in Fit. Distrib.	12812.8		4532.4			2305.7		2684.2	
No. p_{VIS} Data Bins	86		70			78		78	
No. P_{BEAM} Bins	23		23			23		24	
χ^2/NDF	73.6/63		65.1/47			75.1/55		70.9/54	

Units of flux are in number of $K_L^0 \times 10^{-3}$ at H.B.C./200 MeV/c

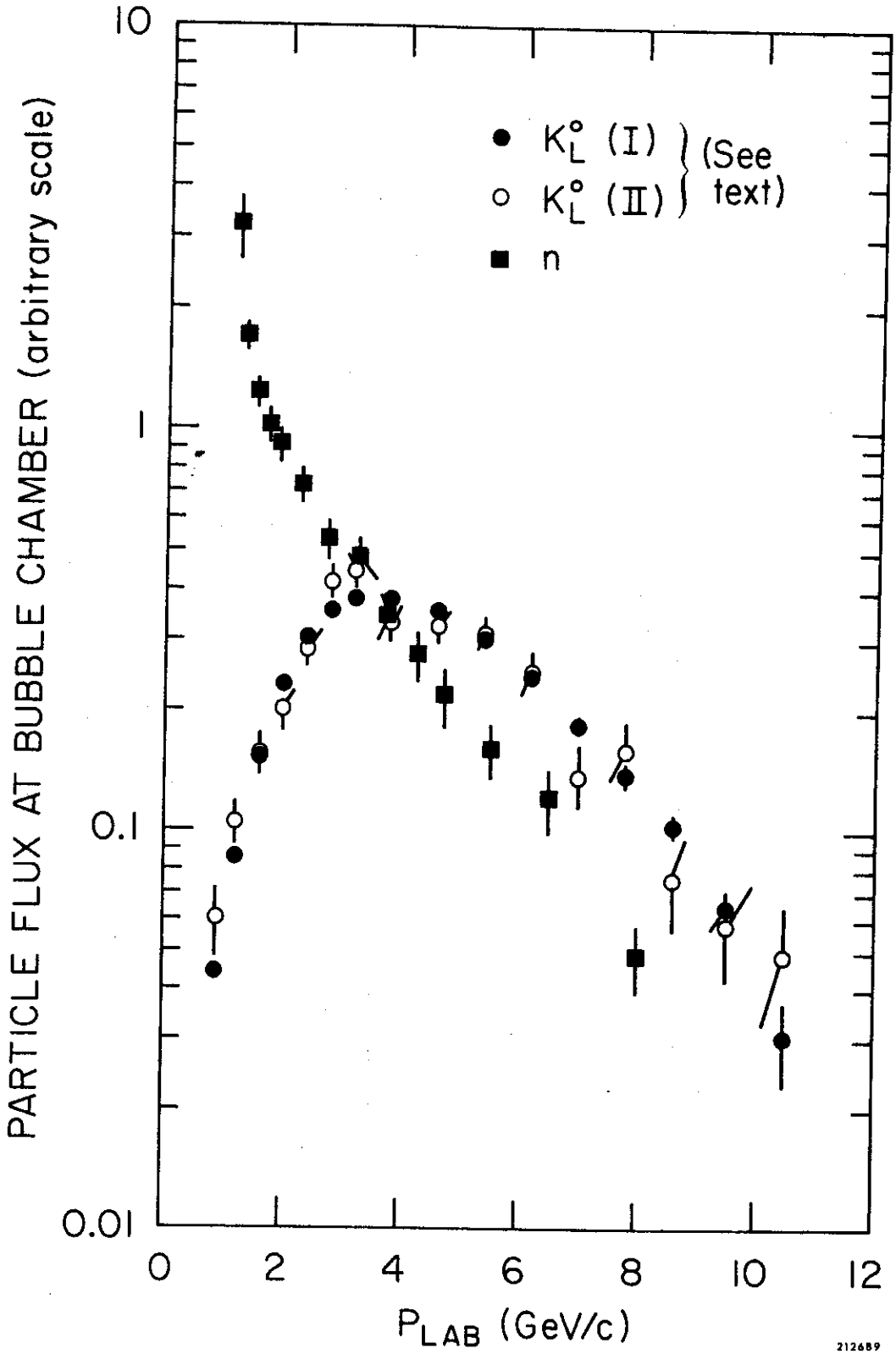

FIG. 7--Comparison of the K_L^o flux (○, ●) and neutron flux (■) at the hydrogen bubble chamber. The solid and open circles result from different methods of analysis of the K_L^o spectrum (see text).

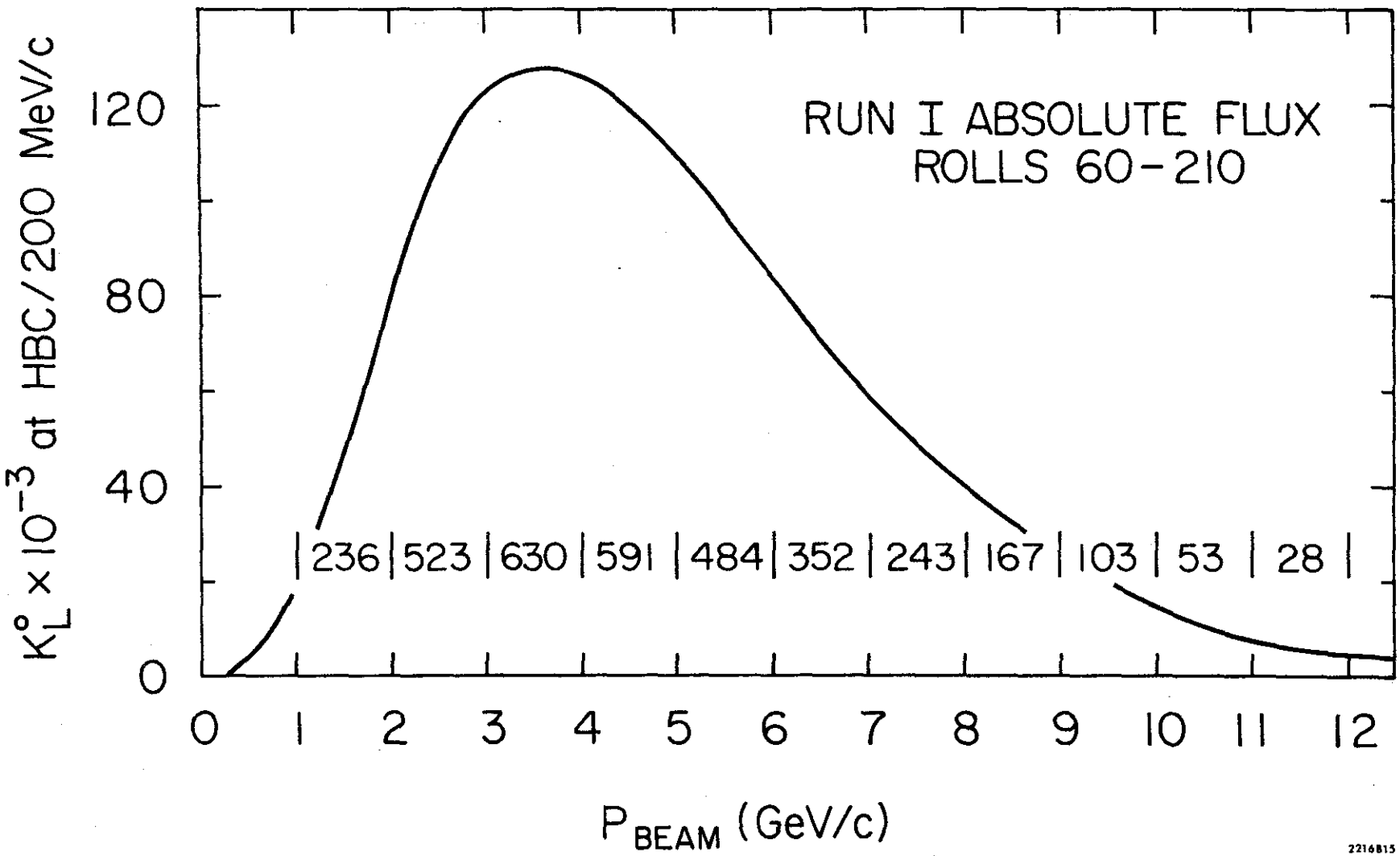

FIG. 8--Absolute K_L^o Flux as a function of incident momentum.

integrated number of K_L^o beam particles ($X10^{-3}$) per GeV/c in the Run I film and taken together with the $\Lambda^o\pi^+$ and $\Sigma^o\pi^+$ events from the same film enables computation of $<\sigma> \equiv <\sigma_{\Lambda\pi}> + <\sigma_{\Sigma\pi}>$, where averaging over a wide region of beam momenta is done to improve the statistical accuracy of $<\sigma>$. This cross section averaged from 2 GeV/c to 6 GeV/c sets the scale when all the data are used in conjunction with the overall composite spectrum.

F. Overall Composite Spectrum

The advantage of combining the four spectra to produce an overall composite spectrum, rather than weighting events by the inverse of the flux for the appropriate run, is purely statistical. In combining N events with weights w_i we find that the fractional error, $[\Sigma w_i^2]^{\frac{1}{2}}/\Sigma w_i$ on the quantity Σw_i is minimized when the w_i have minimal dispersion. This is easily seen since for the trivial example of no dispersion, i.e., all w_i identical, the fractional error achieves its absolute minimal value of $N^{-\frac{1}{2}}$.

Were all the fluxes known, the composite flux would simply be $F_C(p) = \sum_{j=1}^{4} F_j(p)$; however, only the shapes $S_j(p)$ are given, which leaves the proportionality constants α_j, where $F_j(p) \equiv \alpha_j S_j(p)$, yet to be determined. Now weighting events by $S_j^{-1}(p)$ leads to unnormalized cross sections W_j, which are simply related to the actual cross sections by the relations $\sigma_j = W_j/\alpha_j$, and since in the limit of infinite statistics $\sigma_i \rightarrow \sigma_j$, one concludes that $\frac{W_i}{W_j} \rightarrow \frac{\alpha_i}{\alpha_j}$. Fixing one of the α_j ($\alpha \equiv 1$ for Run I) then unambiguously defines the remaining α_j. Values of α_j are given in Table 2 and are based on the sum of the unnormalized cross sections W_j for $\Lambda\pi^+ + \Sigma^o\pi^+ + K_S^o p$ final states averaged over incident momenta from 2 GeV/c to 8 GeV/c (3-8 GeV/c for triggered film).

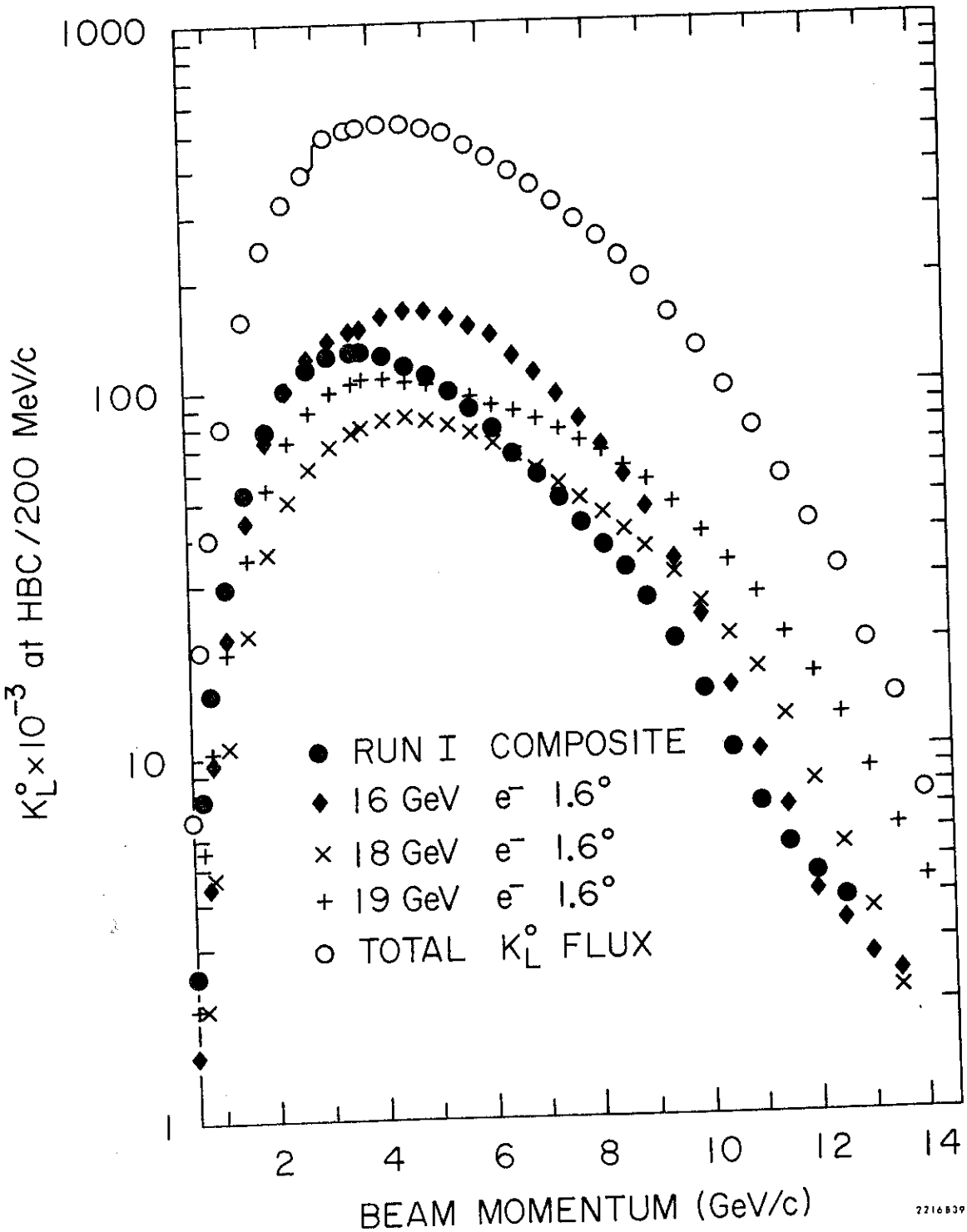

FIG. 9--Beam flux versus incident K_L^o momentum. Only the Run I (●) flux has been determined absolutely. The fluxes shown for the 16, 18, and 19 GeV e^- at 1.6^o (◆, X, and +) exposures are derived from the unnormalized intensities of Table 1 times the α coefficients of Table 2. The discontinuity at 3.0 GeV/c in the total K_L^o flux (○) is due to the use of the triggered film from the 19 GeV e^- exposure only for K_L^o momenta greater than 3.0 GeV/c (see text).

TABLE 2

Spectrum	No. Events (All Mom.)	No. Events (2–8 GeV/c)	α
Run I	1879	1005	$\equiv 1.0$ (±3.2%)
16 GeV 1.6°	1981	1181	0.342 (±2.9%
18 GeV 1.6°	986	609	0.363 (±4.1%)
19 GeV 1.6° (untriggered)	1390	835	0.439 (±3.5%)
19 GeV 1.6° (triggered)	863	261	0.247 (±6.2%)

In producing the final composite spectrum (Fig. 9, open dots), additional corresponding momentum points are taken from smooth curves drawn through the component spectra to bring the number of sampling points to about 40. After summing with the appropriate α coefficients a composite spectrum is ready for insertion into cross section programs, where the flux is computed by linear interpolation of the composite for each event according to its incident beam momentum value.

G. Use of Triggered Film

Of the 370 rolls of film taken with 19 GeV electrons on Be and a 1.6° production angle, 219 rolls were taken without triggering, while the remaining 151 rolls were taken using time-of-flight information as a trigger. In particular, the trigger conditions were set to fire on events with a K_L^0 beam momentum of less than 2.5 GeV/c. Since there were as many as 10 interactions per frame (including one-prongs) and since only one of the many events need meet the triggering condition, one expects rather non-selective triggering. This was indeed observed to be the case as our picture taking rate dropped by only a

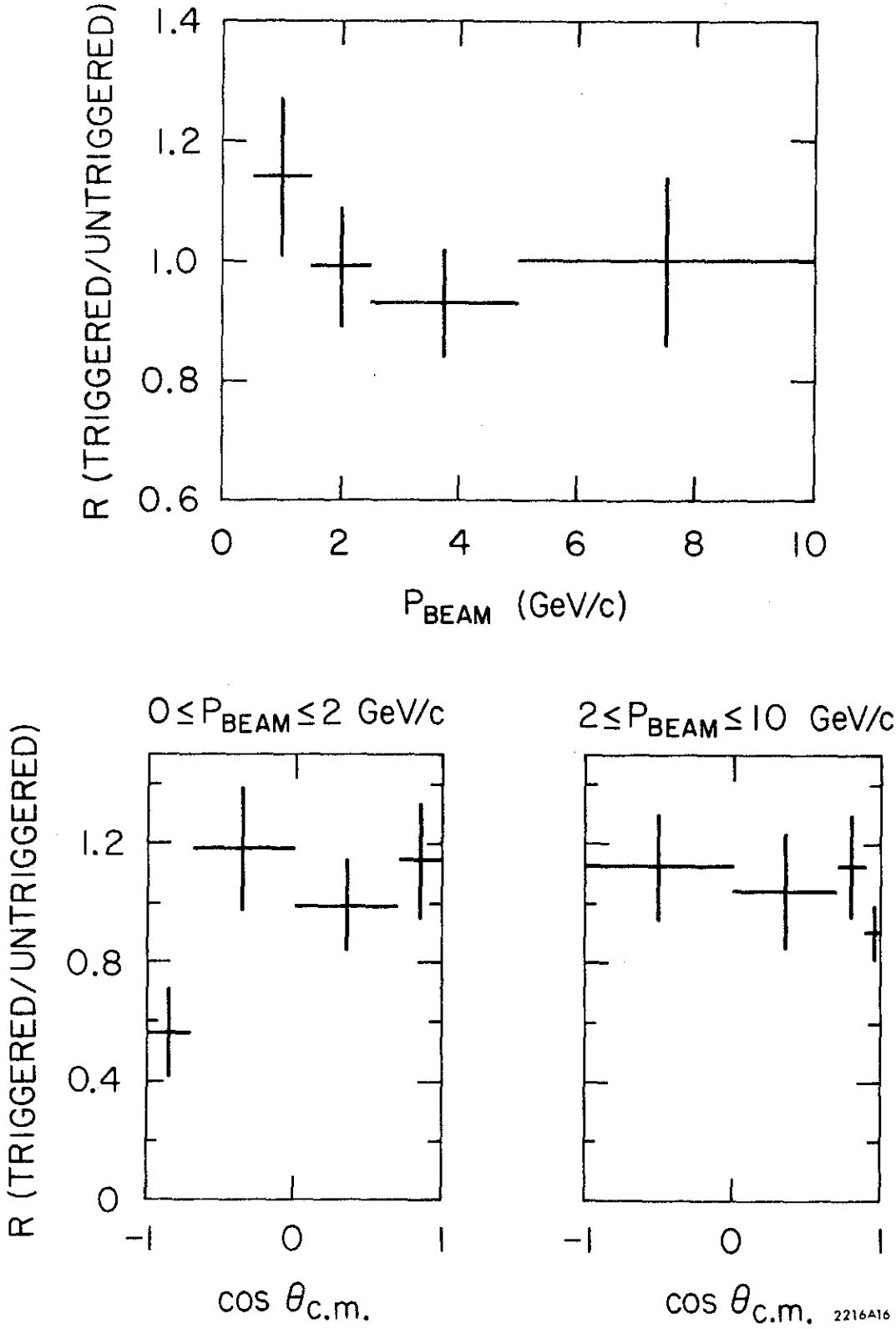

FIG. 10-- Comparison of triggered to untriggered $\pi^+(\Lambda, \Sigma^0)$ data from the 19 GeV, 1.6^0 e^- exposure. Upper figure shows relative event abundance versus beam momentum. Lower figure shows relative detection efficiency versus $\cos\theta_{c.m.}$ for the events below 2 GeV/c (left) and above 2 GeV/c (right). To avoid biases, triggered data with $P_{BEAM} < 3$ GeV/c have been eliminated from the data sample.

factor of 2 to 3. The net result is that one expects negligible bias to high momentum event distributions as the presence of these events is uncorrelated with the triggering condition. In Fig. 10 the triggered and untriggered data for $\overline{K}^0 p \rightarrow (\Lambda, \Sigma)\pi^+$ are compared by plotting the quantity $R = \frac{\text{No. Triggered}}{\text{No. Untriggered}} \times C$ ($C \equiv$ TOTAL NO. UNTRIGGERED EVENTS/TOTAL NO. TRIGGERED EVENTS) as a function of beam momentum (upper) as well as center of mass scattering angle (lower) for low and high momentum data. The data show a slight detection enhancement below 2 GeV/c, as expected, and an accompanying detection efficiency bias in the angular distribution of these low momentum events, as evidenced by a severe relative efficiency loss for backward events. For the higher momentum events no such non-uniformity is seen in the angular distribution so that it is considered reasonable to make use of the triggered data with incident momenta above a conservative cutoff momentum, chosen to be 3 GeV/c. Care was also taken to insure that the additional beam flux coming from the triggered film sample was added to the total flux only above the 3 GeV/c cutoff.

CHAPTER 4

Cross Sections

A. Biases in the Data

Though in principle the bubble chamber is a detector with complete 4π steradian detection capabilities, in practice some events are effectively invisible to the scanner either because of the geometrical orientation of the event or due to the momenta of the tracks involved, while some other events, though easily found, consistently fail in reconstruction. Fortunately there is often an isotropy condition or known decay distribution available for observing and correcting a given bias.

1. Azimuthal Symmetry About Beam

In general there is a loss of steeply dipping tracks,which in the case of the reaction $K_L^o p \rightarrow K_S^o p$ appeared as hole in the azimuthal distribution of events about the beam direction since short steeply dipping protons were very hard to find and reconstruct. However, in the case of the reactions $\overline{K}^o p \rightarrow (\Lambda, \Sigma^o)\pi^+$ this distribution is quite flat, for $p_\Lambda > 314$ MeV/c, as seen in the twice folded distribution about beam azimuth of Fig. 11a. In the vicinity of 90°, where the production plane of an event is virtually parallel to the camera axis, the losses are negligible, and attempts to correct for a possible loss in four of the steeper azimuth bins leads to the null correction factor of 1.008 ± 0.009. For events with slower recoil lambdas there are visible losses in this distribution and a correction factor of 1.05 ± 0.02 is called for; however, the loss is much more strongly correlated with the orientation of the lambda decay plane rather than with the orientation of the overall production plane. Hence, we proceed to a study of Λ decay distributions after being assured that the azimuthal distribution of the π^+ about the beam direction is flat as expected.

2. Λ Decay Losses

In considering the decay of the Λ there are really two distributions which should be viewed simultaneously,as the losses in each are strongly correlated with one another. One is the orientation of the Λ decay plane with respect to the camera axis while the other is the helicity cosine distribution of the proton in the Λ rest frame with the Λ direction in the lab defining the $\hat{z}$ axis. This pair of distributions is shown in Fig. 11b for a narrow range of Λ momenta. The helicity cosine distribution has losses near the backward direction because here the decay protons emerge with momenta low enough to make detection of the proton track difficult. In fact the magnitude of this effect can be exactly computed (Fig. 12) if one assumes a minimum detectable proton momentum, p_{CUT}, corresponding to a known stopping distance, ℓ_{STOP}, in liquid hydrogen. Similarly, the azimuthal distribution of the Λ decay plane shows losses when the plane is nearly parallel to the camera axis. The two dimensional histogram of these two distributions has been analyzed for various Λ^0 momentum intervals and the Λ detection efficiencies given in Table 3a. It is worth noting that the helicity cosine distribution shows a loss even for very fast lambdas; not however because of slow protons since there are none, but rather because of very slow π^- particles ($P_{\pi^-} < 40$ MeV/c corresponds to track lengths <1.5 cm).

3. Vee Detection Efficiency Versus Length

Another possible source of substantial bias comes from the loss of very short and very long vees. It is therefore desirable to know the detection-processing efficiency for lambdas as a function of their distance from the main vertex. Once this efficiency profile is known, minimum and maximum cutoffs in vee length can be chosen and events properly weighted for cross section distributions.

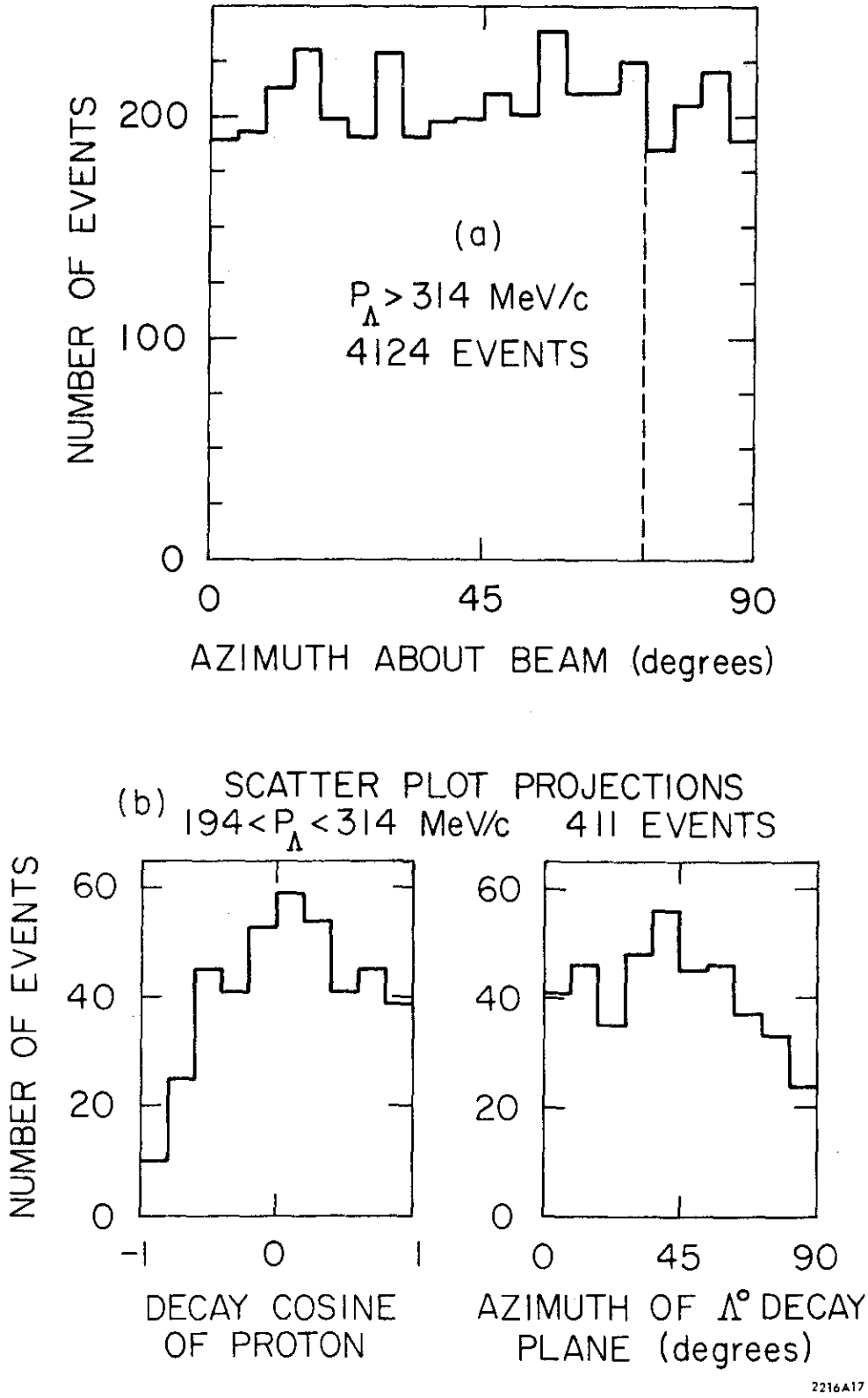

FIG. 11--Three "isotropic" distributions sensitive to steeply dipping or low momentum lambdas. Upper figure shows isotropy about the incident beam for $P_\Lambda > 314$ MeV/c ($-t > 0.05$ GeV^2 for $\overline{K}^0 p \rightarrow \pi^+ \Lambda$). Lower figures are the projections of a scatter plot of decay cosine of proton versus azimuth of Λ decay plane. Losses in the two projections are highly correlated and care must be taken to avoid double counting of losses.

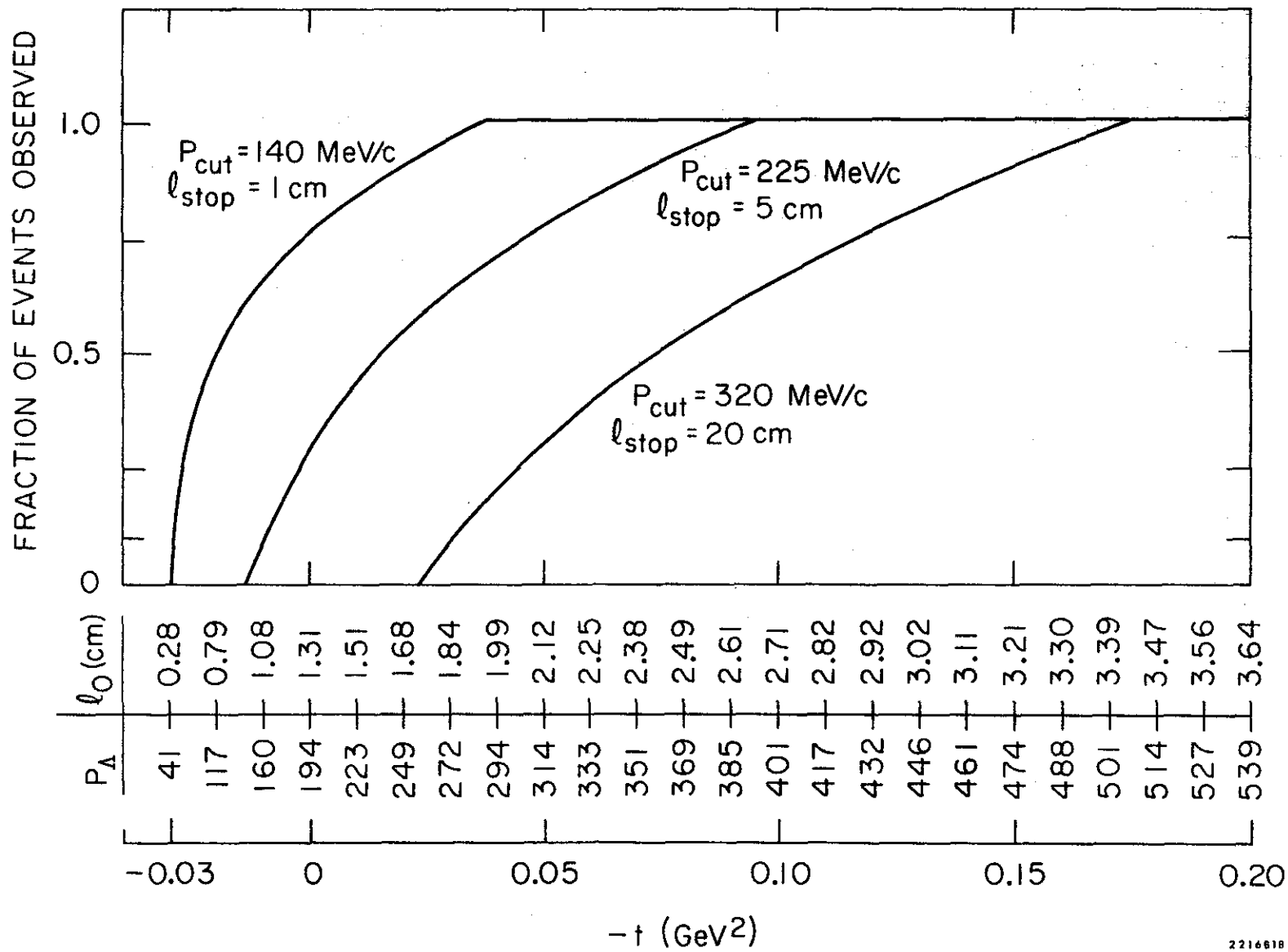

FIG. 12--Calculation of vee detection efficiency versus Λ momentum when proton tracks shorter than ℓ_{STOP} are considered invisible. Corrections to the data however, came from the data and not from these simulations.

The first issue to be resolved is the selection of the fiducial volume. Based on studies of vertex distributions (Fig. 13) together with some limiting factors the regions shown in Fig. 14 were chosen for primary vertex (solid line) and secondary vertex (dotted line) fiducial volumes. The limiting factors on the fiducial volume size were considerations such as initial scanning volume, adequate vee track lengths for a good measurement, and uniform detection efficiency throughout the volume. Selecting then a sample of unambiguous ET 110 associated Λ events (i.e., no competing $K_S^o \rightarrow \pi^+\pi^-$ 3-C fit) one may proceed, knowing that for a lossless sample of N_o decaying particles one expects

$$dn(x) = N_o e^{-x/\ell_o} \frac{dx}{\ell_o}$$

events between x and x + dx, where $\ell_o = \beta\gamma c\tau_o = \frac{P_\Lambda}{m_\Lambda} c\tau_o$ and τ_o is the lambda proper lifetime. Hence weighting each event by the factor $\ell_o e^{+x/\ell_o}$ results in a flat distribution in x provided detection efficiency is independent of the vee length x. However, what is instead observed is the function E(x), which is a product of the actual efficiency e(x) and the factor $(1 - x/\ell_{HBC})$. This second factor takes into account the fact that the chamber is finite and that by necessity $E(x) \rightarrow 0$ as $x \rightarrow \ell_{HBC}$.†

The detection efficiency, e(x), has been extracted and is shown in Fig. 15. The overall efficiency scale was established by assuming 100% efficiency over a flat region of the curve. For the purpose of Fig. 15 the 100% efficiency

† Actually the effective chamber size, ℓ_{HBC} is a function of the kinematic variables s and t so that ℓ_{HBC} is computed, on an event by event basis, as the distance along the vee direction $\hat{v}$ from the primary vertex fiducial boundary in the $-\hat{v}$ direction to the secondary vertex fiducial boundary in the $+\hat{v}$ direction.

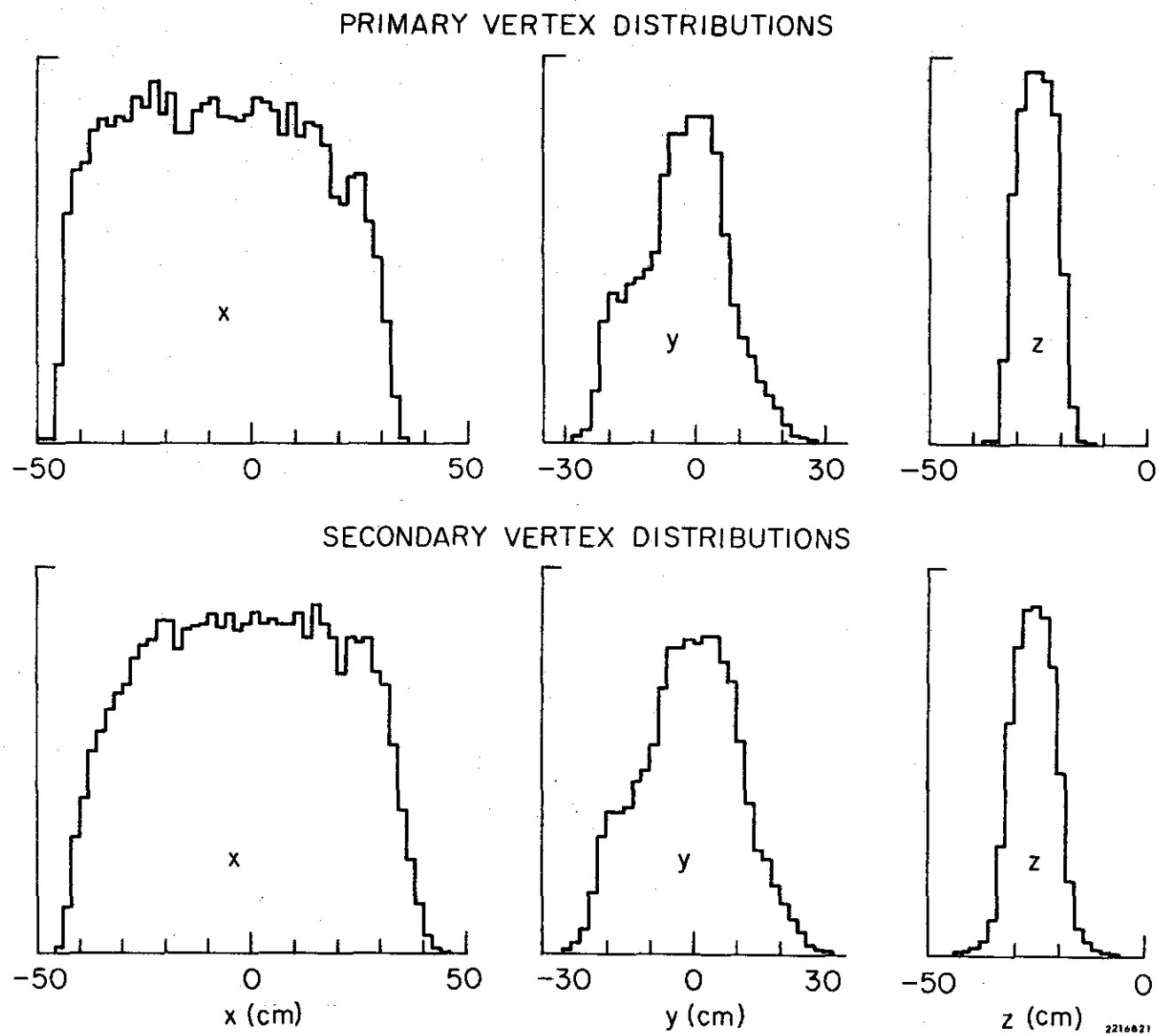

FIG. 13--Primary and secondary vertex distributions in the bubble chamber for $\pi^+(\Lambda, \Sigma^0)$ events. The beam travels in the + x direction.

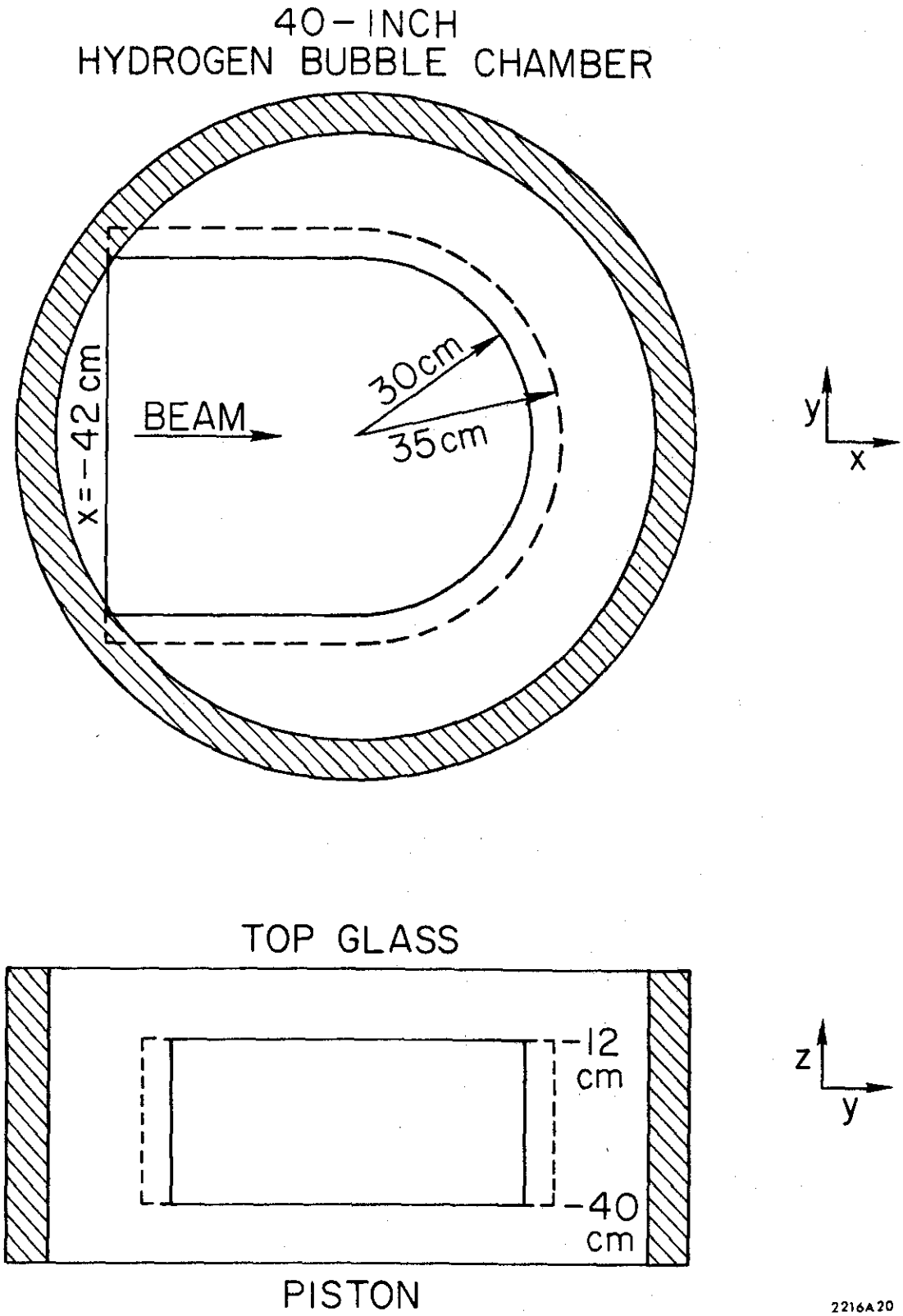

FIG. 14--Fiducial volume boundaries for primary (solid line) and secondary (dotted line) vertices.

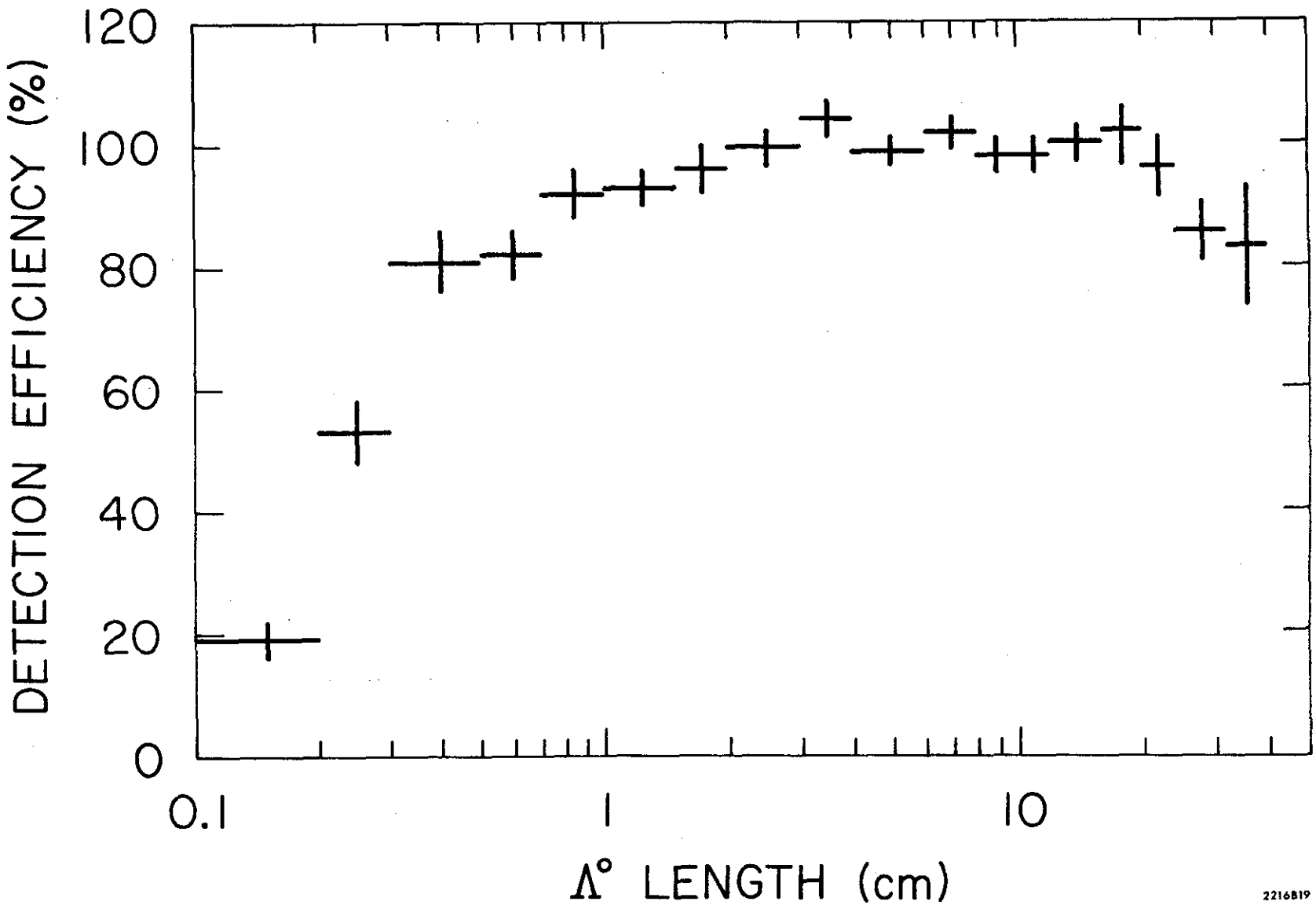

FIG. 15--Vee detection efficiency versus lambda length for all unambiguous ET 110 Λ events. The vertical scale was established by assuming 100% efficiency in the 2-11 cm region.

region was assumed to extend from 2 cm. to 11 cm.; however, had we chosen 2-5 cm instead we would have observed efficiencies of 99 ± 2% for the 5-10 cm region, 99 ± 3% for 10-18 cm, and 86 ± 3% for 18-30 cm. On the basis of the efficiency profile a maximum vee length cutoff of 30 cm has been chosen with vee lengths between 16 cm and 30 cm being corrected by the reciprocal of the EFF factor given in Table 3b. Actually the fitted efficiency factor drops below unity only above 18.7 cm so that vee lengths between 16 cm and 18.7 cm are given unit weight.

Though the efficiency correction for long length vees proved to be independent of momentum, corrections for short length vees showed a strong momentum dependence, the strength of which increased as x decreased. The momentum dependent efficiency factors for short length vees were obtained from two parameter fits and are given in Table 3b. On the basis of these fits minimum length cuts of 0.3 cm for vees with $P_\Lambda < 2$ GeV/c and 0.5 cm for vees with $P_\Lambda > 2$ GeV/c have been selected. Again, the guideline on selecting these cuts has been maximizing statistics consistent with avoiding events with anomalously high weights which act to deteriorate the effective statistics.

With known detection efficiencies and minimum and maximum vee lengths (LMIN and LMAX respectively) chosen, the weight for an event is given by the reciprocal of the detection probability W, where

$$W = EFF * (e^{-X_1/\ell_o} - e^{-X_2/\ell_o})$$

and where

X_1 = LMIN

X_2 = the smaller of (LMAX, S) where S is the distance from the primary vertex to the secondary vertex fiducial boundary as measured along the lambda's flight path.

TABLE 3

EFFICIENCIES FOR Λ DETECTION

(a) Azimuthal and Slow Proton Losses

P_Λ (MeV/c)	$-t$ (GeV^2) for $\bar{K}^o p \rightarrow \pi^+ \Lambda^o$	Efficiency (%)
< 195	< 0	46 ± 6
195 - 400	0.0 - 0.1	81 ± 3
> 400	> 0.1	93 ± 1

(b) Scanning Efficiency Versus Λ Decay Length

Decay Length ℓ_Λ (cm)	Normalized Scanning Efficiency
0.2 - 0.3	0.68 - 0.19 P_Λ(GeV/c)
0.3 - 0.5	0.91 - 0.138 P_Λ
0.5 - 1.0	0.93 - 0.039 P_Λ
1.0 - 2.0	0.95 - 0.019 P_Λ
2.0 - 18.7	≡ 1.00
18.7 - 30.0	1 - .0187 (ℓ_Λ - 18.7)

TABLE 3 (cont'd)

(c) Other Correction Factors

1 prong-V improperly scanned as K_L^o beam decays	1.05
1 prong-V/Beam Decay relative scanning-processing eff.	(No correction)*
Unobserved Λ decay modes	1.56
Confidence level cut at 1%	1.01
Σ^o Mass cut	1.05
Loss of Σ^o data from residual Λ, Σ^o ambiguities	1.03
Contamination of Σ^o data from Λ channels	(> 0.98)*
Contamination of Λ data by Σ^o events	(> 0.99)*

*Corrections in parentheses have been neglected.

In addition, the large sample of unambiguous 3-C Λ fits in the uniform detection efficiency region of e(x) have enabled us to obtain a new measurement of the Λ lifetime of 2.54 ± 0.05 ($\times 10^{-10}$ seconds), which is in agreement with the present world average of 2.52 ± 0.02 ($\times 10^{-10}$ seconds).[28]

B. Λ and Σ^0 Signal Quality

In this experiment we are fortunate in that the Λ and Σ^0 signals are quite free of contamination from one another and from other backgrounds. These resolution capabilities are due in large part to the very well known incident $\overline{K}^0$ direction. However, more complete separation of the Λ and Σ^0 signals and evaluation of their contamination levels proved to be necessary for accurate cross section determination.

1. Λ, Σ^0 Separation

Nearly 80 percent of the events with a good 6-C $\Lambda\pi^+$ fit also had an accompanying 4-C $\Sigma^0\pi^+$ fit. Although this may seem discouraging at first, a brief glance at the "$\Lambda\gamma$" invariant mass plots in Fig. 16 assures one that most of the ambiguities indeed belong to the higher constraint $\Lambda\pi^+$ reaction as naively expected from the frequent assumption that the highest constraint fit achieved is generally the correct one. However, above the 3 GeV/c there is a clear presence of a signal near the Σ^0 mass of 1192 MeV. A mass cut on the data might appear appropriate but fortunately some well known decay properties of the Σ^0 permit a more elegant separation.

In the electromagnetic decay of the Σ^0 into $\Lambda\gamma$,† the gamma ray is emitted isotropically in the rest frame of the Σ^0, while for true Λ events a false gamma

† The lifetime for this decay ($\tau < 1.0 \times 10^{-14}$ sec) is such that the decay occurs within a few microns of the primary vertex and is therefore assumed to occur at the primary vertex location.

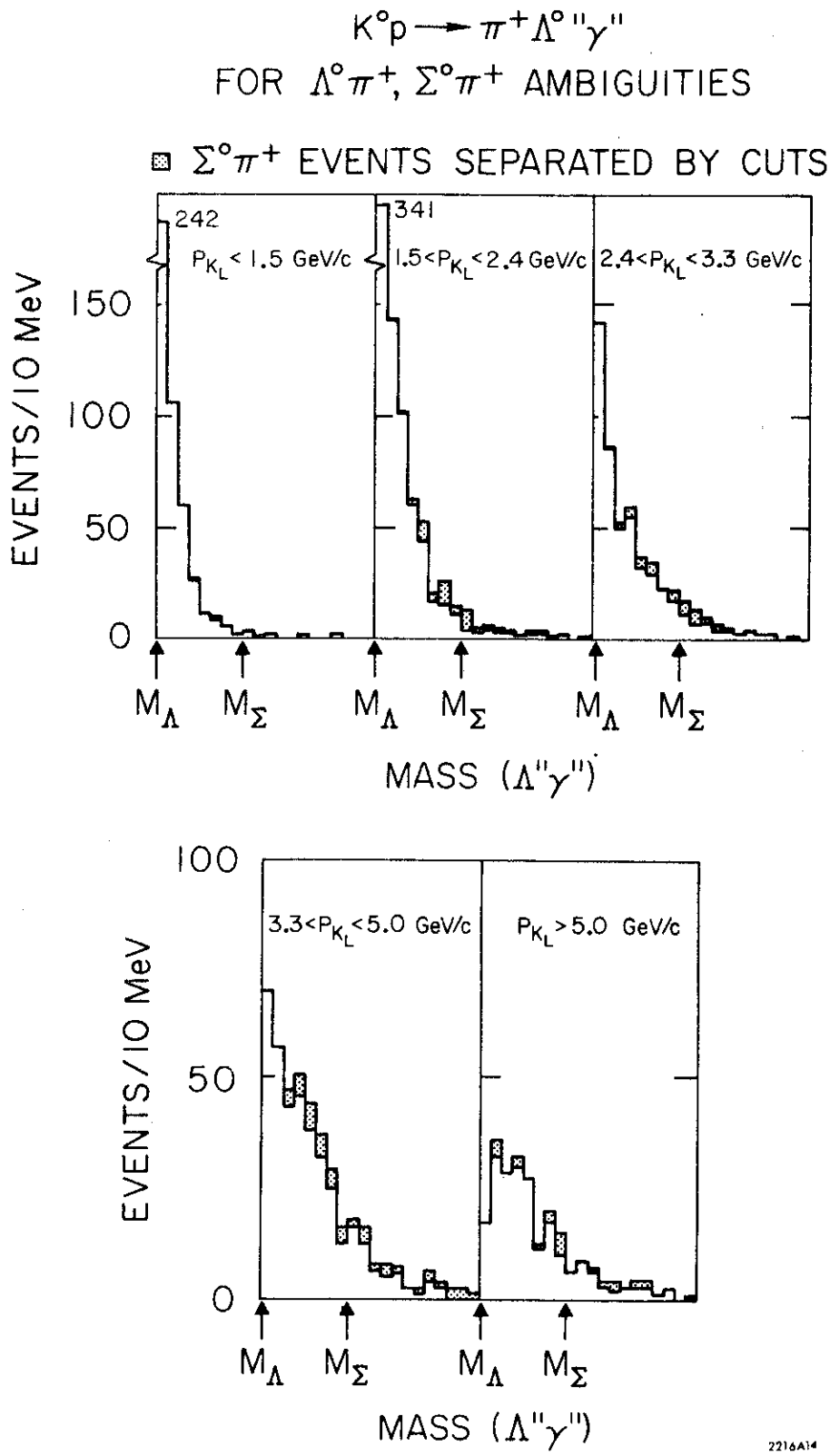

FIG. 16--Invariant mass of the $\Lambda\gamma$ system for Λ, Σ^0 ambiguities.

will tend to appear where measurement errors are most likely to tolerate it. From the point of view of a false Σ^0 the easiest place to insert the 74 MeV/c gamma momentum is along the direction of the incident beam or at least coplanar with the production plane since momentum errors along the normal to the overall production plane, n, should be minimal. As can be seen from the distributions of these ambiguous events (Fig. 17) with respect to $(\hat{\gamma}\cdot\hat{\bar{K}}^0)_{\Sigma^0 r.f.}$ and $(\hat{\gamma}\cdot\hat{n})_{\Sigma^0 r.f.}$ most of the events are probably fake Σ^0 events and hence real $\Lambda\pi^+$ events. Events for which (a) $|\hat{\gamma}\cdot\hat{n}| > 0.4$ or (b) $(\hat{\gamma}\cdot\hat{\bar{K}}^0) < 0.4$ or (c) $|\hat{\gamma}\cdot\hat{n}| > 0.1$ and $(\hat{\gamma}\cdot\hat{\bar{K}}^0) < 0.9$ are assumed to be Σ^0 events. The events obtained from these three cuts constitute an $\sim 12\%$ addition to the unambiguous $\Sigma^0\pi^+$ events and are seen as the shaded contribution to Fig. 18, which depicts the $\hat{\gamma}\cdot\hat{\bar{K}}^0$ and $\hat{\gamma}\cdot\hat{n}$ distributions for all $\Sigma^0\pi^+$ fits. Inclusion of the events from the cuts clearly improves the uniformity of the $\hat{\gamma}\cdot\hat{\bar{K}}^0$ distribution; however, some genuine Σ^0 events with $(\hat{\gamma}\cdot\hat{\bar{K}}^0) \approx +1$ and $(\hat{\gamma}\cdot\hat{n}) \approx 0$ will also have $\Lambda\pi^+$ fits and, being unrecoverable by cuts, are compensated for by a correction factor of 1.03. Conversely, a slight residual $\Sigma^0\pi^+$ contamination to the $\Lambda\pi^+$ sample persists and is estimated at $< 2\%$. No attempt has been made to correct the $\Lambda\pi^+$ data for this residual contamination level.

2. Σ^0 Purity

Aside from the loss of good Σ^0 events to the Λ category, the only other potential threat to the purity of the Σ^0 sample comes from the possible influx of "$\Lambda\pi^+$ neutrals" events. To investigate this possibility all events having a good 3-C $\Lambda\to p\pi^-$ vee fit were tried with the hypothesis $\Lambda\pi^+$ "γ".† The resulting Λ"γ" mass

† The gamma ray is indicated by quotes as it is meant to stand for all missing neutrals. Since the fit with a gamma is 0-C at the main vertex almost all events will obtain a fit. Two 0-C solutions often resulted, in which case the one with the lower $\Lambda\gamma$ mass was used. Use of an actual γ merely facilitated investigation of the Σ^0 purity.

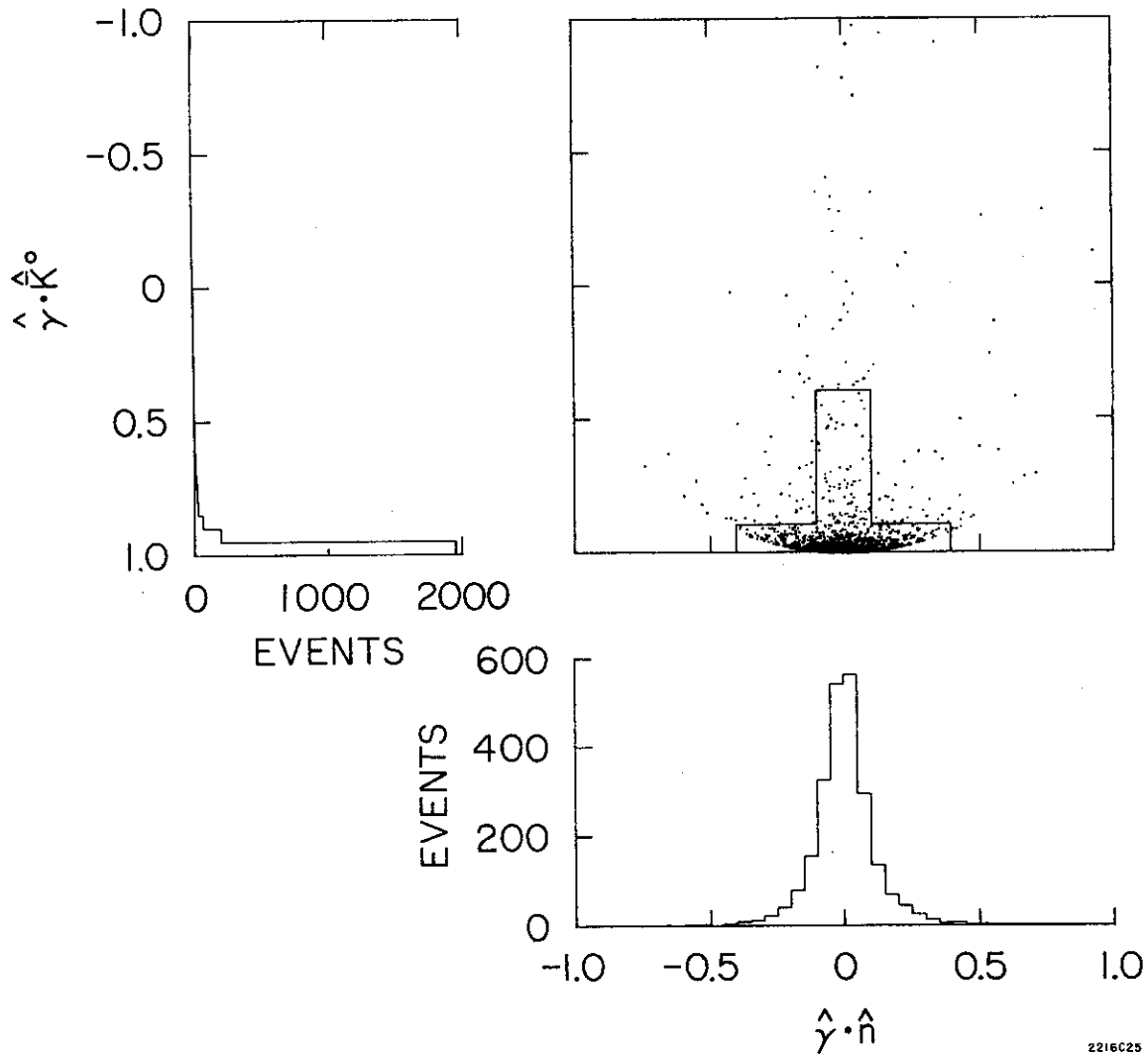

FIG. 17--Distribution of Λ, Σ^{o} ambiguities with respect to $(\hat{\gamma}\cdot\hat{\bar{K}}^{o})$ and $(\hat{\gamma}\cdot\hat{n})$ in the Σ^{o} rest frame. Events outside the "double rectangle" are assumed to be Σ^{o} events.

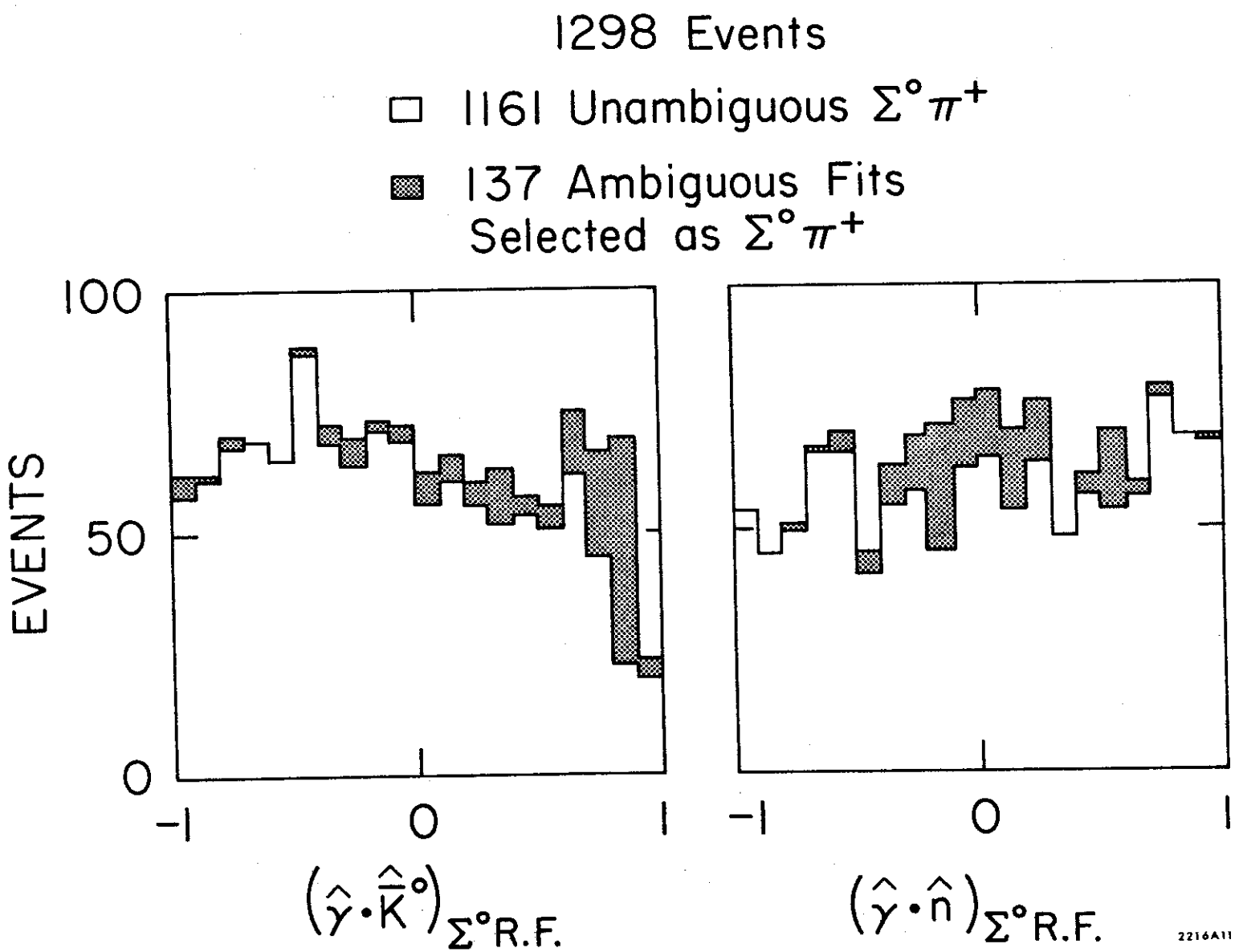

FIG. 18--$(\hat{\gamma}\cdot\hat{\bar{K}}^0)$ and $(\hat{\gamma}\cdot\hat{n})$ distributions for accepted Σ^0 events.

distributions, with good $\Lambda\pi^+$ events excluded, are shown in Fig. 19 for several beam momentum intervals and they indicate a relatively clean separation of the Σ^0 from the high mass continuum background. Although the Σ^0 broadens somewhat at higher beam momenta the available phase space for non-Σ^0 events conveniently dies away leaving the Σ^0 purity rather constant with respect to momentum. The $\Lambda^0\pi^+\pi^0$ channel appears to be the chief contaminator of the Σ^0, its effects seemingly more pronounced at large momentum transfers where low statistics inhibit a more detailed analysis. However, our mass resolution always remains good enough to insure against any $Y_1(1385) \rightarrow \Lambda\pi^0$ resonance contribution to the Σ^0 signal.

Selection of a high mass cutoff for the Σ^0 was accomplished by first assuming that the low mass side of the Σ^0 was uncontaminated and then noting how far one must go below the Σ^0 central mass value of 1192.5 MeV to include 90% of the events on the low side of the Σ^0. Determining this to be $\sim$32.5 MeV we choose a high mass cutoff of 1192.5 + 32.5 = 1225.0 MeV and proceed to count up the number of events in this upper 32.5 MeV mass slice. Assuming that the Σ^0 must be symmetric about its central value, the number of excess events on the high mass side permits calculation of the contamination level, which turns out to be 2.5 ± 2.8% or less than 6.1% contamination at the 90% confidence level. As the level of contamination is consistent with zero, no correction has been made. To compensate for the 5% loss in real data resulting from the mass cut, $\Sigma^0\pi^+$ cross sections have been increased by 5%.

C. Cross Sections Versus Beam Momentum

1. Procedure

The absolute normalization for both the total and differential cross sections for the processes $\overline{K}^0p \rightarrow \Lambda\pi^+$ and $\overline{K}^0p \rightarrow \Sigma^0\pi^+$ hinges on a single quantity which

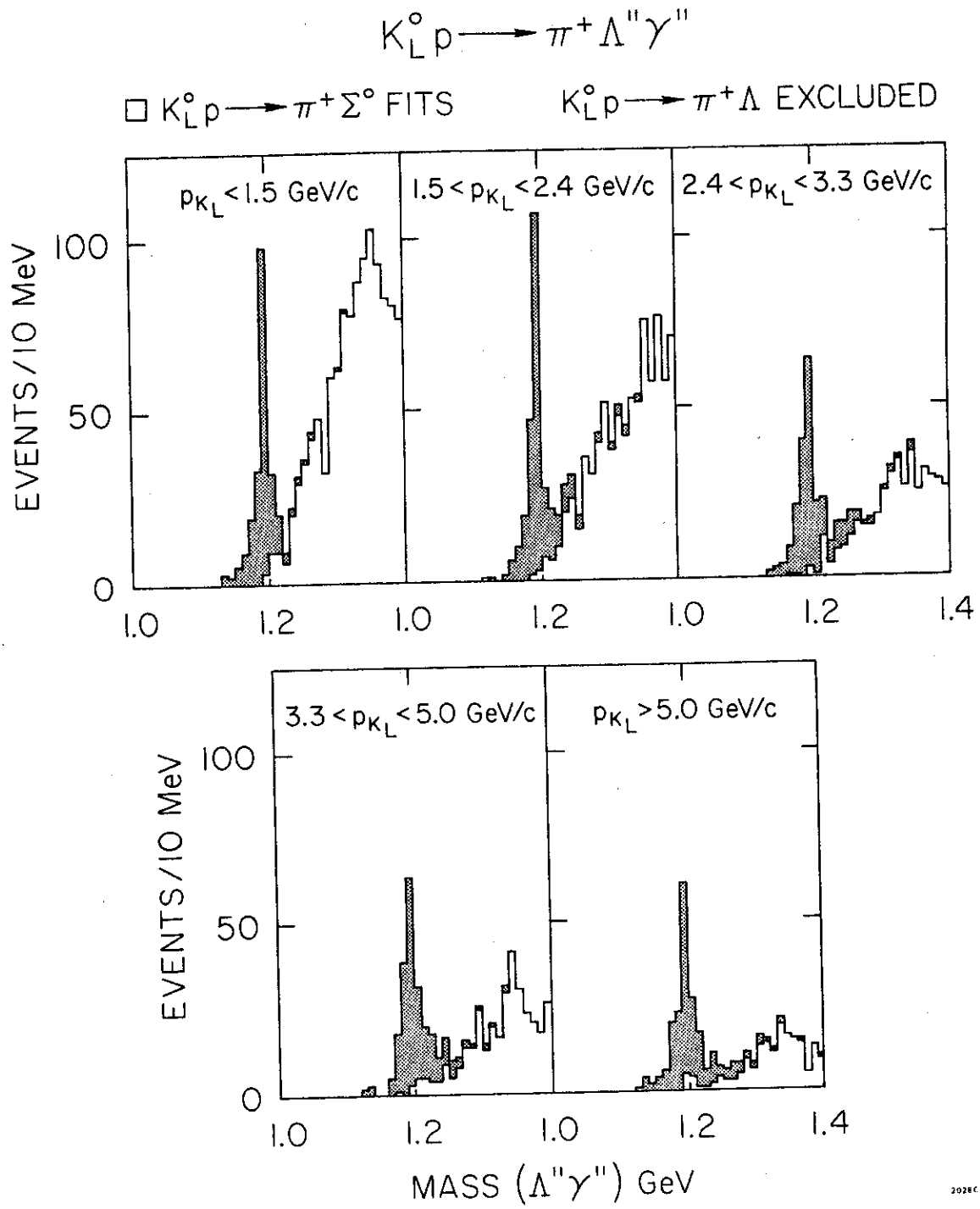

FIG. 19--Invariant mass of the $\Lambda\gamma$ system; $\bar{K}^o p \rightarrow \pi^+ \Lambda$ events are excluded. The shaded events are in the channel $\bar{K}^o p \rightarrow \pi^+ \Sigma^o$.

is the momentum averaged total cross section $<\sigma>$ for the sum of these two reactions. This cross section can only be properly evaluated for the data from Run I (see Chaper 3 sections D and E) and is given in microbarns by the expression

$$<\sigma> = \frac{10^{30}}{N_o \rho \ell} \frac{\epsilon_s(200)}{\epsilon_s(110)} \frac{\epsilon_p(200)}{\epsilon_p(110)} \frac{R}{B.R.(\Lambda^o \rightarrow p\pi^-)} \frac{\Delta P_F}{\Delta P_N} \sum_{i=1}^{N_1} \frac{k_i}{\frac{1}{2}F(p_i)}$$

where $N_o = 6.022 \times 10^{23}$ atoms/gm H_2 (molecules/gmw H_2)

ρ = density of liquid hydrogen (taken as 0.0594 gm/cc)

ℓ = primary vertex fiducial length = 40 cm ($-30 < x < +10$ cm)

$\epsilon_s(ET)$ = scanning efficiency for Run I determined by second scan to be 0.92 for both 110 and ET 200

$\epsilon_p(ET)$ = Run I processing efficiency defined as the number of events passing TVGP/total number of events (including ~10% unmeasurable events) and computed to be 0.897 for both ET 110 and ET 200.

R = Run I resolve scan factor of 1.05 for ET 110 events improperly scanned as ET 200 events (main vertex missed) less the 2% scanning efficiency correlation (see Chapter 2 section G).

$B.R.(\Lambda^o \rightarrow p\pi^-)$ = branching ratio of $(\Lambda \rightarrow p\pi^-/\Lambda \rightarrow \text{all})$ = 0.642

ΔP_N = momentum interval over which cross section averaging is done = 4 GeV/c (i.e., averaging from 2 GeV/c to 6 GeV/c)

N_1 = number of $\Lambda\pi^+ + \Sigma^o\pi^+$ events from Run I in the momentum interval ΔP_N.

k_i = event weight exclusive of spectrum weighting. This factor includes corrections for Λ decay losses (due to azimuth and decay helicity cosine), vee detection efficiency versus length, finite chamber loss of vees, confidence level cut (> 1%), and high mass cut and ambiguity loss on Σ^0 data. (See Table 3 for summary of all corrections.)

$\frac{1}{2}F(p_i)$ = number of $\overline{K}^0$ particles for Run I in a beam momentum slice of width ΔP_F centered at the beam momentum p_i of the ith event. (N.B. $\overline{K}^0$ flux = $\frac{1}{2}$ K_L^0 flux.)

Once a value of $<\sigma>$ is established using only Run I and a very select fiducial volume region (-30 < x < + 10 cm), the overall composite spectrum together with all events from the full fiducial volume are used to compute an average unnormalized cross section $<W>$ averaged over the same momentum region, where

$$<W> = \sum_{i=1}^{N_T} \frac{k_i}{F(p_i)}$$

and where N_T = total number of $\Lambda\pi^+ + \Sigma^0\pi^+$ events in the momentum interval ΔP_N. The total cross section $\sigma(p)$ for a reaction averaged over the momentum interval from $p - \frac{\Delta p}{2}$ to $p + \frac{\Delta p}{2}$ is then just

$$\sigma(p) = \frac{<\sigma>}{<W>} \frac{\Delta P_N}{\Delta p} \sum_{i=1}^{n(p)} \frac{k_i}{F(p_i)}$$

where n(p) = number of events in the momentum interval Δp centered at p and from the identical film sample as used in calculating $<W>$.

If one now considers the quantity $X = \sum_{i=1}^{n} w_i$, where w_i is the total event weight $k_i/F(p_i)$, we see that the statistical error is just $\delta X = [\sum_{i=1}^{n} w_i^2]^{1/2}$. These

statistical errors $\delta X/X$ are then taken in quadrature with the composite shape uncertainty $\delta F(p)/F(p)$ to provide the quoted errors in the cross sections. However, there are additional errors due to the statistical uncertainty in $\langle\sigma\rangle$ ($\sim 6\%$), the overall uncertainty in the Run I flux ($\sim 10\%$), and uncertainties in event weights and various efficiency corrections ($< 10\%$), which combined in quadrature give an additional $\sim 15\%$ uncertainty to the overall cross section normalization. Beam momentum uncertainty in the final event samples was about 2%.

2. Results

The value of $\langle\sigma\rangle$ averaged from 2.0 GeV/c to 6.0 GeV/c was found to be 444 ± 26 ub and was extracted from a sample of 305 events which after dispersion compensation gave a statistical uncertainty equivalent to ~ 287 unweighted events.

Cross sections as a function of incident $\overline{K}^0$ beam momentum are given in Table 4 for the reactions $\overline{K}^0 p \rightarrow \Lambda\pi^+$ and $\overline{K}^0 p \rightarrow \Sigma^0\pi^+$. As mentioned previously the errors on these data include only statistical and spectral shape uncertainties and do not reflect the additional $\sim 15\%$ uncertainty in overall normalization. The cross sections are also displayed in Figs. 20 and 21 along with representative data from other experiments.[30-32] The $\overline{K}^0 p \rightarrow \Lambda\pi^+$ data are compared directly to data on $K^- n \rightarrow \Lambda\pi^-$ since both reactions have pure isospin (I=1) initial and final states while cross sections for $K^- p \rightarrow \Lambda\pi^0$ must be multiplied by two for direct comparison since the $K^- p$ initial state is equally divided into I=0 and I=1 components and only the I=1 component projects into the final state. In Fig. 21 the $\overline{K}^0 p \rightarrow \Sigma^0\pi^+$ data are to be compared directly with the data for $K^- n \rightarrow \Sigma^0\pi^-$; however, comparison to $K^- p \rightarrow \Sigma^+\pi^-$ data is not straightforward. From isospin considerations the amplitudes for the three processes may be written[31b] as

TABLE 4

Total Cross Sections

p_{BEAM} (GeV/c)	Observed No. of Events	$\sigma(\overline{K}^o p \rightarrow \Lambda\pi^+)$ mb.	p_{BEAM} (GeV/c)	Observed No. of Events	$\sigma(\overline{K}^o p \rightarrow \Sigma^o\pi^+)$ mb.
0.6 - 0.8	52	4.51 ± 0.69	0.6 - 0.8	26	2.32 ± 0.49
0.8 - 1.0	105	4.68 ± 0.52	0.8 - 1.0	41	1.86 ± 0.30
1.0 - 1.2	146	3.77 ± 0.34	1.0 - 1.2	44	1.16 ± 0.18
1.2 - 1.4	154	2.58 ± 0.22	1.2 - 1.4	43	777 ± 123 μb
1.4 - 1.6	186	2.36 ± 0.18	1.4 - 1.8	113	661 ± 65
1.6 - 1.8	185	1.85 ± 0.14	1.8 - 2.2	102	413 ± 43
1.8 - 2.0	157	1.28 ± 0.11	2.2 - 2.6	91	264 ± 28
2.0 - 2.2	143	959 ± 84 μb	2.6 - 3.0	98	250 ± 27
2.2 - 2.4	139	776 ± 68	3.0 - 3.5	98	154 ± 16
2.4 - 2.6	143	724 ± 63	3.5 - 4.0	80	123 ± 15
2.6 - 2.8	123	570 ± 53	4.0 - 4.5	75	109 ± 13
2.8 - 3.0	98	440 ± 46	4.5 - 5.0	50	75 ± 11
3.0 - 3.2	87	338 ± 38	5.0 - 6.0	84	65 ± 7
3.2 - 3.4	80	292 ± 34	6.0 - 7.0	52	50 ± 7
3.4 - 3.8	135	236 ± 21	7.0 - 8.0	34	41 ± 7
3.8 - 4.2	123	216 ± 21	8.0 - 10.0	29	30 ± 6
4.2 - 4.6	83	141 ± 16	10.0 - 12.0	5	13 ± 7
4.6 - 5.0	63	104 ± 14			
5.0 - 5.5	83	123 ± 14			
5.5 - 6.0	64	95 ± 12			
6.0 - 7.0	77	68 ± 8			
7.0 - 8.0	41	47 ± 8			
8.0 - 10.0	35	30 ± 5			
10.0 - 12.0	10	26 ± 9			

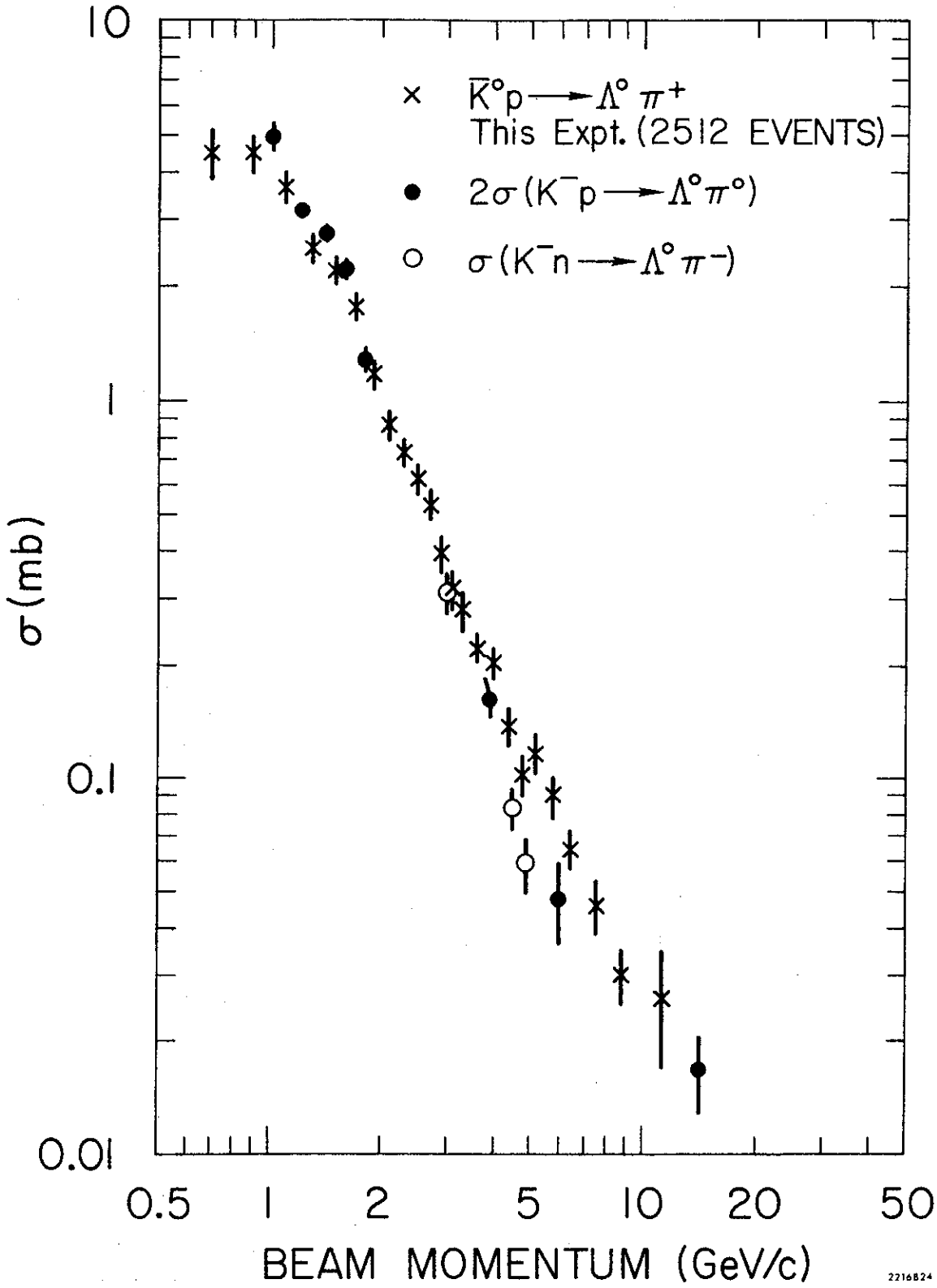

FIG. 20--Cross sections versus incident momentum for $\overline{K}^{o}p \rightarrow \pi^{+}\Lambda$. Other data are from refs. 30 and 31.

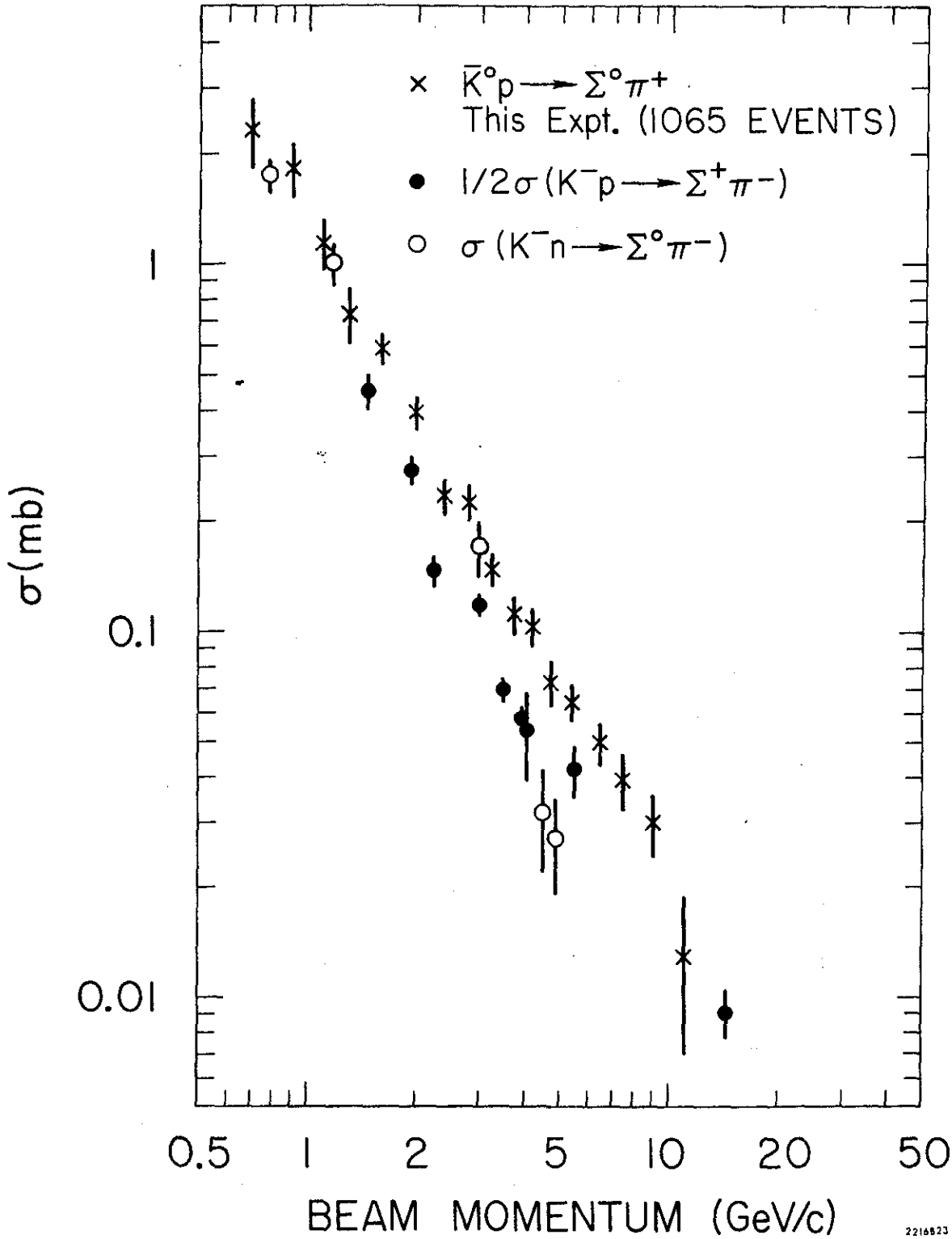

FIG. 21--Cross sections versus incident momentum for $\bar{K}^0 p \rightarrow \pi^+ \Sigma^0$. Other data are from refs. 30 and 32.

$$A(\overline{K}^0 p \to \pi^+\Sigma^0) = A(K^- n \to \Sigma^0\pi^-) = \frac{1}{\sqrt{2}} [A(K^- p \to \Sigma^+\pi^-) - A(K^- p \to \Sigma^-\pi^+)].$$

If t channel exchanges with isospin 3/2 could be neglected then $A(K^- p \to \Sigma^-\pi^+)$ would vanish and the natural comparison would be to $\frac{1}{2}\sigma(K^- p \to \Sigma^+\pi^-)$ as given; however, data on $K^- p$ induced reactions[33] indicate that the quantity $|R| = [\sigma(K^- p \to \Sigma^-\pi^+)/\sigma(K^- p \to \Sigma^+\pi^-)]^{\frac{1}{2}}$ is about $\frac{1}{2}$ at 2 GeV/c, falling to $\sim\frac{1}{4}$ near 5 GeV/c. Hence, though no simple comparison is adequate, observing in Fig. 21 that $\frac{1}{2}\sigma(K^- p \to \Sigma^+\pi^-)$ is consistently only about two-thirds of $\sigma(\overline{K}^0 p \to \Sigma^0\pi^+)$, a value of $R \equiv A(K^- p \to \Sigma^-\pi^+)/A(K^- p \to \Sigma^+\pi^-) \sim -0.2$ is suggested, in agreement with the range of $|R|$ obtained from $K^- p$ data.

The data for both the $\pi^+\Lambda$ and $\pi^+\Sigma^0$ cross sections have been fit to the power law $\sigma = AP^n_{BEAM}$, and the result given in Table 5 along with the A and n coefficients for some related processes.[33-34] One observes the $\overline{K}$ induced cross sections to be considerably larger but falling more rapidly than their companion line reversed π cross sections over the momentum intervals considered.

The low energy data are replotted in Fig. 22, where $\sigma/4\pi\lambda\!\!\!^{-}_i\lambda\!\!\!^{-}_f$ is displayed as a function of center of mass energy.† These data as well as the cross sections, σ, are recorded in Table 6. In the case of $\overline{K}^0 p \to \pi^+\Lambda$, the interval $1.8 \leq P_{BEAM} \leq 5.0$ GeV/c includes the $\Sigma(2250)$ and $\Sigma(2455)$ enhancements as well as possible structure near 3 GeV. It is therefore not surprising to find a steeper P_{BEAM} dependence ($n = -2.62 \pm 0.10$) in this region than is usually associated with strange meson exchange.[35] However, in the higher

† $\lambda\!\!\!^{-}_i$ and $\lambda\!\!\!^{-}_f$ are the wavelengths in the initial and final states respectively, where $\lambda\!\!\!^{-}_i \equiv \hbar/p$.

TABLE 5

Fits to $\sigma = A P_{BEAM}^{n}$

Reaction	P_{BEAM} Interval (GeV/c)	A(mb)	n	Reference
$\overline{K}^{o}p \rightarrow \Lambda\pi^{+}$	1.8 - 12.0	5.9 ± 0.5	-2.44 ± 0.07	This Exp.
	1.8 - 5.0	7.0 ± 0.8	-2.62 ± 0.10	" "
	5.0 - 12.0	4.3 ± 0.3	-2.21 ± 0.19	" "
$K^{-}p \rightarrow \Lambda\pi^{o}$	1.5 - 6.0	5.20 ± 0.28	-3.30 ± 0.10	Ref. 33
$\pi^{-}p \rightarrow \Lambda K^{o}$	2.0 - 6.0	0.79 ± 0.14	-1.93 ± 0.17	Ref. 34
$\overline{K}^{o}p \rightarrow \Sigma^{o}\pi^{+}$	1.8 - 12.0	1.3 ± 0.2	-1.78 ± 0.09	This Exp.
	1.8 - 5.0	1.4 ± 0.2	-1.85 ± 0.15	" "
	5.0 - 12.0	1.3 ± 0.7	-1.74 ± 0.31	" "
$K^{-}p \rightarrow \Sigma^{+}\pi^{-}$	1.0 - 5.5	1.86 ± 0.04	-2.00 ± 0.07	Ref. 33
$\pi^{-}p \rightarrow \Sigma^{o}K^{o}$	2.0 - 6.0	0.46 ± 0.13	-1.82 ± 0.28	Ref. 34

TABLE 6

Cross Sections for $\overline{K}^0 p \cdot \Lambda\pi^+$ and $\overline{K}^0 p \quad \Sigma^0\pi^+$ in the Resonance Region

$E_{c.m.}$ (GeV/c)	$\overline{K}^0 p \to \Lambda\pi^+$		$\overline{K}^0 p \to \Sigma^0\pi^+$	
	$\sigma(\mu b)$	$\sigma/4\pi\lambda\!\!\!^{-}_i\lambda\!\!\!^{-}_f$ (X 10^{-3})	$\sigma(\mu b)$	$\sigma/4\pi\lambda\!\!\!^{-}_i\lambda\!\!\!^{-}_f$ (X 10^{-3})
1.60 - 1.70	4229 ± 647	147 ± 22	2131 ± 454	67.2 ± 14.2
1.70 - 1.80	4844 ± 506	245 ± 25	1804 ± 287	80.0 ± 12.6
1.80 - 1.85	3581 ± 453	221 ± 28	1211 ± 256	68.2 ± 14.4
1.85 - 1.875	3819 ± 567	263 ± 39	1172 ± 328	74.0 ± 20.7
1,875 - 1.90	2438 ± 458	179 ± 33	680 ± 242	45.5 ± 16.2
1.90 - 1.925	2974 ± 463	231 ± 36	1115 ± 308	80.2 ± 22.1
1.925 - 1.95	2450 ± 388	202 ± 32	604 ± 192	46.8 ± 14.9
1.95 - 1.975	2786 ± 389	243 ± 34	925 ± 226	74.8 ± 18.3
1.975 - 2.00	2219 ± 338	204 ± 31	447 ± 162	38.6 ± 14.0
2.00 - 2.025	2290 ± 323	221 ± 31	489 ± 156	44.2 ± 14.1
2.025 - 2.05	2507 ± 343	255 ± 35	715 ± 181	67.8 ± 17.2
2.05 - 2.075	2289 ± 326	244 ± 35	771 ± 178	77.2 ± 17.8
2.075 - 2.10	1964 ± 265	220 ± 30	620 ± 156	64.9 ± 16.4
2.10 - 2.125	2039 ± 265	238 ± 31	853 ± 183	94.0 ± 20.2
2.125 - 2.15	1381 ± 237	168 ± 29	652 ± 148	75.3 ± 17.1
2.15 - 2.175	1340 ± 205	170 ± 26	567 ± 148	68.4 ± 17.9
2.175 - 2.20	1347 ± 199	178 ± 26	337 ± 102	42.4 ± 12.9
2.20 - 2.225	1294 ± 191	178 ± 26	561 ± 124	73.7 ± 16.3
2.225 - 2.25	984 ± 150	141 ± 22	374 ± 104	50.8 ± 14.1
2.25 - 2.275	1120 ± 171	167 ± 26	425 ± 98	60.2 ± 13.9
2.275 - 2.30	868 ± 134	134 ± 21	290 ± 81	42.5 ± 11.9
2.30 - 2.325	752 ± 122	120 ± 20	302 ± 78	46.1 ± 12.0
2.325 - 2.35	807 ± 123	134 ± 20	341 ± 83	53.7 ± 13.1
2.35 - 2.40	772 ± 83	135 ± 15	250 ± 48	42.1 ± 8.0
2.40 - 2.45	799 ± 80	149 ± 15	252 ± 47	45.1 ± 8.3
2.45 - 2.50	522 ± 63	104 ± 13	247 ± 50	47.3 ± 9.6
2.50 - 2.60	521 ± 43	113 ± 9	250 ± 31	52.4 ± 6.4
2.60 - 2.70	334 ± 32	81.3 ± 7.8	171 ± 23	40.0 ± 5.3
2.70 - 2.80	256 ± 26	69.1 ± 7.0	136 ± 19	35.6 ± 5.1
2.80 - 2.90	235 ± 24	70.1 ± 7.1	130 ± 19	38.1 ± 5.6
2.90 - 3.00	221 ± 23	72.7 ± 7.6	134 ± 18	42.8 ± 5.9
3.00 - 3.20	137 ± 13	50.9 ± 4.8	87.7 ± 10.3	32.1 ± 3.8
3.20 - 3.40	113 ± 11	49.3 ± 5.0	78.0 ± 9.6	33.5 ± 4.1
3.40 - 3.60	97.2 ± 10.5	49.4 ± 5.4	51.3 ± 7.8	25.7 ± 3.9

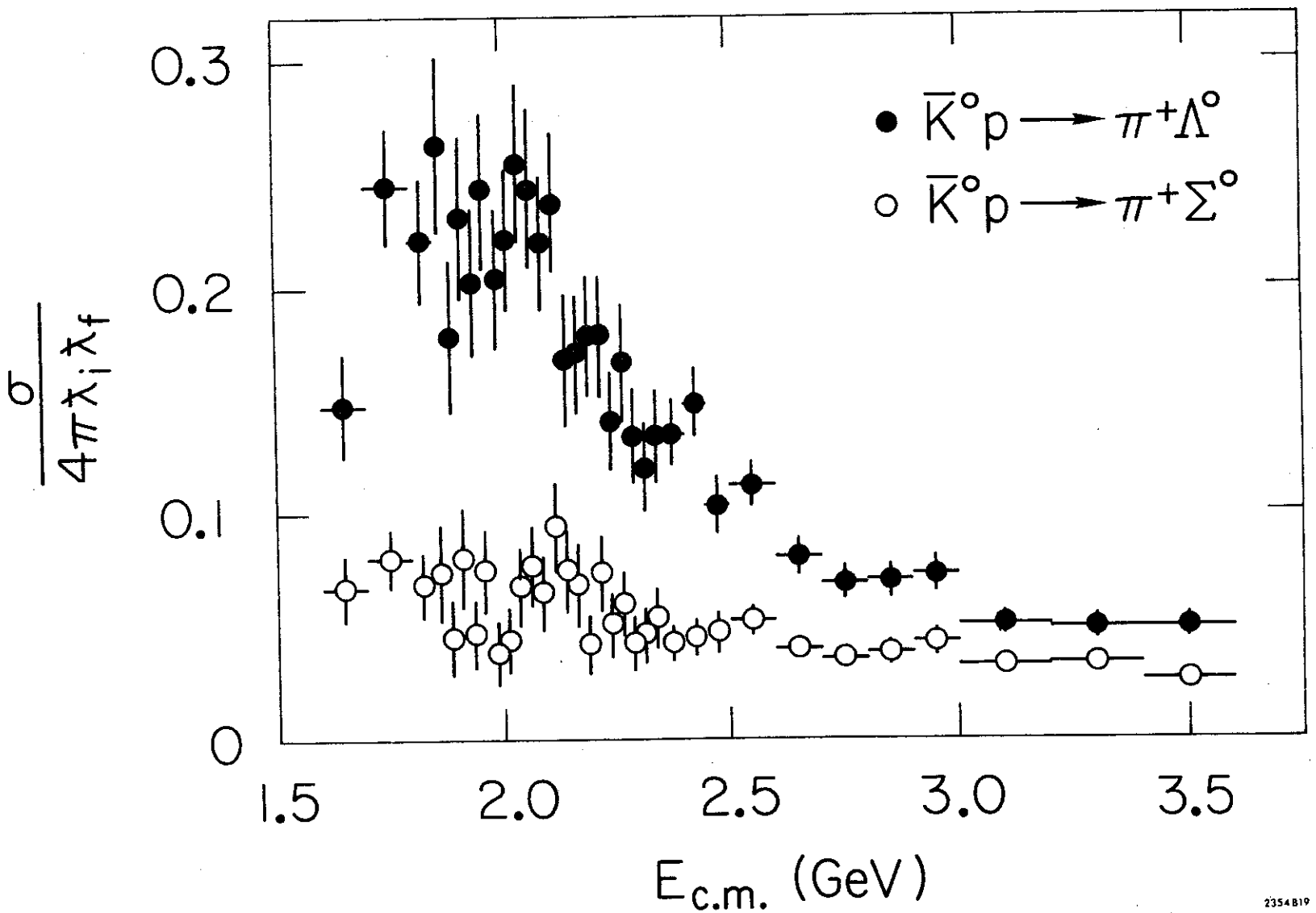

FIG. 22--$\sigma/4\pi\lambda_i\lambda_f$ versus center of mass energy for $\bar{K}^o p \rightarrow \pi^+\Lambda^o$ (solid points) and $\bar{K}^o p \rightarrow \pi^+\Sigma^o$ (open points).

momentum interval $5 \leq P_{BEAM} \leq 12$ GeV/c, where meson exchange might be expected to dominate, we find no significant difference, $n_\Sigma - n_\Lambda = 0.47 \pm 0.36$, in the momentum dependences of the $\pi^+\Lambda$ and $\pi^+\Sigma^0$ cross sections.

3. $\sigma_{\Sigma\pi}/\sigma_{\Lambda\pi}$ Versus Beam Momentum

Although the behavior of the ratio $\sigma(\overline{K}^0 p \rightarrow \Sigma^0\pi^+)/\sigma(\overline{K}^0 p \rightarrow \Lambda\pi^+)$ could be inferred from Figs. 20 and 21, it is of interest in its own right and is therefor tabulated in Table 7 and plotted in Fig. 23. This cross section ratio is insensitive to overall normalization uncertainty as well as errors in the special shape and hence, the quoted errors reflect only statistical uncertainty.† Above 1 GeV/c we see a steady rise of the ratio from ~ 0.3 at 1 GeV/c to ~ 0.6 near 6 GeV/c followed by a possible levelling off of the ratio to an asymptotic value of ~ 0.80 in the 6-12 GeV/c region. We note that the ratio of 0.79 ± 0.10 in the 6-12 GeV/c region compares favorably with the ratios 0.79 ± 0.02, 0.76 ± 0.02 and 0.75 ± 0.11 of Foley et al[36e] obtained at 8, 10.7, and 15.7 GeV/c respectively for the line reversed reactions $\pi^- p \rightarrow K^0(\Lambda, \Sigma^0)$.

The rapid rise in $\sigma(\pi^+\Sigma^0)/\sigma(\pi^+\Lambda)$ over the 1-6 GeV/c beam momentum interval is apparently the result of two effects. First, in the region $1.5 < P_{BEAM} < 3.0$ GeV/c the $\pi^+\Lambda$ channel appears to couple more strongly to I=1 s-channel resonances than the $\pi^+\Sigma^0$ channel. Equivalently we observe that in the backward scattering region baryon exchange is considerably more

† A possible exception to the spectral shape insensensitivity occurs in the 0.5 - 1.0 GeV/c bin where spectral weights differ by a factor of 7 in the space of only 0.5 GeV/c. Coupled with this is the fact that $\Sigma(1620)$ P11 and $\Sigma(1664)$ D13, decaying predominantly into $\Sigma\pi$, appear at 630 MeV/c and 730 MeV/c while the $\Sigma(1765)$ D15, decaying much more strongly into $\Lambda\pi$, appears at 940 MeV/c near the high momentum edge of this first bin. Hence, interpretation of the first bin is somewhat dubious and the errors may be underestimated.

TABLE 7

$\sigma(\bar{K}^o p \rightarrow \Sigma^o \pi^+)/\sigma(\bar{K}^o p \rightarrow \Lambda \pi^+)$

P_{BEAM} (GeV/c)	$\sigma_{\Sigma\pi}/\sigma_{\Lambda\pi}$ All t	$\sigma_{\Sigma\pi}/\sigma_{\Lambda\pi}$ $0.05 \leq -t \leq 0.4$ GeV^2
0.5 - 1.0	0.59 ± 0.10	0.89 ± 0.24
1.0 - 1.5	0.29 ± 0.03	0.32 ± 0.06
1.5 - 2.0	0.36 ± 0.04	0.51 ± 0.10
2.0 - 2.5	0.35 ± 0.04	0.50 ± 0.09
2.5 - 3.0	0.46 ± 0.05	0.49 ± 0.09
3.0 - 3.5	0.51 ± 0.06	0.45 ± 0.08
3.5 - 4.0	0.55 ± 0.08	0.45 ± 0.10
4.0 - 5.0	0.64 ± 0.07	0.67 ± 0.11
5.0 - 6.0	0.60 ± 0.08	0.51 ± 0.10
6.0 - 8.0	0.79 ± 0.11	0.57 ± 0.11
8.0 - 12.0	0.77 ± 0.21	0.64 ± 0.20

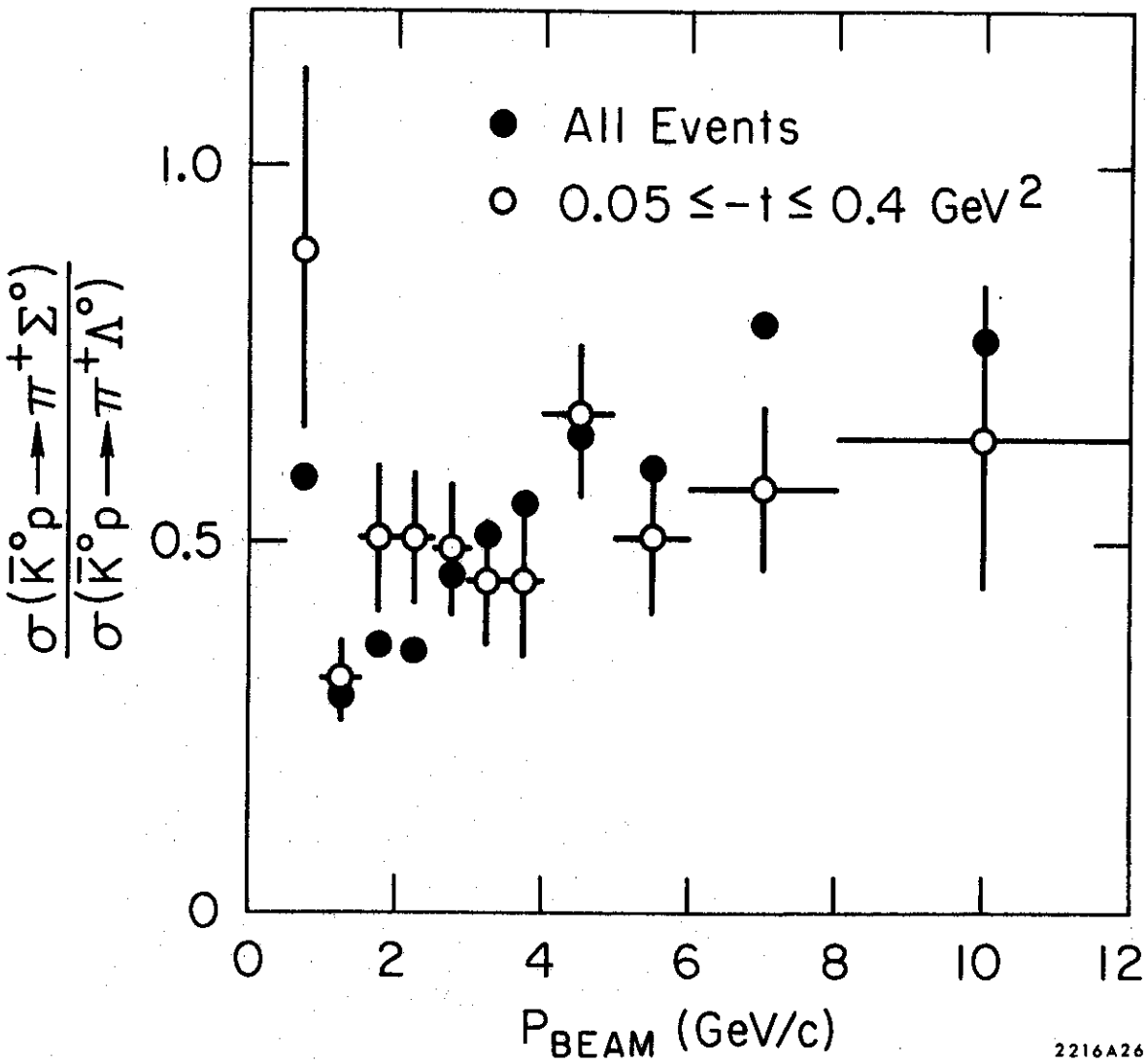

FIG. 23--The ratio $\sigma(\pi^+\Sigma^0)/\sigma(\pi^+\Lambda)$ versus incident momentum for all momentum transfers (solid points), and for $0.05 \leq -t \leq 0.4$ GeV^2 (open points).

important in $\pi^+\Lambda$ than in $\pi^+\Sigma^0$ for momenta $\lesssim$ 3 GeV/c (see Section 4D). Secondly, we note that the $\pi^+\Lambda$ differential cross section in the very forward direction $0.0 \leq -t \leq 0.05$ GeV^2 appears to flatten as the energy increases, whereas the $\pi^+\Sigma^0$ data show no signs of such a trend. Differences in final state interactions or different helicity flip/non-flip coupling strengths are possible sources of these small t effects. Hence, elimination of the very forward region $-t \leq 0.05$ GeV^2, as well as the region where non-peripheral contributions begin to enter should yield a more constant value for $\sigma(\pi^+\Sigma^0)/\sigma(\pi^+\Lambda)$. Indeed Table 7 and Figure 23 (open data points) show the Σ^0/Λ cross section ratios for $0.05 \leq -t \leq 0.4$ GeV^2 to be relatively energy independent above 1.5 GeV/c, as might be expected from a simple picture involving K* and K** Regge exchanges. An average of $\sigma_{\pi\Sigma}/\sigma_{\pi\Lambda} = 0.513 \pm 0.017$ is obtained for these data in the interval $1.5 \leq P_{BEAM} \leq 12$ GeV/c.

We also note that some of the rise in the Σ^0/Λ ratio may possibly be the result of phase space and angular momentum barrier differences arising from the inequality of the Λ and Σ^0 masses. Trilling[37] has pointed out that a factor $\left(\frac{p_i}{p_f}\right)^{2\ell+1}$ must be included before making comparisons between reactions involving unequal mass initial and final states. A relative rise of ~25% in the Σ^0/Λ ratio between 1.5 GeV/c and 5 GeV/c is accommodated by this factor.

D. Differential Cross Sections

The method of calculating the differential cross sections is nearly identical to the procedure for obtaining $\sigma(p)$ except that we now have

$$\frac{d\sigma}{dt}(p,t) = \frac{\langle\sigma\rangle}{\langle W\rangle} \frac{\Delta P_N}{\Delta p} \frac{1}{\Delta t} \sum_{i=1}^{n(p,t)} \frac{k_i}{F(p_i)}$$

where

$n(p, t)$ = number of events in the momentum interval Δp and four-momentum transfer interval Δt centered at p and t and taken from the identical film sample as used in calculating $< W >$.

Choice of the beam momentum intervals Δp, over which the differential cross sections were averaged, was governed primarily by the level of statistics.

The data for both final states are presented first as a function of $\cos\theta$ in Table 8 and Figs. 24 and 25, and then the forward scattering data are given as a function of momentum transfer, t, in Table 9 and Figs. 27 and 28. Figure 29 depicts the relationship between $\cos\theta$ and t as a function of beam momentum. All data are presented in five momentum intervals between 1.5 and 12 GeV/c. As with the total cross sections all errors have been folded in, excepting the overall normalization uncertainty of $\leq 15\%$. Results for the interval $0 < t < t_{MIN}$ are not given because of large uncertainties in the event weights, but examination of the kinematics (Fig. 30) for the reactions shows that this interval is quite small for $P_{BEAM} \gtrsim 2.5$ GeV/c.

Both Λ and Σ reactions are characterized by a sharp forward peak, and a backward peaking for the data with $P_{BEAM} > 3.5$ GeV/c. The cross section at 90° appears to fall off faster with increasing momenta than in any other region of $\cos\theta$, as has been discussed elsewhere.[38]

The cross sections obtained by integrating over the backward region, $-0.7 \geq \cos\theta \geq -1$, are shown in Fig. 26, and fitting these data with the power law dependence: $\sigma_{BACK} = Ap^{n}$ yields $(765 \pm 246\ \mu b)\ P_{BEAM}^{-3.2 \pm 0.3}$ for $\pi^{+}\Lambda$ and $(155 \pm 70\ \mu b)\ P_{BEAM}^{-2.1 \pm 0.4}$ for $\pi^{+}\Sigma^{o}$ for momenta > 1.5 GeV/c. Thus the ratio of Λ to Σ backward cross sections decreases rapidly with momentum, with the exponent $n_{\Lambda} - n_{\Sigma} = -1.1 \pm 0.5$. Only N exchange contributes to the $\pi^{+}\Lambda$

TABLE 8

Differential Cross Sections
(in μb/steradian)

$\bar{K}^o p \rightarrow \pi^+ \Lambda$						
Cos θ		Beam Momentum Interval (GeV/c)				
		1.5 - 2.5	2.5 - 3.5	3.5 - 5	5 - 8	8 - 12
-1.0	-0.9	52 ± 13	11 ± 5			
-0.9	-0.75	56 ± 11	8.6 ± 3.1	5.2 ± 1.1	0.54 ± 0.24	0.20 ± 0.30
-0.75	-0.5	47 ± 8	23 ± 4			0.14
-0.5	-0.2	101 ± 10	15 ± 3			
-0.2	0.2	85 ± 8	13 ± 2	1.9 ± 0.4	0.23 ± 0.12	---
0.2	0.5	91 ± 9	24 ± 3			
0.5	0.7	107 ± 11	23 ± 4	6.2 ± 1.4	0.78 ± 0.39	---
0.7	0.8	106 ± 15	46 ± 8	12 ± 3	3.3 ± 1.1	---
0.8	0.9	175 ± 20	110 ± 12	50 ± 6	12 ± 2	2.7 ± 4.0 1.9
0.9	0.95	341 ± 44	157 ± 20	105 ± 12	33 ± 5	7.3 ± 3.5
0.95	1.0	442 ± 65	250 ± 27	197 ± 18	160 ± 13	72 ± 14

$\bar{K}^o p \rightarrow \pi^+ \Sigma^o$						
Cos θ		Beam Momentum Interval (GeV/c)				
		1.5 - 2.5	2.5 - 3.5	3.5 - 5	5 - 8	8 - 12
-1.0	-0.75	16 ± 4	12 ± 3	3.6 ± 0.9	0.61 ± 0.30	0.55 ± 0.51
-0.75	-0.5	17 ± 5	5.0 ± 1.9			0.31
-0.5	-0.2	31 ± 6	5.3 ± 1.6			
-0.2	0.2	19 ± 4	9.1 ± 1.9	0.95 ± 0.30	< 0.092*	---
0.2	0.5	24 ± 5	6.3 ± 1.8			
0.5	0.7	29 ± 6	8.6 ± 2.5	3.7 ± 1.2	1.1 ± 0.5	---
0.7	0.8	26 ± 8	12 ± 4	5.8 ± 2.1	1.3 ± 0.8	---
0.8	0.9	106 ± 17	32 ± 6	11 ± 2.8	2.8 ± 1.1	---
0.9	0.95	212 ± 35	114 ± 18	47 ± 8	14 ± 3	1.1 ± 1.6 0.8
0.95	1.0	245 ± 41	164 ± 22	173 ± 17	132 ± 12	62 ± 13

*Corresponds to 1.9 events (85% confidence level) when no events are observed.

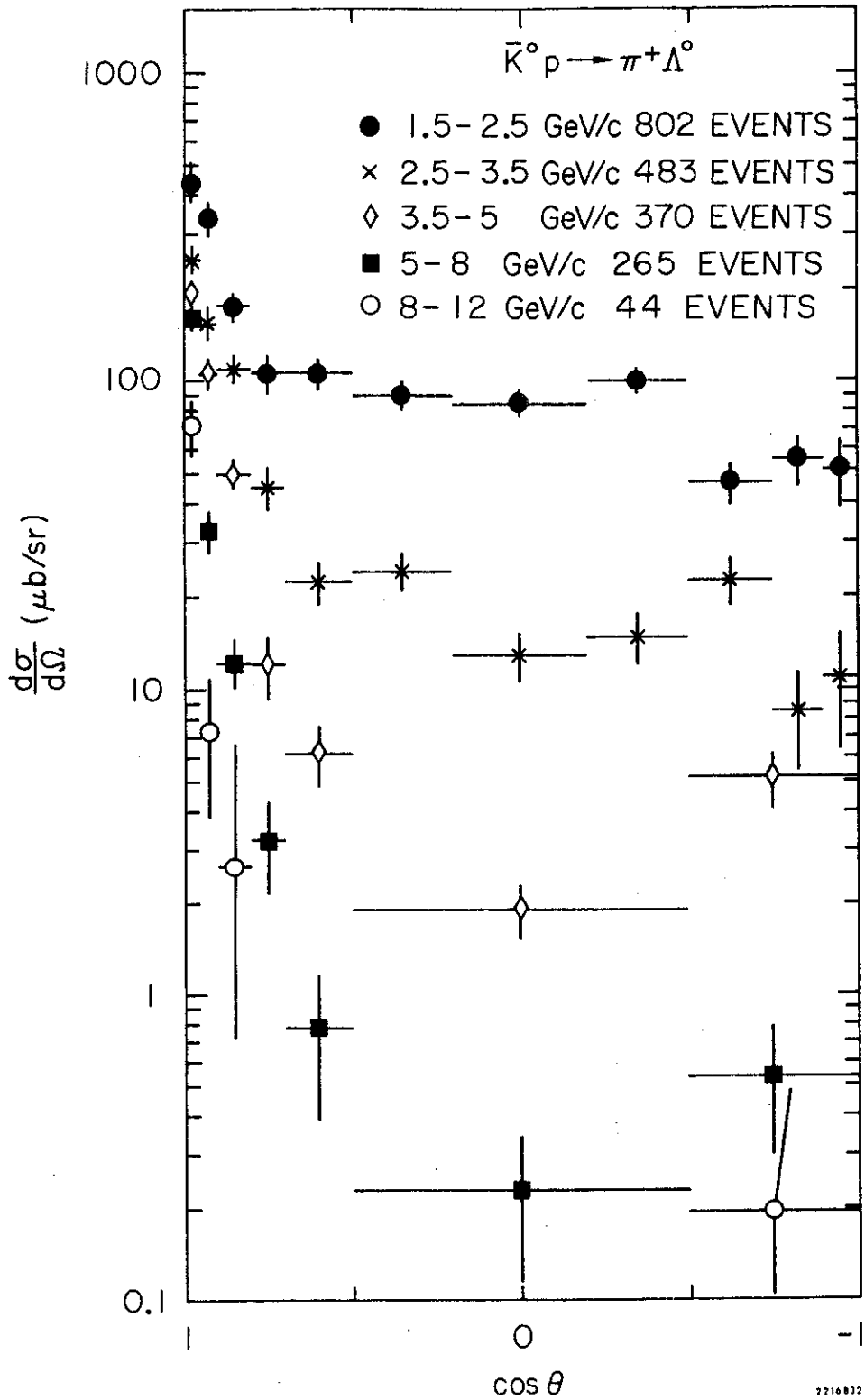

FIG. 24--Differential cross sections versus $\cos\theta$ in the center of mass for $\bar{K}^0 p \rightarrow \pi^+ \Lambda$.

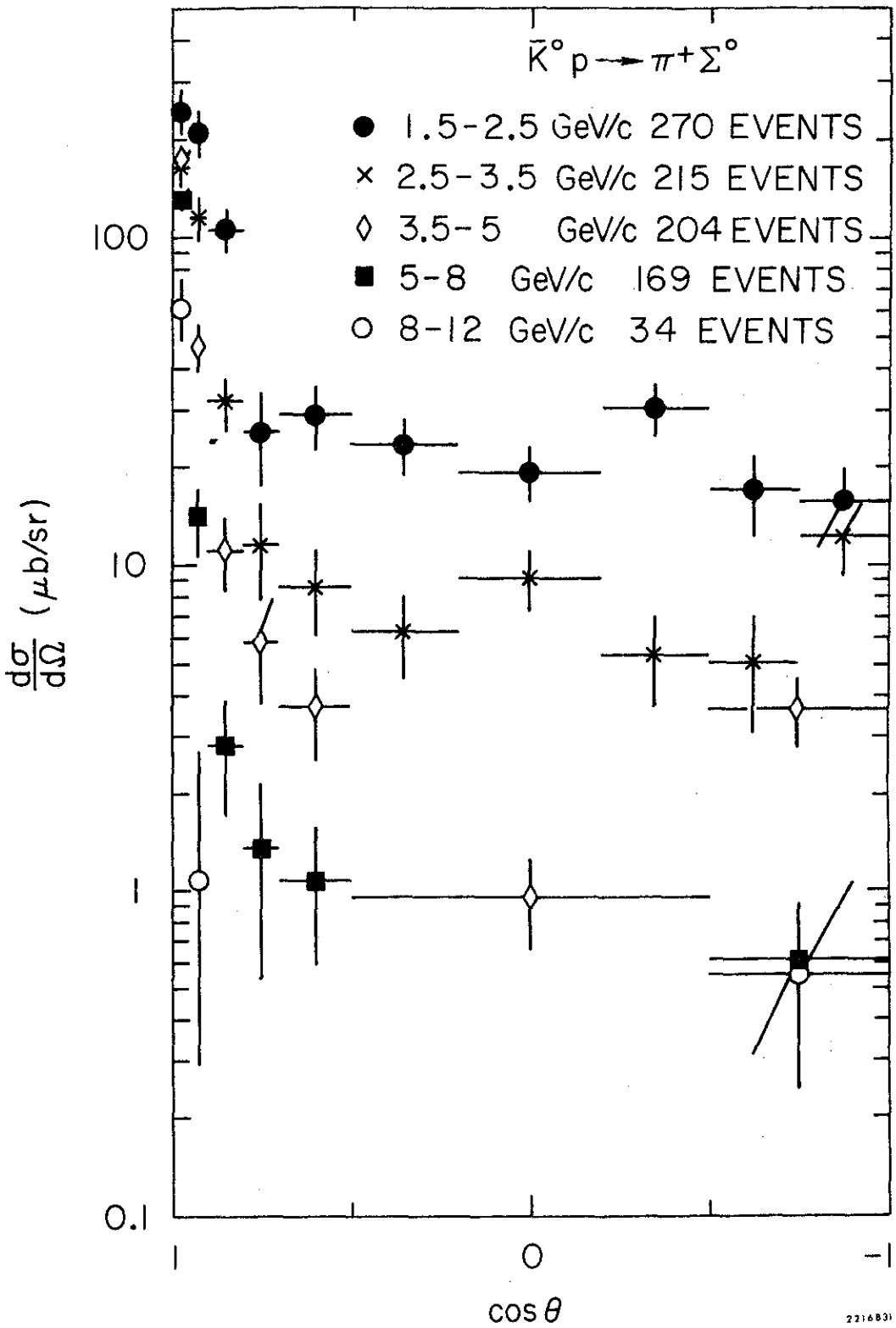

FIG. 25--Differential cross sections versus cosθ in the center of mass for $\bar{K}^o p \rightarrow \pi^+ \Sigma^o$.

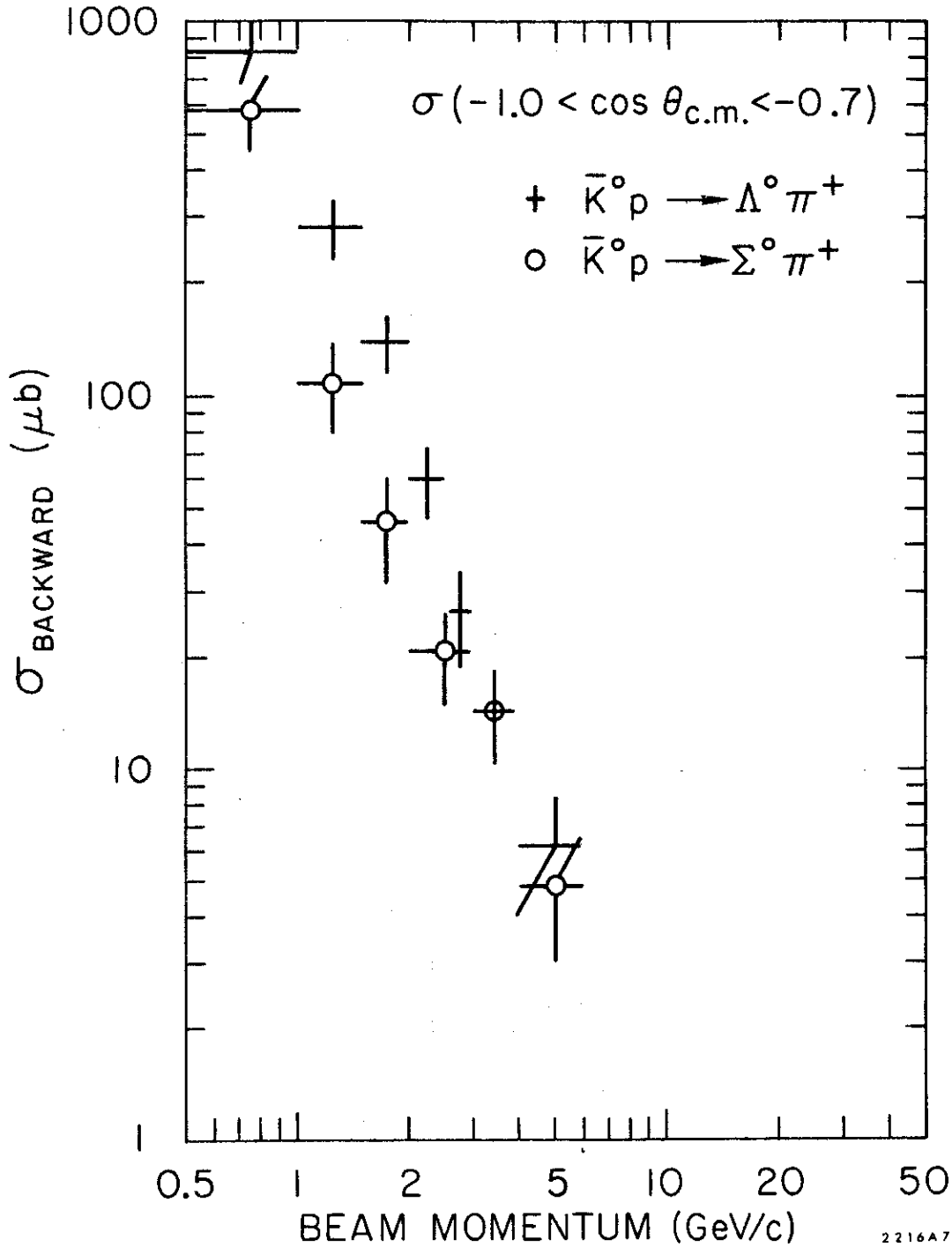

FIG. 26--The backward integrated ($-1.0 \leq \cos\theta_{c.m.} \leq -0.7$) cross section versus incident momentum for $\bar{K}^o p \rightarrow \pi^+ \Lambda$ and $\bar{K}^o p \rightarrow \pi^+ \Sigma^o$.

backward cross section while both N and Δ exchange can contribute to the $\pi^+\Sigma^0$ channel. Thus the difference in momentum dependences for the Λ and Σ^0 data suggests that Δ exchange dominates the $\pi^+\Sigma^0$ channel.† In fact, we note that the difference in P_{BEAM} dependence, $n_\Lambda - n_\Sigma$, is consistent with the difference in the Regge intercepts $2[\alpha_{N_\alpha}(0) - \alpha_{\Delta_\delta}(0)] = -1.1$.[39]

Considering the data as a function of momentum transfer t we see strong forward peaking in both channels at all momenta. Both reactions also have a break in slope near $-t \sim 0.3$ GeV^2 at low momenta, which appears to move out to $-t \sim 0.4$-0.5 GeV^2 at higher momenta. The forward peaking together with the lack of any significant miminum near $-t \sim 0.6$ GeV^2 can be taken as evidence for helicity non-flip dominance.[13, 40-42]

Data in the forward region have been parameterized with an exponential form, $\frac{d\sigma}{dt} = Ae^{bt}$, and the results are presented in Table 10 along with the average t_{MIN} values for each momentum interval. In the $\pi^+\Sigma^0$ channel the data are consistent with being exponential all the way to t=0, while in the $\pi^+\Lambda$ final state the data in the first t bin ($0.0 \leq -t \leq 0.05$ GeV^2) suggest a turnover or flattening out of the cross section in the forward direction. However, we observe that the parameters obtained when the first bin is excluded or included agree within errors. We note that the $K^-p \rightarrow \pi^0\Lambda$ data of Mason and Wohl[31c] at 3.13 and 3.30 GeV/c show simple exponential behavior to t=0 while their data at 3.59 GeV/c and the data of Moscoso et al[31e] at 3.93 GeV/c exhibit a flattening out in the forward direction; hence, the situation at $t \approx 0$ remains unclear for the $\pi\Lambda$ final state.

---

† The dominance of Δ exchange in backward $\Sigma\pi$ scattering is consistent with $g^2_{KN\Lambda} >> g^2_{KN\Sigma}$ (see Ref. 21) and the observation that the $\Lambda\pi$ and $\Sigma\pi$ backward cross sections are of the same order of magnitude.

TABLE 9

Differential Cross Sections

(in $\mu b/GeV^2$)

$\bar{K}^o p \rightarrow \pi^+ \Lambda^o$					
$-t$ (GeV^2)	Beam Momentum Interval (GeV/c)				
	1.5 - 2.5	2.5 - 3.5	3.5 - 5	5 - 8	8 - 12
0.0 - 0.05	1813 ± 338	726 ± 139	439 ± 80	229 ± 45	94 ± 57
0.05 - 0.1	1518 ± 248	735 ± 119	300 ± 56	293 ± 45	123 ± 49
0.1 - 0.2	931 ± 115	500 ± 63	301 ± 35	151 ± 20	55 ± 17
0.2 - 0.3	522 ± 84	369 ± 54	174 ± 27	81 ± 15	40 ± 14
0.3 - 0.4	605 ± 97	241 ± 43	124 ± 23	58 ± 13	14 ± 7
0.4 - 0.5	642 ± 100	211 ± 40	122 ± 22	16 ± 6	20 ± 13
0.5 - 0.6	641 ± 100	97 ± 19	58 ± 11	27 ± 6	2.4 ± $^{2.3}_{1.4}$
0.6 - 0.7	377 ± 77				
0.7 - 1.0	547 ± 57	70 ± 14	29 ± 6	8.4 ± 2.6	
1.0 - 1.5	479 ± 43	77 ± 12	13 ± 3	4.8 ± 1.7	1.7 ± $^{2.5}_{1.2}$
1.5 - 2.0	307 ± 34	49 ± 9	6.4 ± 2.4	1.0 ± $^{0.9}_{0.6}$	
2.0 - 2.5	179 ± 24	46 ± 10	6.1 ± 2.5	0.51 ± $^{0.47}_{0.29}$	----
2.5 - 3.0	76 ± 15	45 ± 9	1.1 ± $^{1.7}_{0.8}$	----	----

$\bar{K}^o p \quad \pi^+ \Sigma^o$					
$-t$ (GeV^2)	Beam Momentum Interval (GeV/c)				
	1.5 - 2.5	2.5 - 3.5	3.5 - 5	5 - 8	8 - 12
0.0 - 0.1	1025 ± 154	403 ± 69	393 ± 51	273 ± 35	101 ± 34
0.1 - 0.2	612 ± 101	315 ± 52	166 ± 27	92 ± 17	48 ± 16
0.2 - 0.3	266 ± 63	132 ± 32	71 ± 18	46 ± 11	34 ± 17
0.3 - 0.4	107 ± 48	55 ± 15	30 ± 8	5.7 ± 2.5	1.7 ± $^{2.5}_{1.2}$
0.4 - 0.5	227 ± 65				
0.5 - 0.7	169 ± 38	34 ± 12	15 ± 6	4.1 ± 1.5	----
0.7 - 1.0	98 ± 26	29 ± 9	9.0 ± 3.7		
1.0 - 1.5	122 ± 21	17 ± 6	8.5 ± 2.9	2.1 ± 1.1	----
1.5 - 2.0	94 ± 21	33 ± 8	4.7 ± 2.1	2.2 ± 1.1	----
2.0 - 2.5	57 ± 13	18 ± 6	1.8 ± $^{1.6}_{1.0}$	----	----
2.5 - 3.0	12 ± 5	16 ± 6	2.1 ± $^{1.9}_{1.2}$	----	----

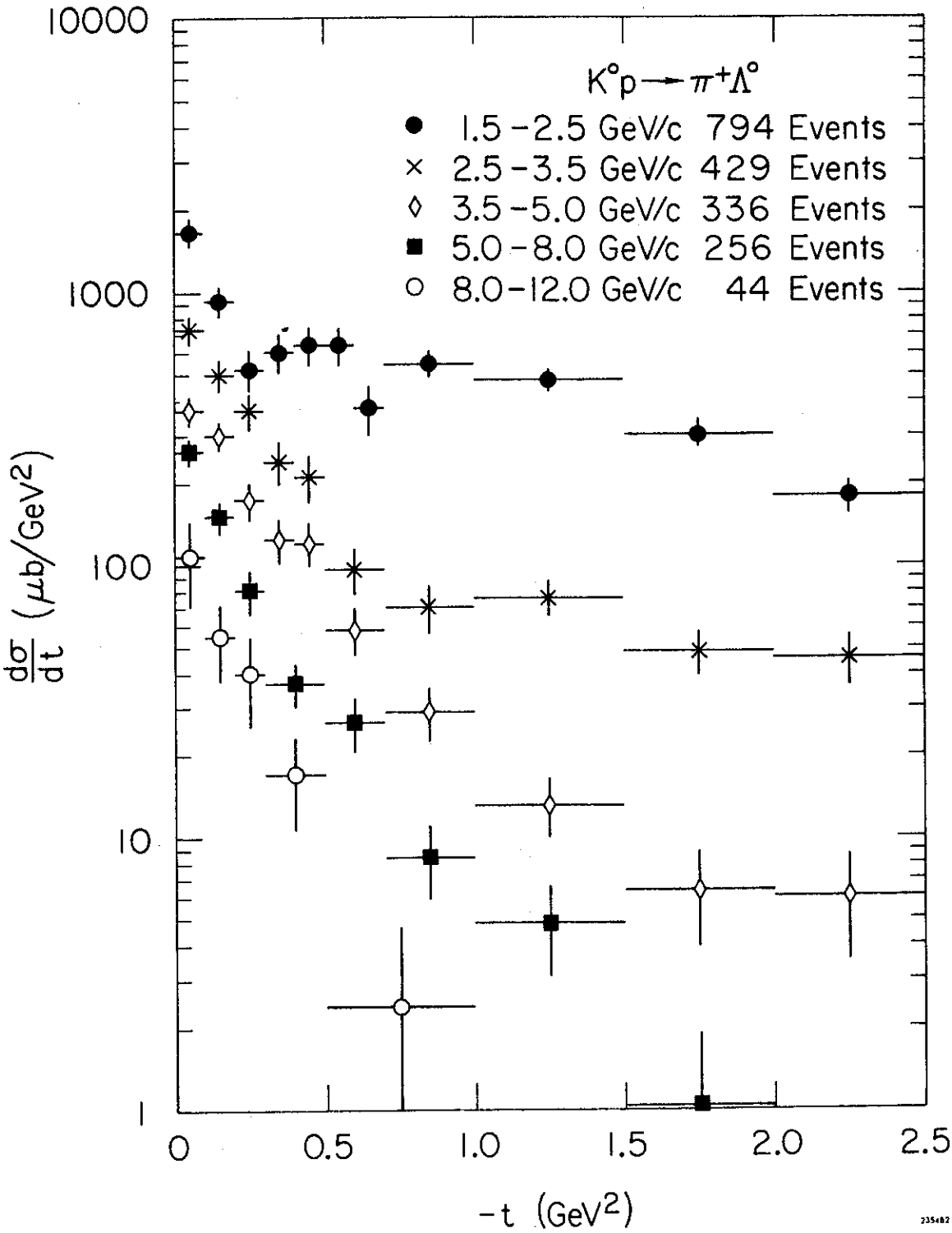

FIG. 27--Differential cross sections versus momentum transfer for $\bar{K}^o p \rightarrow \pi^+ \Lambda$.

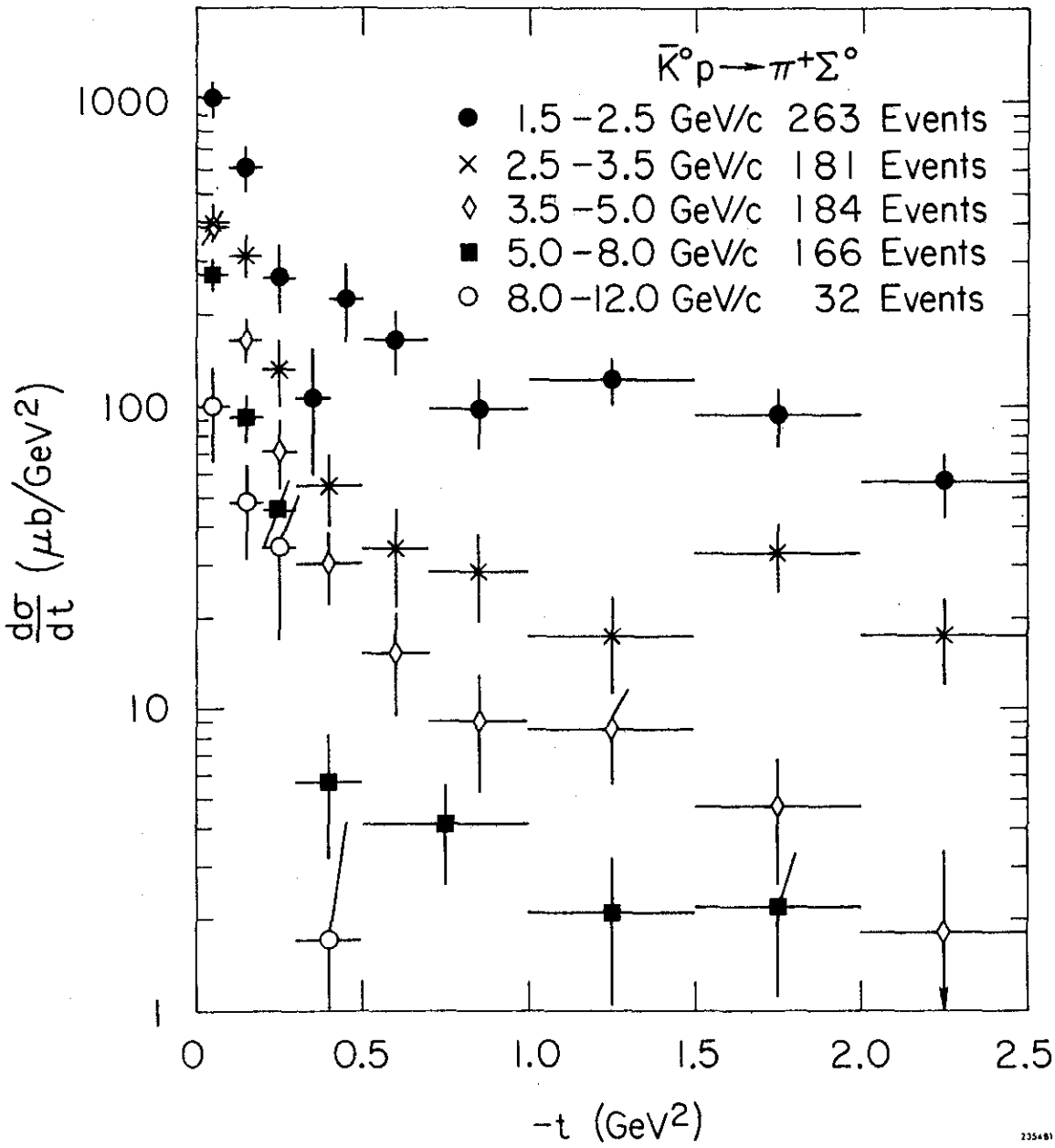

FIG. 28--Differential cross sections versus momentum transfer for $\bar{K}^o p \rightarrow \pi^+ \Sigma^o$.

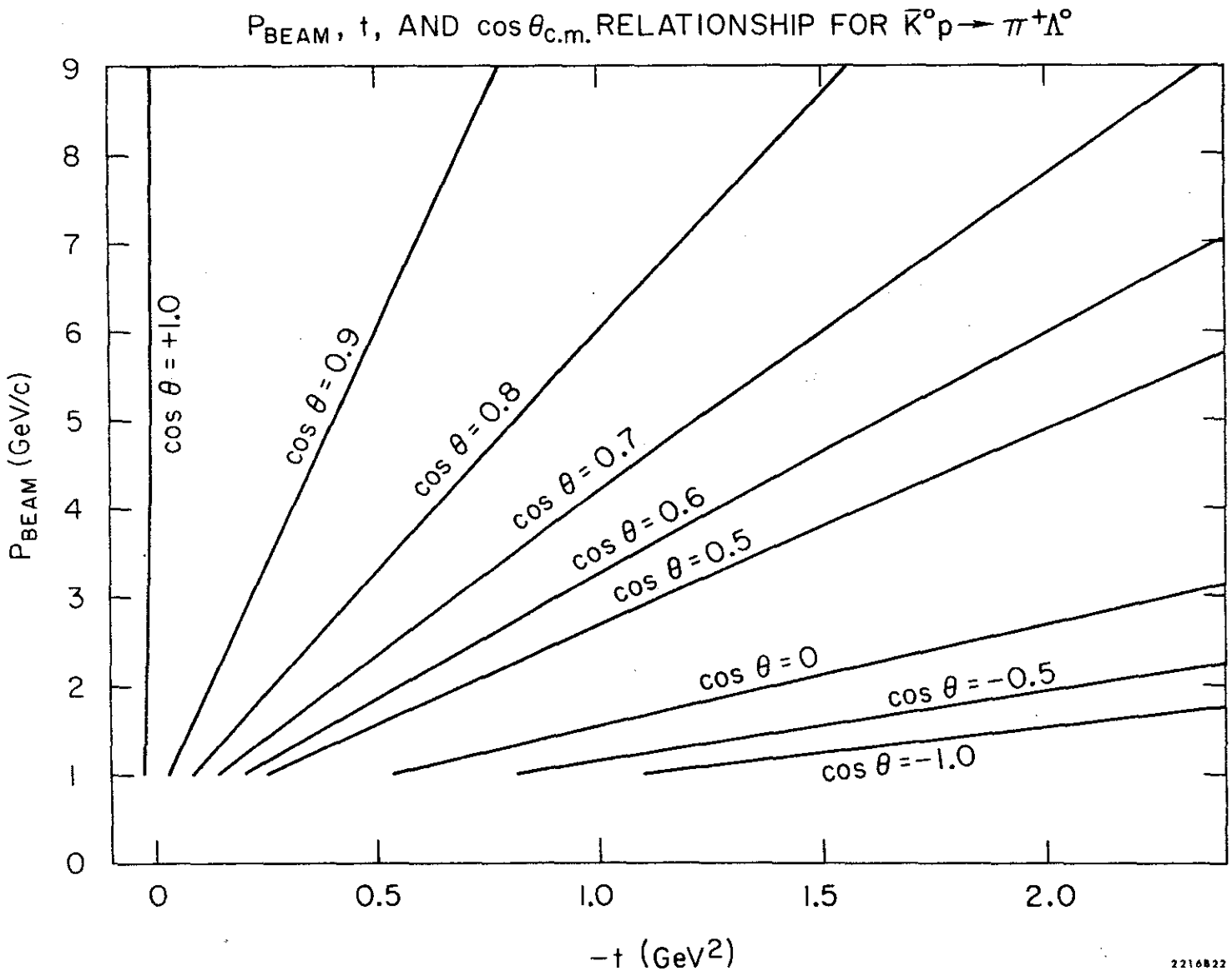

FIG. 29--Relationship between center of mass scattering angle, $\cos\theta$, and momentum transfer, t, as a function of beam momentum for the reaction $\bar{K}^o p \rightarrow \pi^+ \Lambda$. The relationship for $\bar{K}^o p \rightarrow \pi^+ \Sigma^o$ does not differ significantly.

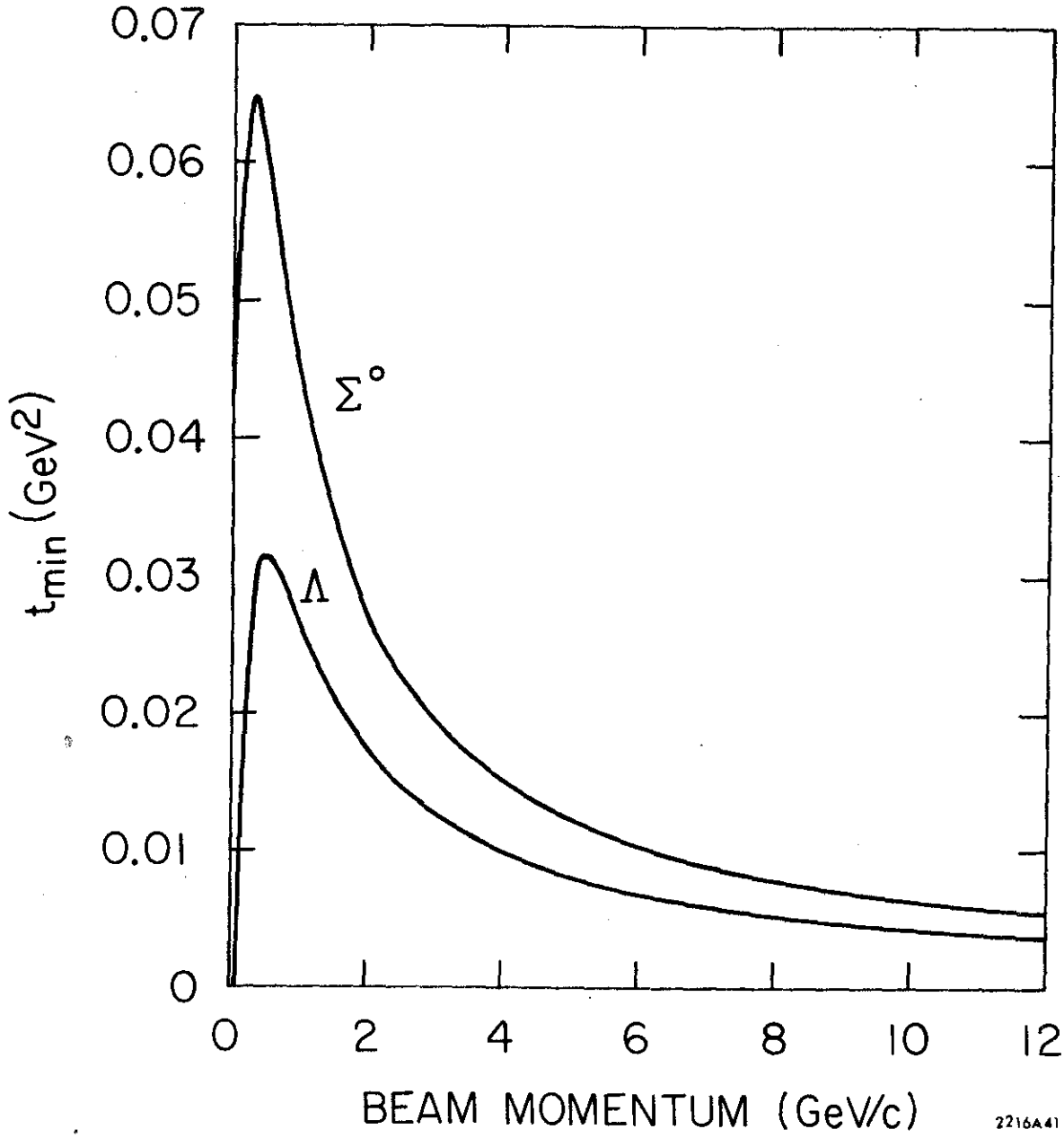

FIG. 30--Momentum transfers, t_{MIN}, corresponding to zero degree scattering for the reactions $\bar{K}^o p \rightarrow \pi^+ \Lambda$ and $\bar{K}^o p \rightarrow \pi^+ \Sigma^o$.

The slope parameters from the fits which included the $0.0 \leq -t \leq 0.05$ GeV^2 data are shown in Fig. 31. Superimposed are lines indicating the average slope of previous $K^-N \rightarrow \Lambda\pi$ data as well as the nearly momentum independent slope obtained from $\pi^-p \rightarrow \Lambda K^0$ data.[36] Exchange degeneracy demands that the slopes be equal for the π and $\overline{K}$ induced reactions, yet previous data indicate a three standard deviation separation of the average slope values.[9] Our data, while being consistent with previous K^-N data, suggest shrinkage of the forward slope for the $\overline{K}$ induced reactions implying possible convergence of the π and $\overline{K}$ induced reaction slopes near 10 GeV/c.

The situation is quite analogous for the reactions involving a Σ^0. Slopes for the π induced reactions are large ($\sim$ 9 GeV^{-2}) and remain relatively constant with increasing incident momenta[36] while our data and data on $K^-p \rightarrow \Sigma^+\pi^-$,[32] indicate shrinkage of the forward slope for the $\overline{K}$ induced reaction, with possible equality of the π and $\overline{K}$ induced reaction slopes for $P_{BEAM} \gtrsim 6$ GeV/c.

We turn now to the forward cross sections, $\left(\frac{d\sigma}{dt}\right)_{t=t_{MIN}} = Ae^{bt_{MIN}}$, obtained from the parameters of Table 10. We observe the Σ^0/Λ forward cross section ratio, R, to rise from 0.73 ± 0.11 for $1.5 \leq P_{BEAM} \leq 3.5$ GeV/c to 1.31 ± 0.19 for $3.5 \leq P_{BEAM} \leq 12$ GeV/c.† If one assumes equality of the vector and tensor amplitudes (octet dominance) and common F/D ratios, it can be shown[40] that

$$R = 3\left(\frac{2F_+ - 1}{2F_+ + 1}\right)^2$$

† Failure to extrapolate to $t = t_{MIN}$ gives somewhat lower $R_{t=0}$ values of 0.67 ± 0.10 for $1.5 \leq P_{BEAM} \leq 3.5$ GeV/c and 1.22 ± 0.18 for $3.5 \leq P_{BEAM} \leq 12$ GeV/c; however, this does not significantly alter our interpretation.

TABLE 10

Forward Cross Sections Fit to Ae^{bt}

$\bar{K}^o p \rightarrow \pi^+ \Lambda$

P_{BEAM} Interval (GeV/c)	-t Interval (GeV^2)	$A \frac{\mu b}{GeV^2}$	$b(GeV^{-2})$	$\langle t_{MIN} \rangle$ (GeV^2)
1.5 - 2.5	0.05 - 0.3	2470 ± 573	6.6 ± 1.4	0.0175
2.5 - 3.5	0.05 - 0.4	935 ± 161	3.9 ± 0.8	0.0127
3.5 - 5	0.05 - 0.4	453 ± 79	3.6 ± 0.8	0.0094
5 - 8	0.05 - 0.4	395 ± 82	6.2 ± 1.1	0.0064
8 - 12	0.05 - 0.4	148 ± 61	6.7 ± 2.1	0.0043
1.5 - 2.5	0.0 - 0.3	2235 ± 344	6.0 ± 1.0	0.0175
2.5 - 3.5	0.0 - 0.4	868 ± 115	3.6 ± 0.7	0.0127
3.5 - 5	0.0 - 0.4	465 ± 62	3.8 ± 0.7	0.0094
5 - 8	0.0 - 0.4	303 ± 52	5.0 ± 0.9	0.0064
8 - 12	0.0 - 0.4	137 ± 48	6.3 ± 1.9	0.0043

$\bar{K}^o p \rightarrow \pi^+ \Sigma^o$

1.5 - 2.5	0.0 - 0.4	1408 ± 228	6.7 ± 1.0	0.0274
2.5 - 3.5	0.0 - 0.5	619 ± 101	6.3 ± 0.8	0.0195
3.5 - 5	0.0 - 0.5	527 ± 77	7.7 ± 0.9	0.0143
5 - 8	0.0 - 0.5	423 ± 66	10.7 ± 1.1	0.0096
8 - 12	0.0 - 0.5	131 ± 57	9.2 ± 2.8	0.0064

When $\chi^2/NDF > 1$ errors on fitted quantities have been scaled up by the factor $\sqrt{\chi^2/NDF}$.

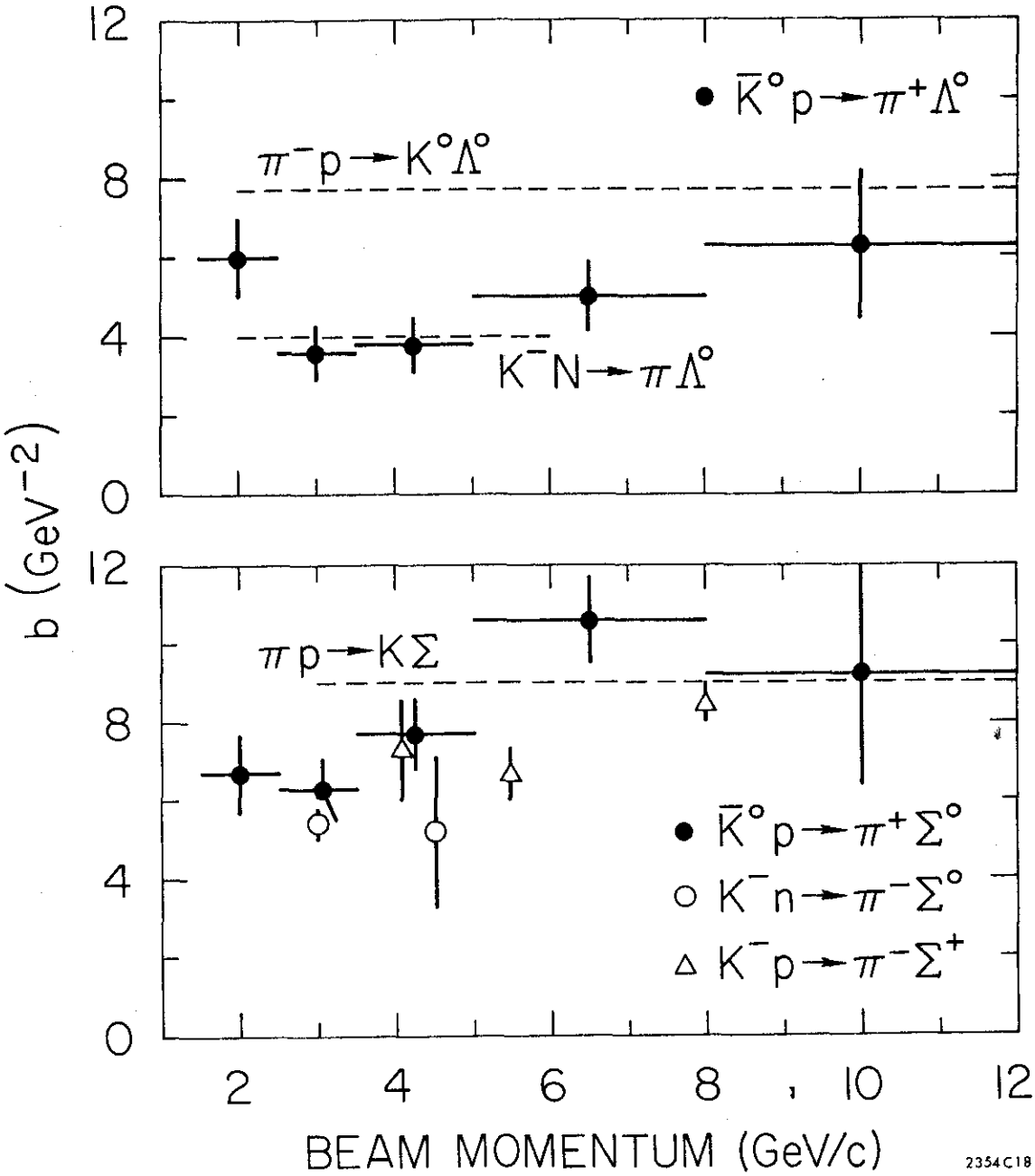

FIG. 31--Forward slopes for $\bar{K}^0 p \to \pi^+ \Lambda$ (upper figure) and $\bar{K}^0 p \to \pi^+ \Sigma^0$ (lower figure) versus beam momentum determined in the momentum interval $0.0 \leq -t \leq 0.3\text{-}0.5$ GeV^2 (see Table 10). Dotted lines represent average slope values for the indicated reactions.

where F_+ is the helicity non-flip f-type coupling constant. Solving for F_+ and choosing the solution corresponding to 0° relative phase between the Λ, Σ^o amplitudes we obtain

$$F_+ = \frac{1}{2}\left(\frac{1 + \sqrt{R/3}}{1 - \sqrt{R/3}}\right).$$

This relation gives $F_+ = 1.47 \pm {}^{0.15}_{0.14}$ for $1.5 \leq P_{BEAM} \leq 3.5$ GeV/c in good agreement with the canonical value of $F_+ \approx 3/2$.[42] At higher momenta, however, we find a larger value of $F_+ = 2.6 \pm {}^{0.47}_{0.38}$, which reflects the ~80% rise in R. Only about one-fourth of this increase in R can be accounted for by phase space and angular momentum barrier correction factors.† The remainder of this rise may be the result of differences in Λ, Σ^o final state interactions.

Finally, to determine the "effective trajectories", the data has also been fit to the functional form $s^{2\alpha(t)}/P^2_{BEAM}$. The results are given in Table 11 and are shown in Fig. 32. The data in both channels give values of $\alpha(t)$ consistent with the straight line trajectory, Re $\alpha = 0.35 + 0.82t$, which passes through both K*s. However, the $\Sigma^o\pi^+$ data appears to follow a somewhat steeper trajectory.

E. Polarizations

Parity violation in the weak decay $\Lambda \rightarrow p\pi^-$ makes it possible to measure the lambda polarization, P_Λ, by observing the angular distribution of the proton with respect to the normal $\hat{n}$ to the production plane.[43] The proton distribution is proportional to

$$I(\theta) = 1 + \alpha P_\Lambda \cos\theta$$

† Inclusion of Trilling factors (see text) raises the Σ/Λ forward cross section ratio to 1.06 ± 0.16 and 1.70 ± 0.25 respectively for the two momentum intervals considered.

TABLE 11

Effective Regge Trajectory

$\bar{K}^o p \rightarrow \Lambda \pi^+$

-t Interval (GeV^2)	α_{EFF}	P_{BEAM} Interval (GeV/c)
0.0 - 0.1	0.24 ± 0.19	3 - 9
0.1 - 0.2	0.13 ± 0.22	3 - 9
0.2 - 0.3	0.19 ± 0.29	3 - 9
0.3 - 0.5	-0.21 ± 0.27	3 - 9
0.5 - 0.8	-0.05 ± 0.31	3 - 9
0.8 - 1.2	-0.60 ± 0.62	3 - 7
1.2 - 2.0	-1.31 ± 0.83	3 - 6
$\bar{K}^o p \rightarrow \Sigma^o \pi^+$		
0.0 - 0.1	0.64 ± 0.18	3 - 10
0.1 - 0.2	0.35 ± 0.27	3 - 10
0.2 - 0.4	-0.08 ± 0.36	3 - 9
0.4 - 1.0	-0.60 ± 0.69	3 - 6

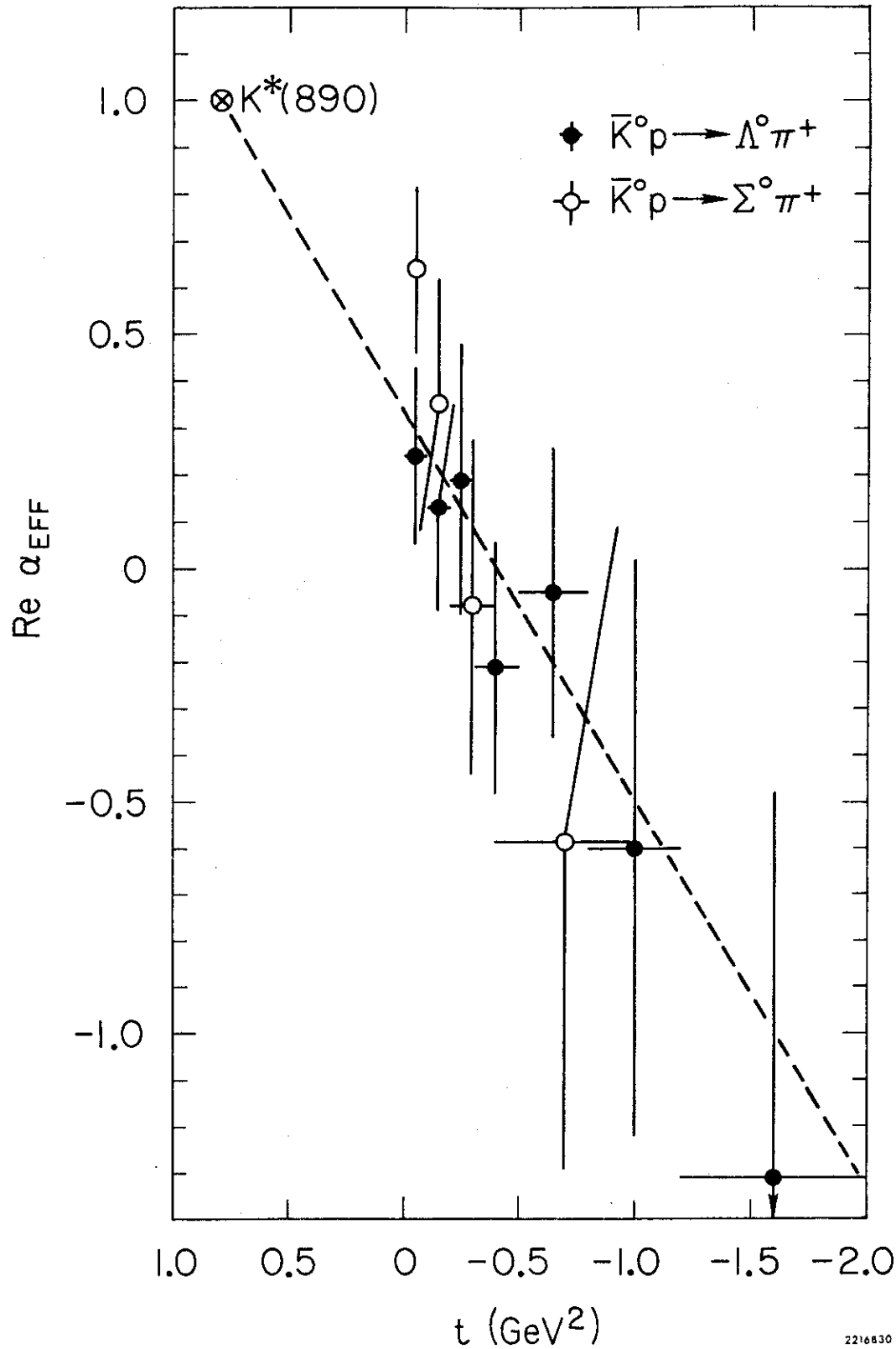

FIG. 32--Real part of the effective Regge trajectory versus momentum transfer for $\bar{K}^o p \rightarrow \pi^+ \Lambda$ (solid points) and $\bar{K}^o p \rightarrow \pi^+ \Sigma^o$ (open points). Dotted curve represents the conventional K* trajectory, Re α (t) $\approx$ 0.35 + 0.82 t.

where

$$\cos\theta = \hat{q}_p \cdot \hat{n}$$

$$\alpha = 0.645$$

$$\hat{n} = \hat{q}_i \times \hat{q}_f$$

and where $\hat{q}_i$, $\hat{q}_f$, and $\hat{q}_p$ are the momentum unit vectors of the incident meson ($\bar{K}^o$), outgoing meson (π^+), and decay proton respectively, as seen in the Λ rest frame. Now given a unit normalized probability distribution $I(z) = \frac{1}{2}(1 + az)$ where $z \equiv \cos\theta$, the first momentum M_1 is defined as

$$M_1 = \int_{-1}^{+1} z\, I(z)\, dz = \frac{a}{3},$$

and extension of this definition to a set of N discrete events gives

$$M_1 = \frac{\sum_{i=1}^{n} z_i}{N} = \langle z_i \rangle = \frac{a}{3}$$

Hence, the quantity αP_Λ is just equal to $3M_1$ so that we are led to the simple result

$$\alpha P_\Lambda = 3 \langle \cos\theta \rangle$$

The error on αP_Λ is given by $\left[\frac{3 - (\alpha P_\Lambda)^2}{N}\right]^{1/2}$.[44] Data on the reaction $\bar{K}^o p \rightarrow \pi^+ \Lambda$ were divided into two samples, $2.5 < P_{BEAM} < 3.8$ GeV/c and $P_{BEAM} > 3.8$ GeV/c, with about an equal number of events in each sample. Polarizations obtained from the two samples (Fig. 33 lower) are in good agreement and thus served as justification for combining all data with $P_{BEAM} > 2.5$ GeV/c. The data (Table 12 and Fig. 33 upper) show a large positive Λ

TABLE 12

Hyperon Polarization

$\bar{K}^o p \rightarrow \Lambda\pi^+$

-t (GeV^2)	$\alpha_\Lambda P_\Lambda$		
	$P_{BEAM} > 2.5$ GeV/c	$2.5 < P_{BEAM} < 3.8$ GeV/c	$P_{BEAM} > 3.8$ GeV/c
0.0 - 0.2	0.21 ± 0.08	0.30 ± 0.13	0.15 ± 0.10
0.2 - 0.4	0.36 ± 0.11	0.32 ± 0.17	0.39 ± 0.15
0.4 - 0.7	0.59 ± 0.14	0.66 ± 0.15	0.64 ± 0.15
0.7 - 1.1	0.77 ± 0.18		
1.1 - 2.0	0.21 ± 0.18	0.23 ± 0.14	0.44 ± 0.32
2.0 - 3.4	0.32 ± 0.19		

$\bar{K}^o p \rightarrow \Sigma^o \pi^+$

-t (GeV^2)	$\alpha_\Lambda P_\Sigma$ $P_{BEAM} > 2.5$ GeV/c
0.0 - 0.2	-0.18 ± 0.16
0.2 - 0.4	-0.83 ± 0.32
0.4 - 1.1	-0.28 ± 0.41
1.1 - 3.4	-0.06 ± 0.35

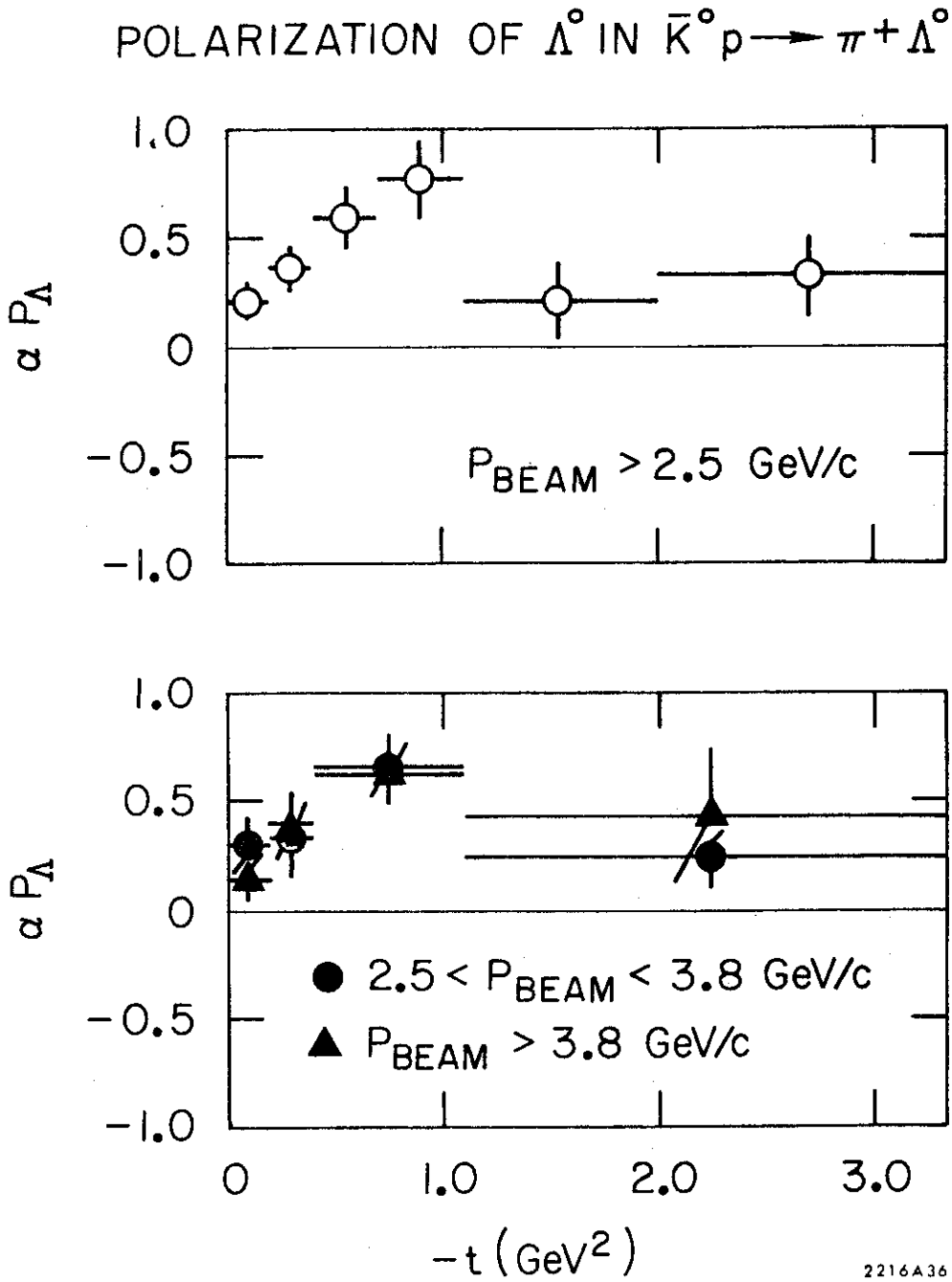

FIG. 33--Polarization of the Λ in $\bar{K}^o p \rightarrow \pi^+ \Lambda$ versus momentum transfer.

polarization, rising rapidly from zero in the forward direction, where it must vanish by angular momentum conservation, peaking near $-t \sim 0.9\ \mathrm{GeV}^2$, and falling slowly at larger t.

This is in good agreement with the polarization behavior observed in $K^-N \rightarrow \pi\Lambda$ data. Comparison with the polarization data fron πN experiments[36] show that for $-t > 0.3\ \mathrm{GeV}^2$ there is agreement with the EXD prediction of the polarization changing sign under line reversal. However, for $-t < 0.3\ \mathrm{GeV}^2$ both π and K induced reactions show positive polarization, in violation of the simple EXD hypothesis.

Further justification for combining the polarization data for all beam momenta above 2.5 GeV/c is demonstrated in Fig. 34, which shows the quantity $<\alpha P_\Lambda>$ averaged over the momentum transfer interval $0.2 \leq -t \leq 1.0\ \mathrm{GeV}^2$ † as a function of P_{BEAM}. The momentum independence of $<\alpha P_\Lambda>$, which is also tabulated in Table 13, is clearly evident above the s-channel resonance region ($P_{BEAM} \gtrsim 2$ GeV/c).

From a simple Regge picture the s, t dependence of the polarization would be of the form

$$P(s,t) = G(t) s^{\alpha_2(t) - \alpha_1(t)}$$

where $\alpha_1(t)$ and $\alpha_2(t)$ represent the two highest lying trajectories exchanged.[39] By identifying these two trajectories with the K*-K** pair, one might consider the momentum independence of $<\alpha P_\Lambda>$ as evidence for "weak" EXD of the K*, K** trajectories in the scattering region, $t < 0$.

---

† The momentum transfer limits for this averaging process were chosen mainly with the idea of minimizing $\delta <\alpha P_\Lambda> / <\alpha P_\Lambda>$, which implies choice of a t region where αP_Λ is large. It is advantageous, therefore, to avoid the abundant supply of low polarization events at small -t and also to eliminate the non-peripheral contributions at large momentum transfers.

TABLE 13

Average Hyperon Polarization

$0.2 \leq -t \leq 1.0\ \mathrm{GeV}^2$

$\bar{K}^o p \rightarrow \pi^+ \Lambda$

P_{BEAM} (GeV/c)	$\alpha_\Lambda P_\Lambda$
0.5 - 1.0	0.31 ± 0.17
1.0 - 1.5	0.15 ± 0.11
1.5 - 2.0	-0.19 ± 0.14
2.0 - 2.5	0.65 ± 0.13
2.5 - 3.0	0.49 ± 0.18
3.0 - 3.5	0.42 ± 0.20
3.5 - 4.0	0.54 ± 0.21
4.0 - 6.0	0.53 ± 0.13
6.0 - 10.0	0.54 ± 0.24

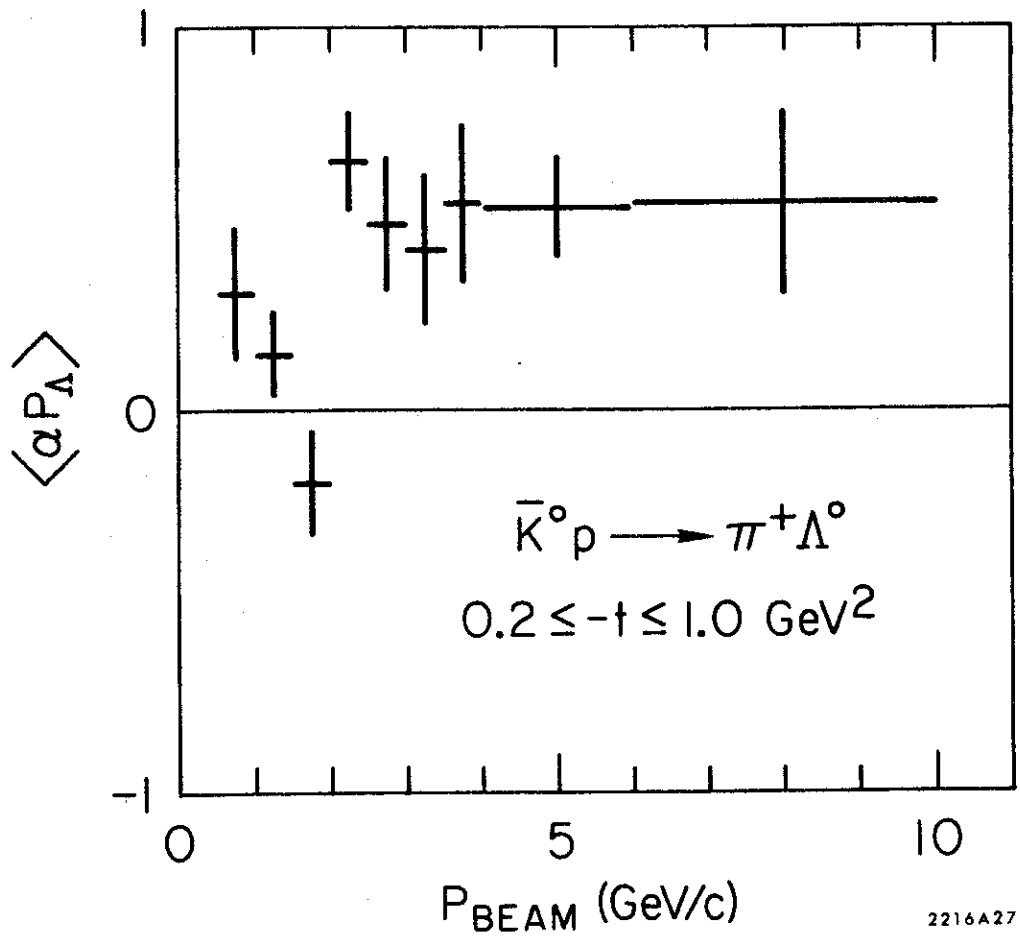

FIG. 34--Polarization of the Λ averaged over the interval $0.2 \leq -t \leq 1.0$ GeV^2 versus incident momentum for the reaction $\bar{K}^o p \rightarrow \pi^+ \Lambda$.

We have also determined the Σ^0 polarization using the relation[45]

$$\alpha P_\Sigma = -9 \langle (\hat{q}_\Lambda \cdot \hat{n})\ (\hat{q}_\Lambda \cdot \hat{q}_p) \rangle$$

where $\hat{q}_\Lambda$ is the momentum unit vector of the Λ in the Σ^0 rest frame. The minus sign comes from the spin flip associated with a spin 1/2 Σ^0 decaying into a spin 1/2 Λ and a spin 1 photon. The Σ^0 polarization for data with $P_{BEAM} > 2.5$ GeV/c is recorded in Table 12. The large errors, given by $\left[\frac{9-(\alpha P_\Sigma)^2}{N}\right]^{1/2}$ are the result of poor statistics coupled with the very forward peaking of $d\sigma/dt$.

F. Discussion

The sharp forward peaking and the absence of any significant dip structure near $-t \sim 0.6\ \mathrm{GeV}^2$ in the Λ or Σ^0 differential cross sections (see Fig. 27, 28) indicates that the s-channel helicity nonflip amplitude, f_{++}, dominates the $\bar{K}^0 p \to \pi^+(\Lambda^0, \Sigma^0)$ reactions. A similar result is found for the crossed reactions, $\pi^- p \to K^0(\Lambda, \Sigma^0)$,[36] confirming that K*, K** exchanges couple strongly to helicity nonflip at the baryon vertex.

For small values of momentum transfer the modulus of the helicity nonflip amplitude can be parameterized by a simple exponential

$$f_{++}(t) \sim e^{at}$$

which yields an impact parameter representation of the form

$$f_{++}(b) \sim e^{-b^2/4a}\ .$$

Alternatively, helicity flip amplitudes, f_{+-}, have an additional factor of $\sqrt{-t}$ from angular momentum conservation, and yield

$$f_{+-}(b) \sim b\ e^{-b^2/4a}\ .$$

Since absorption depletes the low partial waves (i.e., small b) it is apparent that while helicity nonflip amplitudes may be strongly modified by absorption, helicity flip amplitudes are relatively unaffected.[46] Hence, it would not be too surprising if evidence for exchange degeneracy was seriously obscured in hypercharge exchange reactions, while being easily visible in charge exchange reactions (involving ρ, A_2 exchanges) which have dominant helicity flip amplitudes. Thus for hypercharge exchange reactions, the interpretation of line reversed reaction pair comparisons may depend heavily on detailed knowledge of the absorption differences in the particular initial and final states.

As mentioned previously (Chapter 1), conventional absorption models lead to incorrect predictions while the successes of some other models seem to come from greater freedom in parametrizing the absorption. Interestingly, the introduction of phase space and angular momentum barrier corrections[37] may eliminate one of the above mentioned objections to simple absorption models.[10] One notes that the hypercharge exchange reactions are always accompanied by a change in masses from initial to final state (e.g., $\pi p \to K\Lambda$ or $\overline{K}p \to \pi\Lambda$). Although such mass shifts appear negligible when compared to incident energies of several GeV, Trilling[37] has suggested that unequal mass effects can nevertheless be quite large. To compensate for phase space and angular momentum barrier differences, Trilling suggests that cross sections should be scaled by a factor $(p_i / p_f)^{2\ell+1}$ before making any SU(3) or exchange degeneracy comparisons. The momenta p_i, p_f are defined in the center of mass and $\ell = p_i a$ with $a = 0.88$ fm.[†] With this correction applied the resulting $\pi^- p \to K^0(\Lambda, \Sigma^0)$ and

[†] An interaction radius of 0.88 fm corresponds to the first zero of $J_0(a\sqrt{-t})$ occuring at $-t \sim 0.3$ GeV^2.

$\bar{K}^o p \rightarrow \pi^+(\Lambda, \Sigma^o)$ integrated cross sections are approximately equal, although the uncorrected data differ by factors of ~ 3.5 at 3 GeV/c and ~ 1.7 at 10 GeV/c.

From the analysis of the Σ^o/Λ^o cross section ratio at $t=t_{MIN}$ (see Section 4D and Table 10) it is observed that the helicity nonflip coupling constant, F_+, varies substantially with energy (that is, the Σ^o/Λ ratio is not constant). Although there are some problems of relative normalization between different experiments, a compilation of hypercharge exchange data by Irving, Martin and Barger[47] also suggests that F_+ is energy dependent. However, recent high statistics counter experiments yield conflicting results.[36c, 36e] Interestingly, the energy dependences of the Λ^o, Σ^o data are in agreement at intermediate values of momentum transfer,[47] $-t \sim 0.3$ GeV^2, as shown in Fig. 32. A similar comparison of the energy dependences of $K^o_L p \rightarrow K^o_S p$, Kp charge exchange and $\pi^- p \rightarrow \pi^o n$ data has also observed discrepancies near $t \sim 0$.[19] Absorption or direct channel effects may provide the simplest explanation of these data.[19]

Although the forward Σ^o, Λ cross sections have a substantial energy dependence in the momentum interval 3 to 10 GeV/c, the Λ polarization data is observed to be essentially independent of the $\bar{K}^o$ momentum.† This result, and the fact that the observed polarizations are large ($\sim 80\%$ in $\bar{K}^o p \rightarrow \pi^+ \Lambda$ for $0.4 \leq -t \leq 1.1$ GeV^2) provides substantial constraints on t channel exchange models incorporating low lying daughter trajectories. Unfortunately, the condition on the polarization, P, and spin rotation parameters, A, R that

$$P^2 + A^2 + R^2 = 1$$

implies that R and A are necessarily small where P is near 1.[41] Thus the R

† Actual fits to $\langle \alpha P_\Lambda \rangle \sim S^n$ yield $n = 0.15 \pm 0.11$ for $2.5 \leq P_{BEAM} \leq 10.0$ GeV/c.

and A parameters for $\bar{K}^0 p \rightarrow \pi^+(\Lambda, \Sigma^0)$ may provide only a weak discrimination between various helicity amplitude structures in the momentum transfer interval $0.3 \lesssim -t \lesssim 1.0$ GeV^2.

G. Summary and Conclusions

We have presented experimental results on the reactions $\bar{K}^0 p \rightarrow \pi^+ \Lambda$ and $\bar{K}^0 p \rightarrow \pi^+ \Sigma^0$ from 1 to 12 GeV/c with emphasis placed on the comparison of the Λ and Σ channels and on momentum dependences in the data. The principle features of the data are:

(a) The integrated cross sections exhibit power law, $\sigma \quad P^n_{BEAM}$, behavior with $n = -2.62 \pm 0.10$ for $1.8 \leq P_{BEAM} \leq 5.0$ GeV/c and $n = -2.21 \pm 0.19$ for $P_{BEAM} > 5$ GeV/c in the $\pi^+ \Lambda$ channel and with $n = 1.78 \pm 0.09$ for $P_{BEAM} \geq 1.8$ GeV/c in the $\pi^+ \Sigma^0$ channel.

(b) The ratio $\sigma(\pi^+ \Sigma^0) / \sigma(\pi^+ \Lambda)$ in the interval $0.05 \leq -t \leq 0.4$ GeV^2 is nearly momentum independent.

(c) The differential cross sections in both reactions exhibit shrinkage of the forward peak with slope values tending toward the slopes observed in the line reversed reactions as momentum increases.

(d) The Σ^0/Λ ratio at $t = 0$ is found to increase with energy. This cannot be explained by simple K*-K** exchange models, but may suggest that absorption or direct channel effects are important.

(e) Effective trajectories for both reactions were consistent with a straight line passing through both K*(890) and K**(1420), except possibly near $t = 0$ in $\pi^+ \Sigma^0$ channel.

(f) Hyperon polarization in the $\pi^+\Lambda$ final state is large, positive, and essentially momentum independent. The polarization averaged over $0.2 \leq -t \leq 1.0\ \mathrm{GeV}^2$ varies as $s^{0.15 \pm 0.11}$ for $P_{BEAM} \geq 2.5$ GeV/c. Σ^0 polarization is found to be large and negative for $0.2 \leq -t \leq 0.4\ \mathrm{GeV}^2$.

REFERENCES

1. R.C. Arnold, Phys. Rev. Letters 14, 657 (1965).
2. R. Dolen, D. Horn, and C. Schmid, Phys. Rev. 166, 1768 (1968).
3. K. Igi and S. Matsuda, Phys. Rev. Letters 18, 625 (1967); A. Logunov, L.D. Soloviev and A.N. Tavkhelidze, Phys. Letters 24B, 181 (1967).
4. H. Harari, Phys. Rev. Letters 22, 562 (1969).
5. J.L. Rosner, Phys. Rev. Letters 22, 689 (1969).
6. F.J. Gilman, Phys. Letters 29B, 673 (1969).
7. D. Cline, J. Matos, and D.D. Reeder, Phys. Rev. Letters 23, 1318 (1969).
8. R.D. Matthews, Nucl. Phys. B11, 339 (1969).
9. K.-W. Lai and J. Louie, Nucl. Phys. B19, 205 (1970).
10. F. Henyey, G.L. Kane, J. Pumplin, and M.H. Ross, Phys. Rev. 182, 1579 (1969); R.C. Arnold and M.L. Blackman, Phys. Rev. 176, 2082 (1968); M.L. Blackman and G.R. Goldstein, Phys. Rev. 179, 1480 (1969); C. Michael, Nucl. Phys. B13, 644 (1969).
11. H. Harari, Annals of Physics 63, 432 (1971); H. Harari, "Phenomneological Duality," Stanford Linear Accelerator Center Report No. SLAC-PUB-914; H. Harari, Phys. Rev. Letters 26, 1400 (1971).
12. G.A. Ringland, R.G. Roberts, D.P. Roy and J. Tran Thanh Van, Nucl. Phys. B44, 395 (1972).
13. J.S. Loos and J.A.J. Matthews, Phys. Rev. D6, 2463 (1972).
14. D. Barkai, and K.J.M. Moriarity, Nucl. Phys. B50, 354 (1972).
15. B.J. Hartley and G.L. Kane, "Toward a General Description of Two-Body Hadron Reactions," Michigan preprint (1973).

16. R.D. Field and J.D. Jackson, Phys. Rev. D4, 693 (1971); R.D. Field, Phys. Rev. D5, 86 (1972).

17. G.W. Brandenburg, A.D. Brody, W.B. Johnson, D.W.G.S. Leith, J.S. Loos, G.J. Luste, J.A.J. Matthews, K. Moriyasu, B.C. Shen, W.M. Smart, F.C. Winkelmann, and R.J. Yamartino, Nucl. Phys. B45, 397 (1972).

18. G.W. Brandenburg, W.B. Johnson, D.W.G.S. Leith, J.S. Loos, G.J. Luste, J.A.J. Matthews, K. Moriyasu, W.M. Smart, F.C. Winkelmann, and R.J. Yamartino, Phys. Rev. Letters 28, 14, 932.

19. G.W. Brandenburg, W.B. Johnson, D.W.G.S. Leith, J.S. Loos, G.J. Luste, J.A.J. Matthews, K. Moriyasu, W.M. Smart, F.C. Winkelmann, and R.J. Yamartino, "$K_L^o p \rightarrow K_S^o p$ Scattering from 1 to 10 GeV/c," Stanford Linear Accelerator Center Report No. SLAC-PUB-1339 (1973). See also A.D. Brody, W.B. Johnson, B.Kehoe, D.W.G.S. Leith, J.S. Loos, G.J. Luste, K. Moriyasu, B.C. Shen, W.M. Smart, F.C. Winkelmann, and R.J. Yamartino, Phys. Rev. Letters 26, 1050 (1971).

21. W.B. Johnson, D.W.G.S. Leith, J.S. Loos, G.J. Luste, K. Moriyasu, W.M. Smart, F.C. Winkelmann, and R.J. Yamartino, Phys. Rev. Letters 26, 1053 (1971).

21. G.W. Brandenburg, W.B. Johnson, D.W.G.S. Leith, J.S. Loos, G.J. Luste, J.A.J. Matthews, K. Moriyasu, W.M. Smart, F.C. Winkelmann, and R.J. Yamartino, Phys. Rev. Letters 30, 145 (1973).

22. G.W. Brandenburg, W.B. Johnson, D.W.G.S. Leith, J.S. Loos, G.J. Luste, J.A.J. Matthews, K. Moriyasu, W.M. Smart, F.C. Winkelmann, and R.J. Yamartino, Phys. Rev. D8, 1978 (1973).

23. R.S. Larsen and D. Horelick, "A Precision Toroidal Charge Monitor for SLAC," Stanford Linear Accelerator Center Report No. SLAC-PUB-398 (1968).

24. G.W. Brandenburg, A.D. Brody, W.B. Johnson, D.W.G.S. Leith, J.S. Loos, G.J. Luste, J.A.J. Matthews, K. Moriyasu, B.C. Shen, W.M. Smart, F.C. Winkelmann, and R.J. Yamartino, Phys. Rev. D7, 708 (1973).

25. F.T. Solmitz, A.D. Johnson and T.B. Day, "Three View Geometry Program," Alvarez Group Programming Note P-117, Lawrence Radiation Lab (LRL) - Berkeley (1966); O.I. Dahl, T.B. Day, F.T. Solmitz and N.C. Gould, SQUAW, Alvarez Group Programming Note P-126, LRL-Berkeley (1968) (unpublished).

26. A. Levy and G. Wolf, Stanford Linear Accelerator Center Report No. SLAC-TN-68-16 (1968) (unpublished).

27. G. Wolf, Stanford Linear Accelerator Center Report No. SLAC-TN-68-3 (1968) (unpublished).

28. Particle Data Group, "Review of Particle Properties," LBL-100, April 1972.

29. A. Böhm, P. Darriulat, C. Grosso, V. Kaftanov, K. Kleinknecht, H.L. Lynch, C. Rubbia, H. Ticho, and K. Tittel, Nucl. Phys. B9, 605 (1969).

30. $K^- n \rightarrow \pi^-(\Lambda, \Sigma^0)$

    (a) R. Armenteros et al., Nucl. Phys. B18, 425 (1970);

    (b) S.A.B.R.E. Collaboration, Nucl. Phys. B33, 61 (1971);

    (c) D.J. Crennell et al., Phys. Rev. Letters 23, 1347 (1969);

    (d) W.L. Yen et al., Phys. Rev. Letters 22, 963 (1969); W.L. Yen et al., Phys. Rev. 188, 2011 (1969).

    (e) B.J. Burdick et al., Nucl. Phys. B41, 45 (1972).

31. $K^- p \rightarrow \pi^0 \Lambda$

(a) R. Armenteros et al., Nucl. Phys. B8, 233 (1968);

(b) S.A.B.R.E. Collaboration, Nucl. Phys. B18, 403 (1970);

(c) G.C. Mason and C.G. Wohl, Nucl. Phys. B58, 1 (1973);

(d) B.G.L.O.R. Collaboration, Phys. Rev. 152, 1148 (1966);

B.G.L.O.R. Collaboration, Nuovo Cimento 53A, 522 (1968);

(e) L. Moscoso et al., Nucl. Phys. B36, 322 (1972);

(f) R. Barloutaud, (Oxford Conference, 1972).

32. $K^- p \rightarrow \pi^- \Sigma^+$

(a) A. Berthon et al., Nucl. Phys. B24, 417 (1970);

(b) G.W. London et al., Phys. Rev. 143, 1034 (1966);

(c) S.A.B.R.E. Collaboration, see reference 19b above;

(d) L. Moscoso et al., see reference 19e above;

(e) J.S. Loos et al., Phys. Rev. 173, 1330 (1968);

(f) D. Birnbaum et al., Phys. Letters 31B, 484 (1970);

(g) R. Barloutaud, see reference 19f above.

33. E. Flaminio et al., "Compilation of Cross Sections, K^- Induced Reactions," CERN/HERA 70-6 (1970).

34. E. Bracci et al., "Compilation of Cross Sections, π^- and π^+ Induced Reactions," CERN/HERA 72-1 (1972).

35. D.R.O. Morrison, Phys. Letters 22, 528 (1966).

36. $\pi^- p \rightarrow K^0(\Lambda, \Sigma^0)$

(a) O.I. Dahl et al., Phys. Rev. 163, 1430 (1967);

(b) M. Abramovitch et al., Nucl. Phys. B27, 477 (1971);

(c) C.E.W. Ward et al., Phys. Rev. Letters 31, 1149 (1973);

(d) D.J. Crennell et al., Phys. Rev. D6, 1220 (1972);

(e) K.J. Foley et al., Phys. Rev. D8, 27 (1973).

37. G.H. Trilling, Nucl. Phys. B40, 1 (1972).

38. G.W. Brandenburg, W.B. Johnson, D.W.G.S. Leith, J.S. Loos, J.A.J. Matthews, F.C. Winkelmann, and R.J. Yamartino, Phys. Letters 44B, 305 (1973).

39. V.D. Barger and D.B. Cline, Phenomenological Theories of High Energy Scattering, (W.A. Benjamin, Inc., New York 1969).

40. C. Michael and R. Odorico, Phys. Letters 34B, 422 (1971).

41. A.C. Irving, A.D. Martin, and C. Michael, Nucl. Phys. B32, 1 (1971).

42. A.D. Martin, C. Michael, and R.J.N. Phillips, Nucl. Phys. B43, 13 (1972).

43. E. Segre, Nuclei and Particles (W.A. Benjamin, Inc., New York, 1964) p. 673.

44. F.T. Solmitz, Ann. Rev. of Nucl. Sci. 14, 375 (1964).

45. R. Gatto, Phys. Rev. 109 , 610 (1958).

46. B. Sadoulet, Nucl. Phys. B53, 135 (1973).

47. A.C. Irving, A.D. Martin and V. Barger, Nuovo Cimento 16A, 573 (1973).